Nagoya University

Graduate School of Engineering

On-Chip Magnetically Actuated Microrobot for Biomedical Applications

A dissertation submitted for the degree of Doctor of Philosophy

Department of Mechanical Science and Engineering

Masaya HAGIWARA

On-Chip Magnetically Actuated Microrobot for Biomedical Applications

Masaya Hagiwara

Abstract

This thesis presents high performance magnetically driven microtool (MMT) actuated by permanent magnets, which have significantly higher magnetic fields than electromagnetic coils, in a microfluidic chip for cell manipulations. High power (mN order), high precision (μm order) and high speed (up to 15 mm/sec) actuation was achieved by reducing friction on the MMT. Three different approaches to reduce friction were discussed, the driving unit development, the actuation field modification, and the MMT shape.

First, the magnetic analysis was conducted to show the current MMT problem and proved that the static friction makes an MMT control difficult. The new driving methodologies, which reduce the vertical component of the magnetic force on the MMT effectively, were introduced and supported by a finite elemental method analysis as well as the experimental results. The positioning accuracy improved 3-10 times and than in the conventional drive method. It was also extended to multi-degree of freedom movement by assembling four permanent magnets.

Next, the ultrasonic vibration was applied to glass substrate to reduce effective friction on the MMT by attaching piezoelectric ceramic. Then minimum 1.1 μm positioning accuracy was achieved as well as mN order output force and 5 Hz actuation. The problem here was the accuracy deteriorates easily with increasing MMT speed.

In order to counter above problem, riblet surface was employed on the MMT in order to reduce fluid friction force. Si-Ni composite structure was fabricated by anisotropic wet etching and DRIE of Si wafer and Ni electroplating. Evaluation experiments validate the effectiveness of the riblet surface and the positioning accuracy of MMT with riblet surface was stable in high speed region as well while it was easily deteriorated in MMT without riblet.

Several applications for cell manipulation in a microfluidic chip were presented. Owing to the high power and precise accuracy, MMT can apply wide range of applications for multi-scale of biological cells (5 – 500 μm).

Contents

List of Figures

Chapter 1.

Introduction

1.1 Cell manipulations

All living organisms are composed of single or multiple cells and the cell is the smallest unit of life. It is essential to understand the functions of cells in order to investigate life and apply it to enrich human life. The importance of cell or microorganism manipulation, separation, and cultivation is growing rapidly in recent years for various fields, such as drug discovery, regenerative medicine, investigation of new energy source, countermeasure for worldwide food shortage, preservation of species, and so on. Figure 1.1 shows the applications of the biomanipulations in various fields. The market of the applications of biomanipulations exceeds billions dollar in the world. Therefore, many researches focus on the methodology to manipulate cells precisely, effectively and with high throughput. However, the sizes of the cells are micro/nanometer order and the dominant factor of the conventional Newton equation is totally different in such a small scale from macro-scale world. Figure 1.2 shows the size classification of micro/nano- world. In micro/nanometer size world, the volume force such as gravity force and inertia force does not have impact on the actuator, while the friction force, adhesion force, viscous force and any other forces, which is not major force in macro scale world, are emerging more. In order to achieve precise cell manipulation, these factors have to be considered carefully.

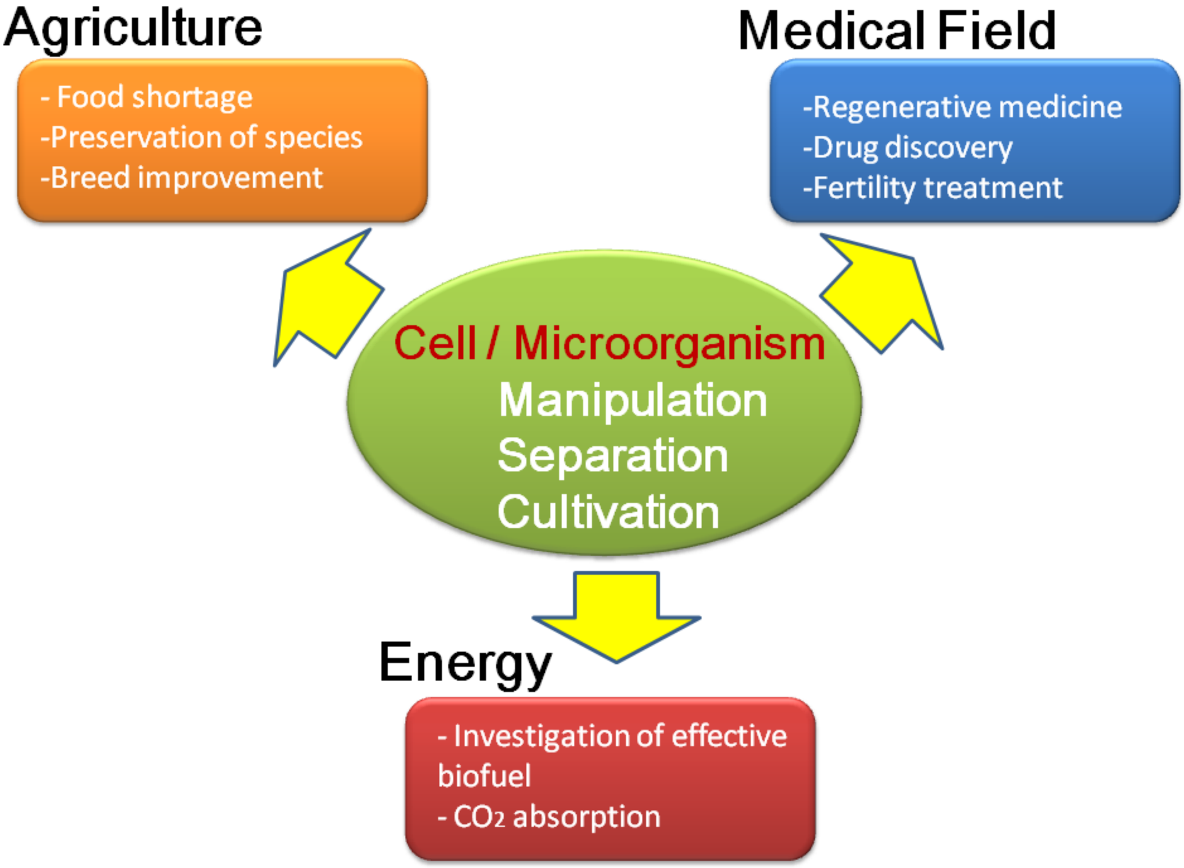

Figure 1.1 Applications of cell / microorganism manipulations in various fields

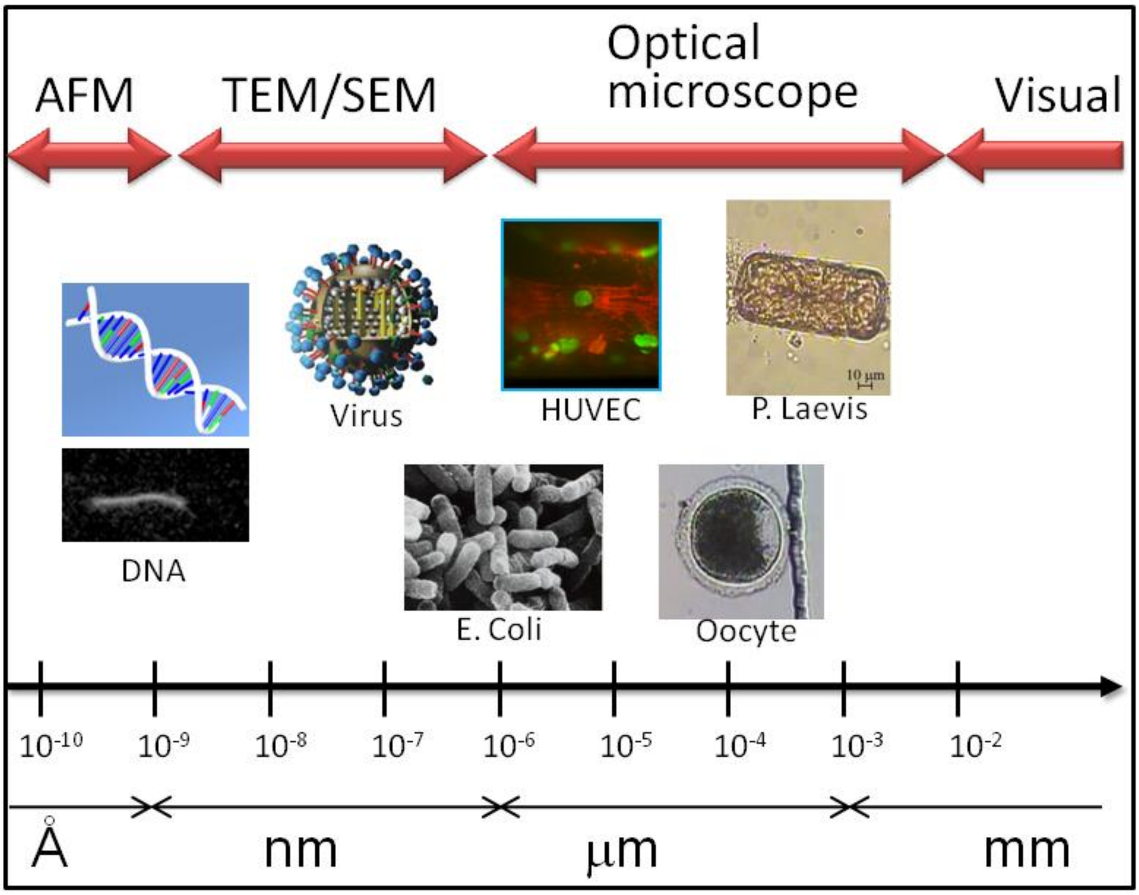

Figure 1.2 Classifications of micro / nano world

1.2 Manipulation Approaches

1.2.1 Contact manipulation

1.2.1.1 Mechanical micromanipulator

A micromechanical manipulator (Figure 1.3) is widely used for medical and life science applications because of its capability of high accuracy, high power output, and flexibility of the manipulation [1-4]. However, the manipulation is conducted in an open environment to the air due to the huge size of the manipulator and it leads to the cell contamination issues. In addition, there are many potential disturbances such as unexpected fluid flow due to the open space and it encumbers precise motion. In recent years, some research achieved cell manipulation in the size of nanometer order by inserting mechanical manipulator into E-SEM environment [5, 6]. The approach allows precise and powerful cell manipulation, such as cutting Yeast cell. But the scaling of physical effects makes even the simplest manipulation tasks challenging and the manipulation requires a high skill to the operator because the manipulator has to be controlled in 6 degrees of freedom. Therefore, the success rate, repeatability and productivity tend to depend on the operator’s skill, especially for the skilled job like enucleation of oocyte.

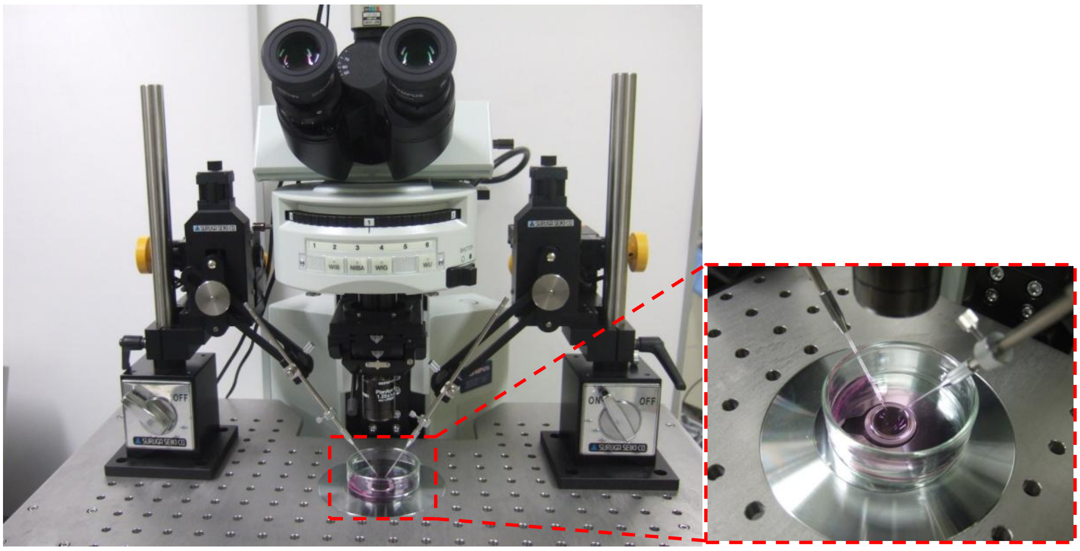

Figure 1.3 Conventional mechanical micromanipulator

1.2.2 Noncontact manipulator

In order to supply power source to an actuator without contact, field force, such as electric force, and magnetic force is required. Field force itself is normally not strong and thus, it tends to be ignored in macro-scale world. However, they can be dominant factors and enough power sources in micro-scale world since the volume force such as gravity force and inertia force tend to be lightly affected in a microscale. Representative field forces are electric force, optical force, acoustic force, and magnetic force. The actuation principles and related researches are discussed in following sections.

1.2.2.1 Dielectrophoresis

When the microparticle or cell is subjected to a non-uniform electric field, a force is exerted on a dielectric particle. This phenomenon is called Dielectrophoresis (DEP) and the DEP force amount is depend on the balance of permittivity of the medium surrounding the microparticle (ε_m), the electric field (***E***), the radius of the particle (r). By applying real part of Clausius-Mossotti factor α, the DEP force is expressed as [7-9]:

$$\vec{F}_{DEP} = 2\pi r^3 \varepsilon_m \operatorname{Re}[\alpha](\nabla \vec{E}^2) \qquad (1.1)$$

The Clausius-Mossotti factor α is expressed as

$$\alpha = \frac{\tilde{\varepsilon}_p - \tilde{\varepsilon}_m}{\tilde{\varepsilon}_p + 2\tilde{\varepsilon}_m} \qquad (1.2)$$

where $\tilde{\varepsilon}$ is the complex effective permittivity of the particle (p) and the medium (m).

Based on the balance of permittivity between the particle and medium, the direction of the force on the particle is determined and it moves toward high or low field gradient. DEP have been widely applied to cell manipulation especially for cell sorting and trapping in a microfluidic chip since 1990s [10-16]. Becker et al. separated the human breast cancer cell from blood by appropriately balancing the hydrodynamic and dielectrophoretic forces acting on the cells (Figure 1.4) [10]. Morgan et al. also succeeded in separating submicron particles by arraying the electrode on the microchannel and making use of the permittivity differences between cells [13]. Asbury et al. achieved to trap DNA molecules at the edges of the electrodes [11]. They also succeeded in moving the trapped DNA from one edge to another by mixing static and oscillating electric fields. Durr et al. comprehensively analyzed DEP force and experimentally measured DEP force, which was 50 fN to 1 pN [17]. Tsutsui et al. succeeded in quick trapping of mouse embryonic stem cell on the patterned ITO electrodes in a microfluidic chip by DEP force and external fluid flow in a microchannel [16]. They conducted to pattern pholyethylene glycol (PEG) hydrogels to prevent from cell adhesion on the microchannel and confirmed the cell survival after 1 day of trapping (Figure 1.5).

As shown above, DEP force can be suitable power source to migrate or accumulate selective cells on the particular place but it is controllable only in the limited region adjacent to the electrodes and thus, it is difficult to apply any other cell manipulation such as cutting and mechanical stimulations.

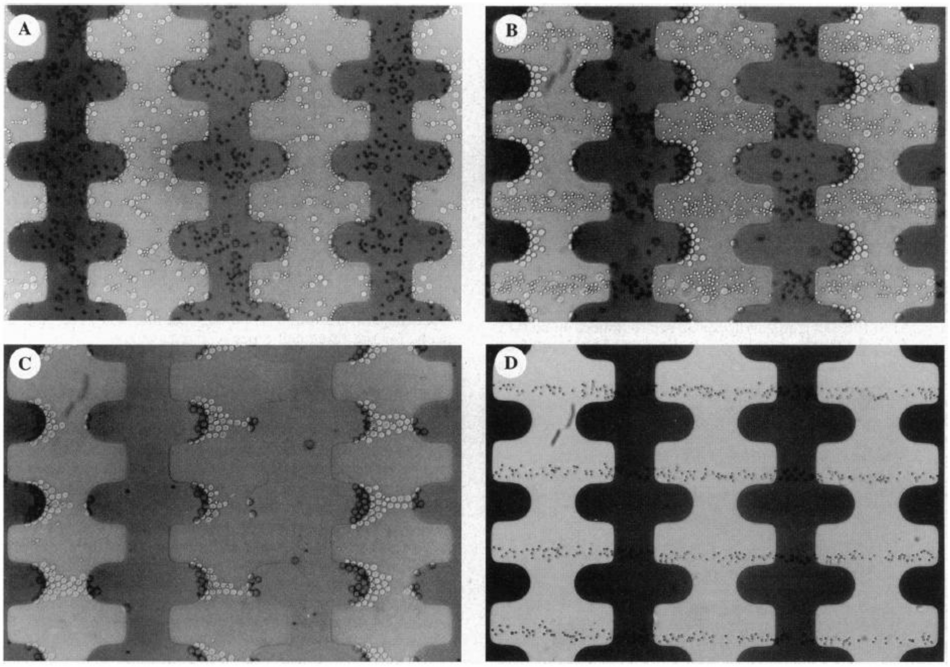

Figure 1.4 Separation of human breast cancer from blood. (A) initial collection (B) fluid flow from left to right (C) during DEP (D) migration of blood cells [10].

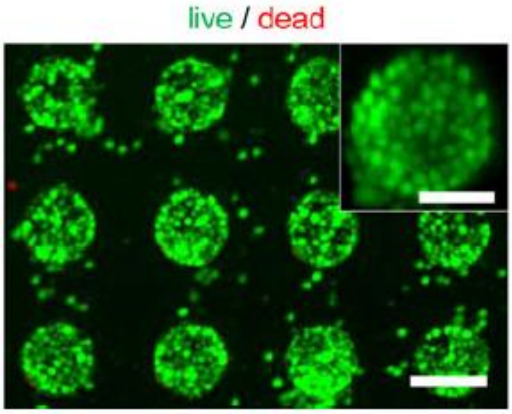

Figure 1.5 Quick trapping of mES cell at patterned ITO electrodes by DEP and fluid flow [16]

1.2.2.2 Optical tweezers

An optical trap is formed by tightly focusing a laser beam with an objective lens. A dielectric particle near the focus will experience a force due to the transfer of momentum from the scattering of incident photons. Arthur Ashkin first developed the field of laser-based optical trapping, “optical tweezers” [18, 19]. Ashkin et al. employed optical tweezers in a wide range of experiments to manipulate live bacteria or virus [19], and trapping of neutral atom [20].

Theoretical and experimental work on fundamental aspect of optical trapping is being actively pursued. Glückstad et al. developed computer generated hologra (CGH) approach, which is that there is a direct imaging operation between the spatial light modulator and the intensity profile in the tweezer plane [21]. Glückstad et al. also developed generalized phase-contrast (GPC) method to the implementation of a multi-beam optical tweezers system [22]. They achieved to generate four optical tweezers from a fixed phase mask in conjunction with a GPC system to trap and hold micron size polystyrene beads in solution. Arai et al. developed synchronized laser micromanipulation, which allowed manipulating multiple targets independently using the single laser by changing discrete laser scanning pattern

(Time-shared scanning: TSS) (Figure 1.6) [23].

The ability of apply pico-neweton order forces micrometer particles with nanometer precision is widely applied to the researches for single molecular [24-27], single cell analysis [28-31] and virus separations [32]. Wener et al. succeeded in immobilization of more than 200 yeast cells into a high-density array of optical traps and the cell array could be moved to specific locations to expose in a controlled manner the cells to reagents and to analyze the responses of individual cells (Figure 1.7). Maruyama et al. developed the device to separate ϕ 100 nm virus by employing optical tweezers and DEP and achieved to infect a specific cell with an influenza virus in order to analyze the mechanism of the infection.

As shown above, the optical tweezers are now one of the most successful tools to manipulate single cell and it has ability to manipulate cells of nm to μm size with nm order resolution. However, the weakness of the optical tweezers is its small amount of output force and thus the application is limited to trapping or migration of small size of cells.

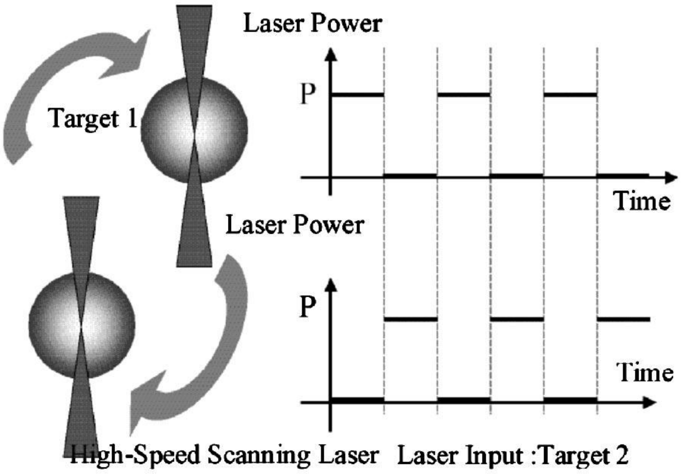

Figure 1.6 Principle of Time-shared Scanning: TSS [23]

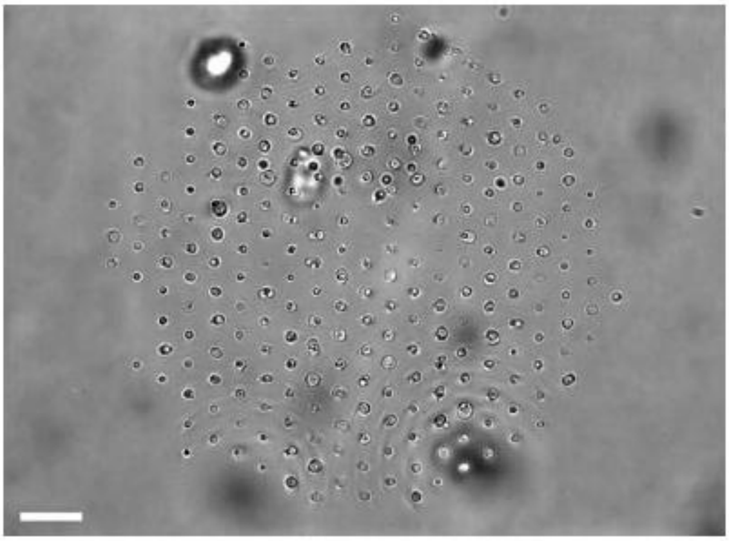

Figure 1.7 More than 200 trapped yeast cells by optical tweezers; scale bar: 30 μm.

1.2.2.3 Acoustic force

Suspended particles in an acoustic field are affected by acoustic forces. Acoustic waves generate pressure gradients and acoustic forces in a liquid, which can be used to manipulate particles or cell in a microfluidic chip. Recently surface acoustic waves (SAW), generated by interdigital transducers (IDT) on a piezoelectric substrate, has been employed to focus [33], separate [34, 35], align [35-38], direct microparticles [35, 39, 40] and to manipulate the fluid droplets [41-47] (Figure 1.8). Yeo et al. derived the acoustic radiation force as follows;

$$F_{AR,L} = 2\pi\rho(\frac{2\pi f}{c_f})R^6|\xi|^2 \frac{1+\frac{2}{9}\left(1-\frac{\rho}{\rho_p}\right)^2}{\left(2+\frac{\rho}{\rho_p}\right)^2} \qquad (1.3)$$

where $|\xi|$ is the fluid particle velocity, ρ is the fluid density, ρ_p is the particle density, f is the frequency of the incident sound field and c_f is the sound speed in the fluid medium. The novelty of the IDT electrodes is it can determine the wave length by designing the pith of the electrode.

Shi et al. developed a microfluidic particle focusing device using standing surface acoustic wave (SSAW) [33]. They also demonstrated to manipulate multiple particles in 2-D by designing pairs of IDT in different direction (Figure 1.9) [34]. Cecchi et al. developed PDMS and $LiNBO_3$ devices for droplet control in microfluidic chip by SAW [46]. They succeeded in transporting the droplet though a microchannels.

The novelty of the SAW is that it can manipulate multiple particles at one time, and it can conduct multi-DOF manipulation by combining multiple IDT electrodes. On the other hand, it is difficult to manipulate single particle or cell from the mixture and achieve precise positioning control due to reflection and interference of the acoustic wave. It will be stronger device if it is combined with any other noncontact actuation such as optical tweezers and magnetic force.

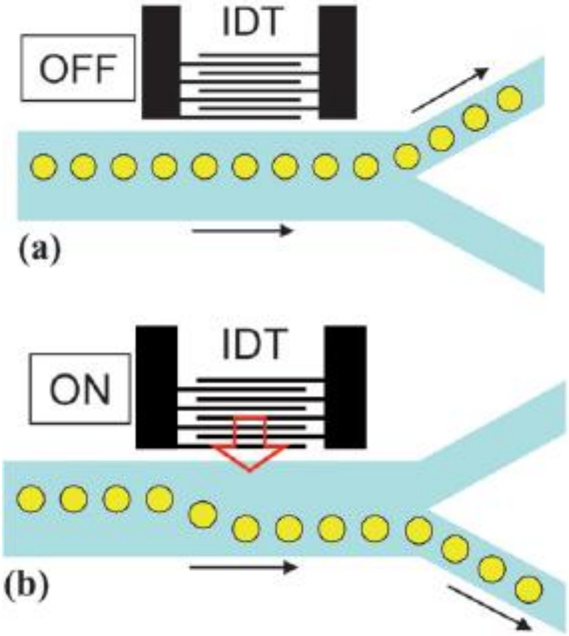

Figure 1.8 Particle sorting by SAW [35]

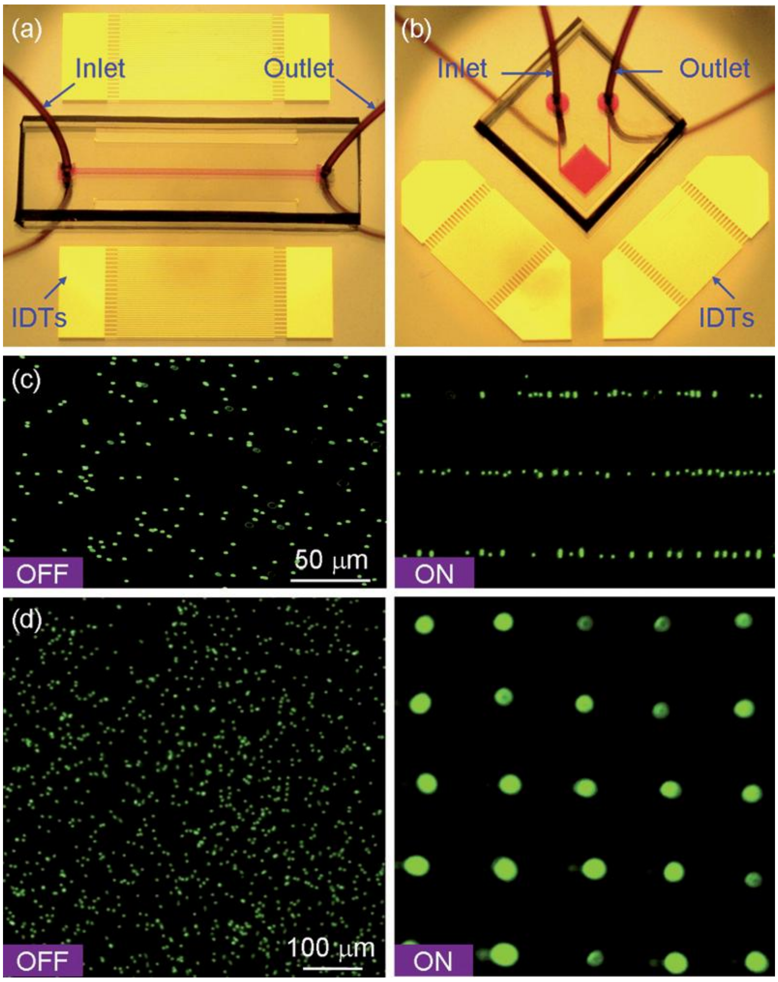

Figure 1.9 Cell alignment by SSAW [34]

1.2.2.4 Magnetic force

One of the most promising actuation methods at the microscale is magnetic force which is generated by permanent magnet or electromagnetic coils. Cugat et al. comprehensively analyzed effect of magnetic force on the magnetic body in size and distance from the magnet and proved that magnetic force is strong power source for microactuator [48]. The magnetic force can be calculated as follows;

$$F_{mag} = \mu_0 v (M \cdot \nabla) H \qquad (1.4)$$

where μ_0 is v is volume of magnetic body, M is magnetization of the material, H is magnetic field intensity, ∇ is gradient operator, which is expressed as

$$\nabla = \left[\frac{\partial}{\partial x} \quad \frac{\partial}{\partial y} \quad \frac{\partial}{\partial z} \right]^T \qquad (1.5)$$

Barbic et al. actuated magnetic object in a microfluidic chip by magnetic fields generated by three electromagnetic coils set on the XYZ linear stages and achieve to 3-DOF actuation, x-y-θ[49]. Rotation of magnetic material inside a microchannel can be achieved by a rotating external magnet with a conventional stirrer plate [50-52] (Figure 1.10). Gauthier et al. analyzed the magnetic fields on the permanent magnet and controlled magnetic object position and its posture. It is achieved strong output force from permanent magnet and precise positioning accuracy. However, it is only available on the large magnet, thus, it cannot operate multiple microrobot at a time and the application is limited since the posture is changing by changing positions [53] (Figure1.11).

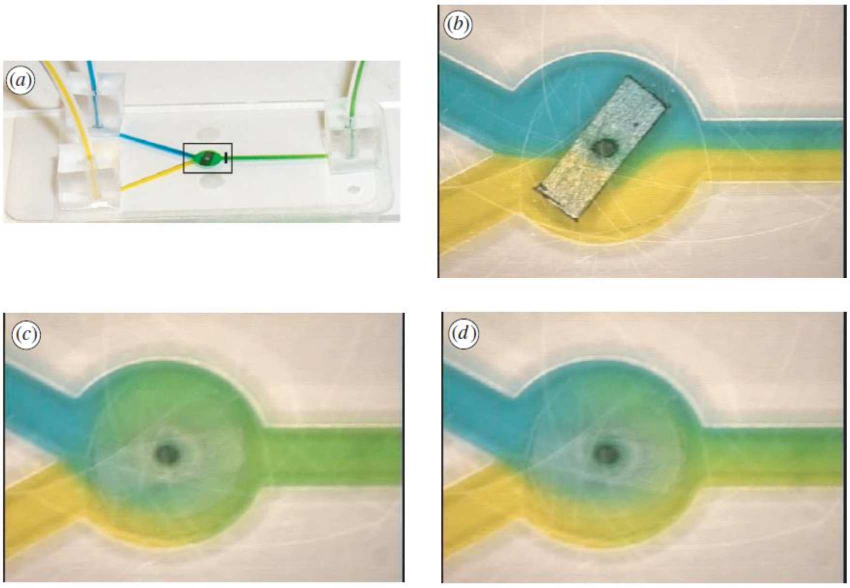

Figure 1.10 Mixture device operated by permanent magnet outside the microfluidic chip [50]

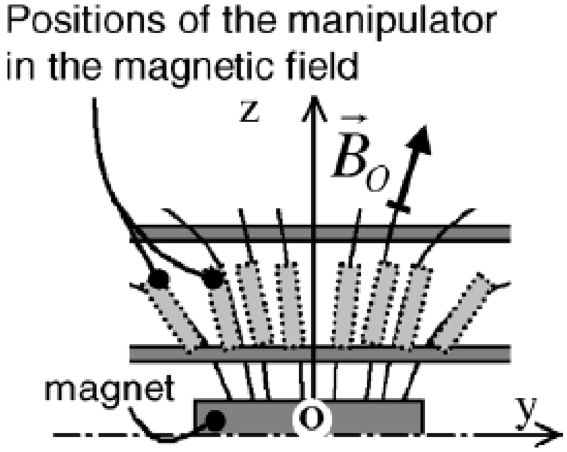

Figure 1.11 Manipulator control of permanent magnet actuation [53]

Helmholtz coil, which is composed of pairs of electromagnetic coils with concentric circle, is widely used for the cell manipulation in recent years owing to uniform magnetic fields between coils. It can generate uniform magnetic fields in multiple axes by combining two or three Helmholtz coils and it enables multi-DOF actuation of on-chip robot

Nelson et al. are continuously researching magnetic actuators operated by pairs of Helmholtz [54-57]. They fabricated spiral shape microrobot using MEMS technology and the microrobot swim in liquid environment and it can achieve 6-DOF precise actuation (Figure 1.12). The final goal of this research is actuating microrobot in vivo environment by MRI and thus recently they comprehensibly modeled in vivo situation [58]. Sitti et al. also applied pairs of Helmholtz coils for microrobot actuation [59, 60]. They actively employed stick-slip effects on the sliding magnetic object by switching the magnetic fields of vertical direction and horizontal direction (Figure 1.13). They recently achieved to assemble microobjects by manipulating hexahedron posture [59]. Kumar et al. also employed Helmholtz coils to obtain precise control of microtranspoter [61, 62]. They integrated the magnetic actuation with vision feedback control, and they achieved to deliver the microgel to neuron.

As discussed above, Helmholtz coils is promising tool to achieve precise accuracy of actuation in multi-DOF but it requires special design of microscope. In addition, the size of the cells and the application of the Helmholtz coil are limited due to micronewton order force from electromagnetic coils.

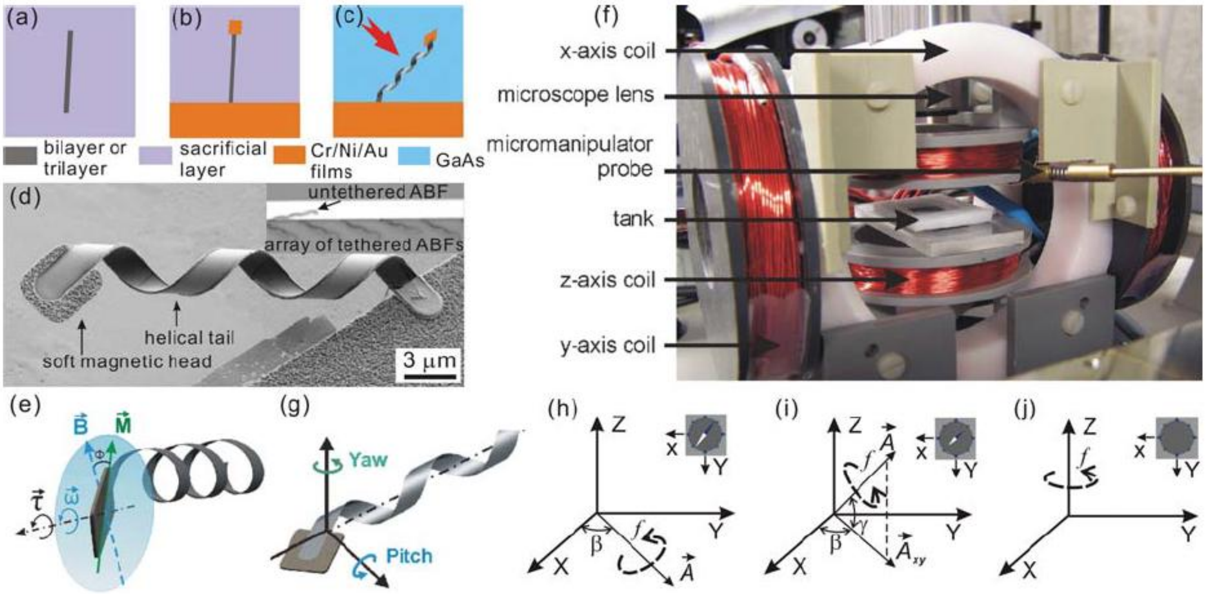

Figure 1.12 Magnetically driven microrobot using Helmholtz coils [56]

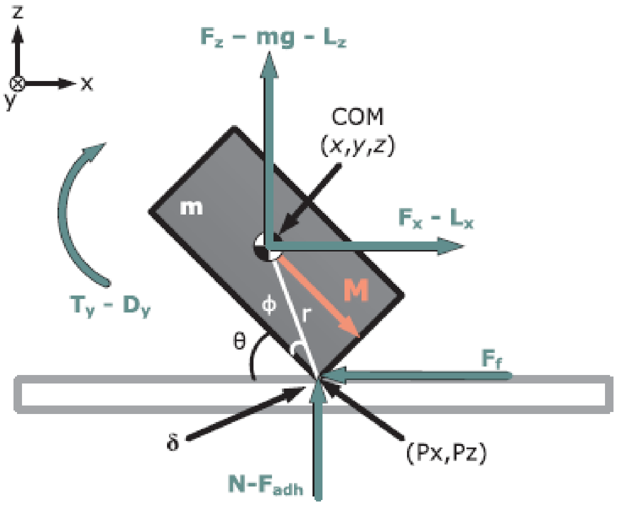

Figure 1.13 Stick-slip motion model actuated by Helmholtz coils [60]

1.2.3 Microfluidics

Another approach to manipulate biological cells is conducted in a microfluidic chip. The area of micro total analysis systems (μTAS), also called “lab on a chip”, miniaturized or microfluidic analysis systems, is a rapidly developing field. A Lab-on-a-Chip is a device to integrate laboratory functions into single microfluidic chip of millimeter or centimeter square in size by employing microelectromechanical systems (MEMS) technology, surface modification, flow control, and micro channel design [63]. Figure 1.14 shows immunoassay device made by polydimethylsiloxane (PDMS). The device contains various functions to imitate laboratory environment in a small size of the chip. The microfluidics allows achieving high throughput screening, separation, detection and reaction in a small confined space taking advantages of the ability to use very small quantities of samples and reagents, and to carry out separations and detections with high resolution and sensitivity; low cost; short times for analysis; and small footprints for the analytical devices [64]. The applications of microfluidic

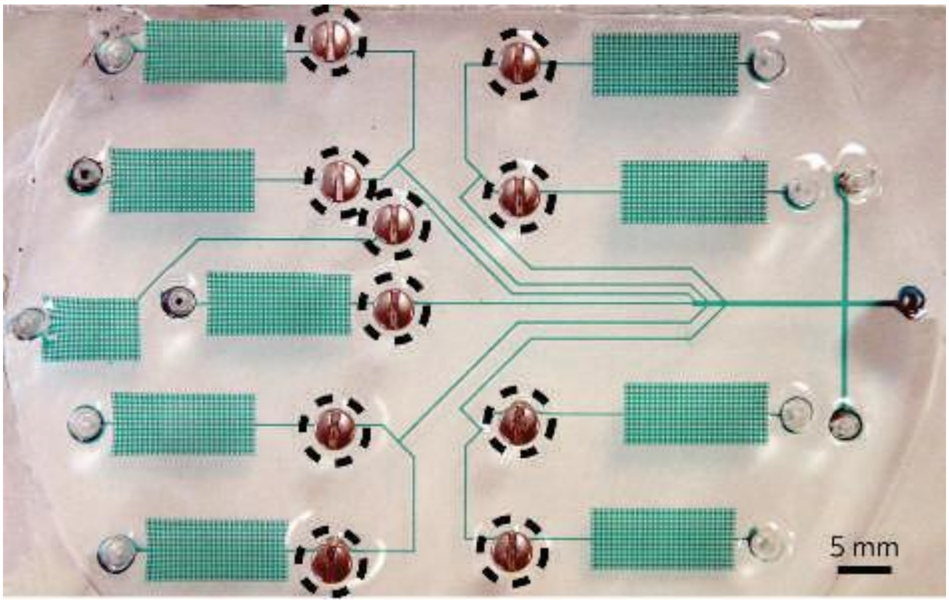

Figure 1.14 Microfluidic diagnostic device [65]

chip are mainly separation [66-72], mixing [73-77], droplet generation [78-84], cultivation [85, 86] and so on.

Numerous works were focused on cell separation using fluid control in a microfluidic chip and succeeded high throughput separation in order to analyze single cell or detect specific cell from cell turbid solution. Inertia force is dominant force for most of separation device. It allows label-free, size dependent separation by designing microchannels. Han et al. developed separation microfluidic chip for circulating tumor cell from blood by inertial microfluidics [72] (Figure 1.15). They focused attention on the fact that the tumor cell is relatively large in blood cells and designing microfluidic chip for tumor cell to get centered and for the other blood cell to flow along the PDMS wall.

Monodisperse emulsions or droplets are widely used not only as functional materials for drugs, foods, and cosmetics, but also as the starting materials for producing monodisperse particles and capsules for various chemical, biomedical, and industrial applications. Seki et al. succeeded in generating 15 daughter droplets from a large mother droplet by fluid control [80] (Figure 1.16). They designed channel network based on resistive circuit model to control the distribution ratio of the flow rate, which dominates the division ratios of the mother droplets.

As shown above, the microfluidics offers so many advantages, but the operation of the cell manipulation is generally passive way in Lab-on-a-Chip fields, and therefore it is difficult to achieve precise mechanical cell manipulations.

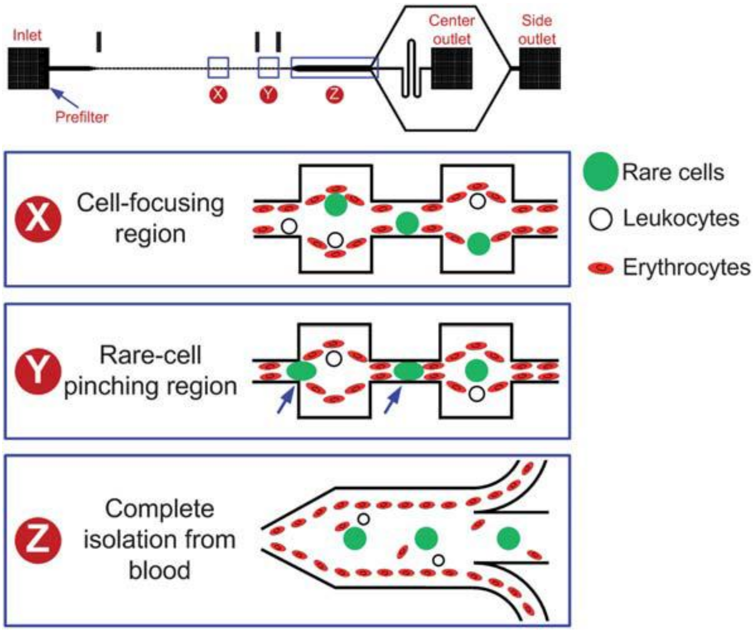

Figure 1.15 High throughput separation for circulating tumor cell from blood [72]

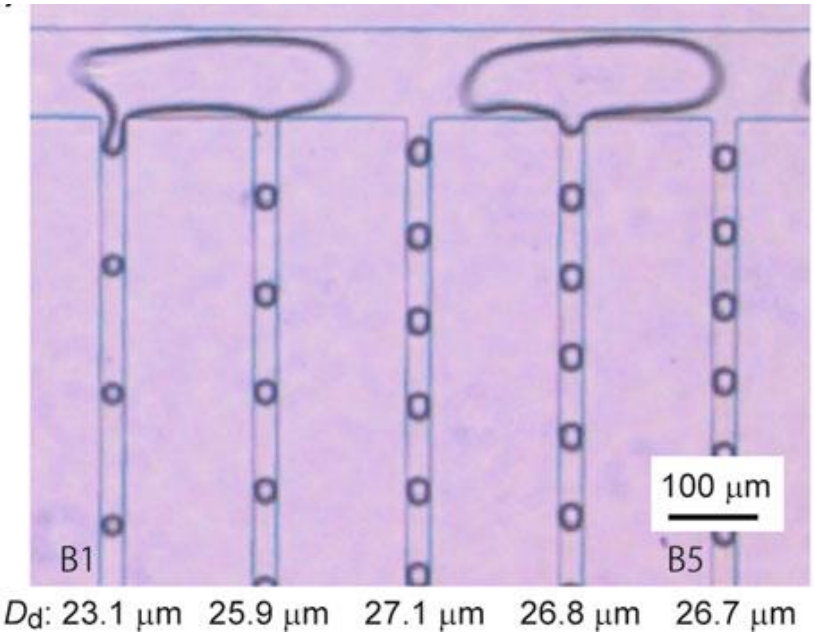

Figure 1.16 Multiple droplet generation by fluid control [80]

1.2.4 On-chip robot

Cell manipulations in the confined space of a microfluidic chip have great advantages in the field of biotechnology because of the low contamination capability, repeatability, and high throughput ability [87-89]. Especially cell manipulations by microrobot in a microfluidic chip have great advantages for the treatment of biological cell instead of human handling due to their non-skill dependent, high throughput and high repeatability [90]. Figure 1.17 shows the concept of on-chip robot. Taking advantages of both of manipulator and Lab-on-a-Chip devices, in other words, mechanical approach and environmental approach, on-chip robot have potential to achieve powerful and accurate actuation, for broad range of cell manipulations with high throughput. In additions, the cost of on-chip robot is generally low owing to the small size of the manipulator and microfluidic chip and thus it is disposable after the operation is conducted to prevent cell contaminations. Furthermore, closed environment of microfluidic chip also help to prevent cell contamination as well as provide stable environment for the robot actuations.

For the actuation of the microrobot in a microfluidic chip, the noncontact drive principle is required. Many different approaches are investigated for the actuation of microrobot and they have always pros and cons. A brief review of noncontact actuations as well as related work will be discussed in next sections.

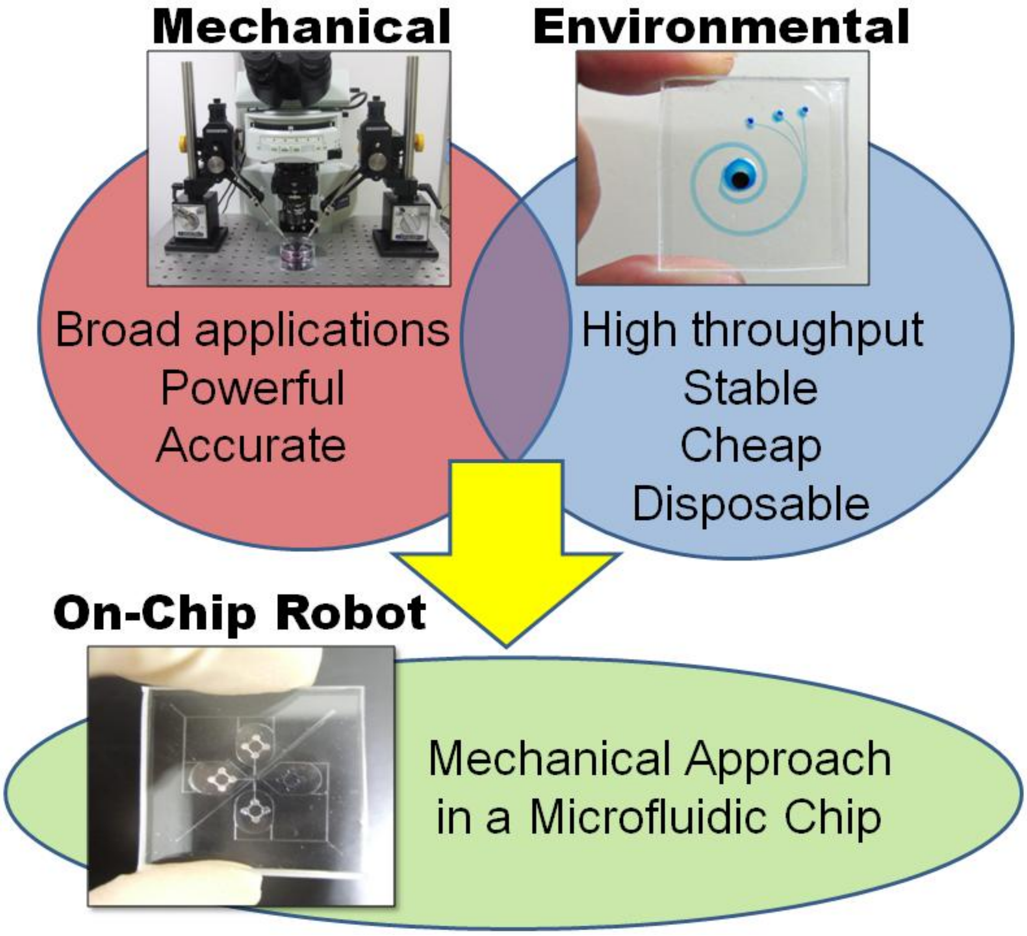

Figure 1.17 Concept of on-chip robot

1.3 Magnetically Driven Microtool (MMT)

A permanent magnet has a more than 10-100 times stronger magnetic field to drive an MMT than an electromagnetic coil of the same size. Arai et al. continuously developed magnetically driven microtool (MMT) to manipulate biological cell in a microfluidic chip. The novelty of the MMT is that powerful actuation of permanent magnet drive can be achieved and the material of the MMT has choice depending on the applications. Figure 1.18 shows the classification of the MMT based on the composed material. Polymer MMT is fabricated by mixture of the polydimethylsiloxane (PDMS) and magnetite particles. This type of MMT can manipulate biological cells without damage since PDMS is soft and biocompatible material. On the other hand, Metal based MMT, which is fabricated by electroplating after photolithography, is hard material and it can receive strong magnetic force since it is ferromagnet. Therefore, it can apply force required job such as cutting cells. Also, it can be used as movable electrode since it is conducting body as well and the electric currency can be applied. Hybrid of metal and polymer structure has both advantages of materials.

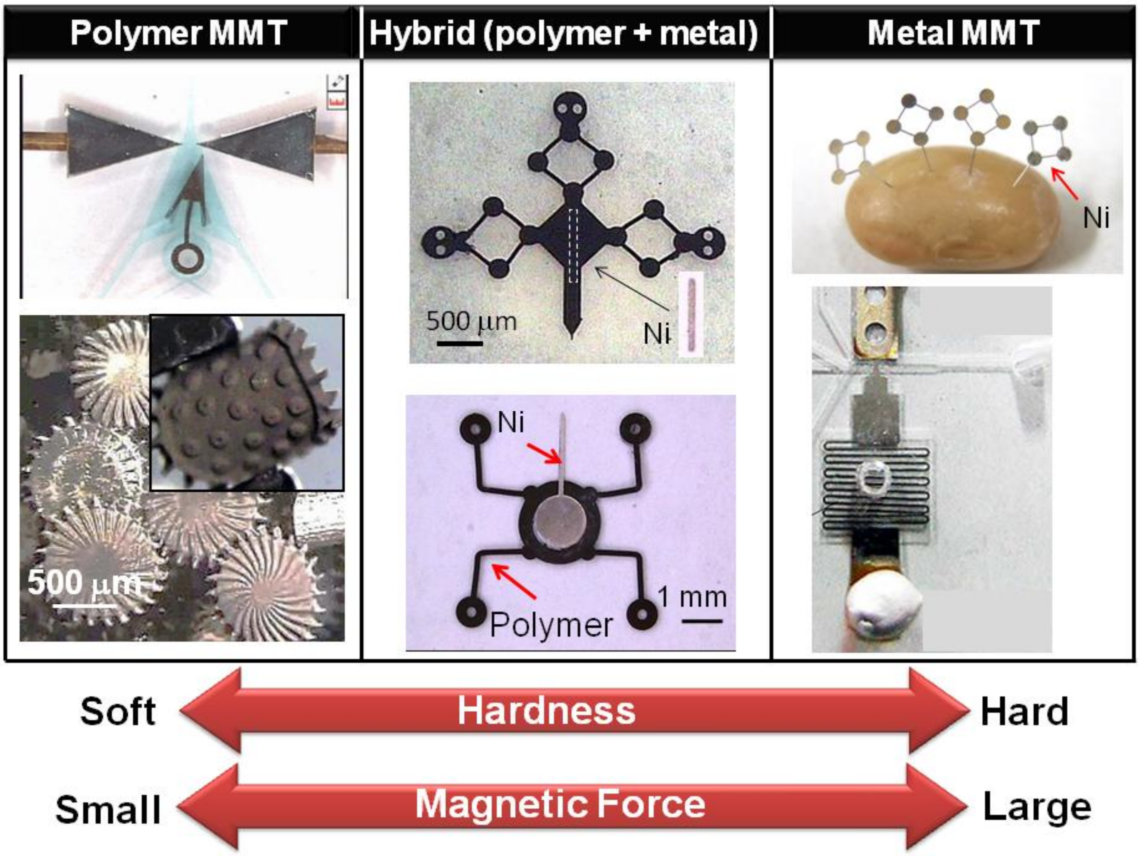

Figure 1.18 Classification of MMT based on material

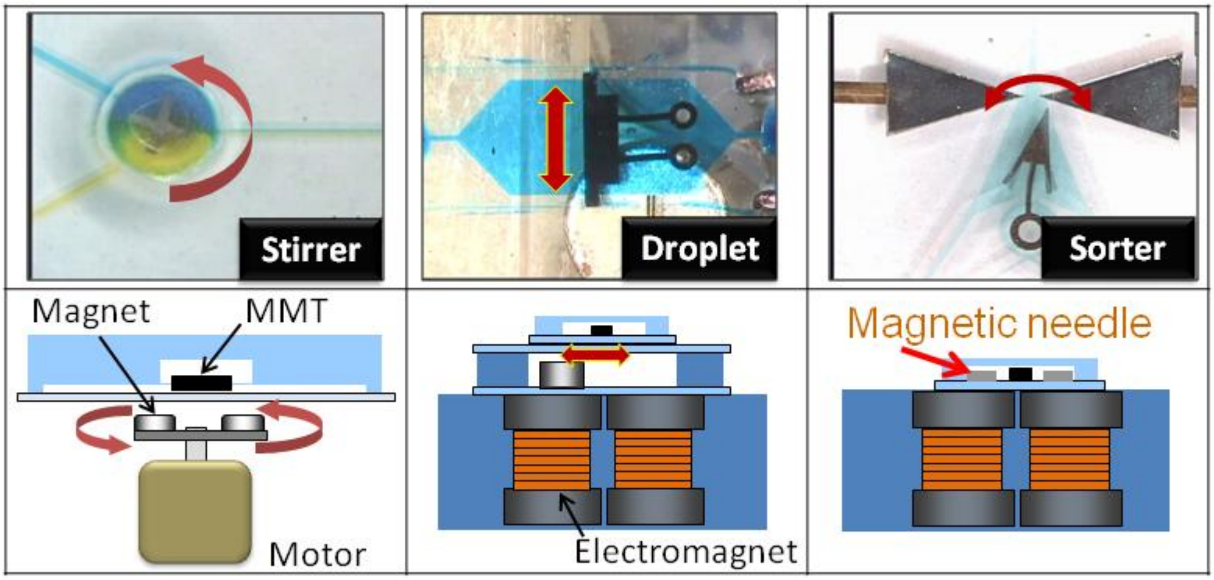

Figure 1.19 Classification of conventional MMT drive [91, 92]

Therefore, MMT can be used for various applications to relatively large cell / particle, whose size is ϕ 100 or more, manipulations such as particle sorter [93, 94], loader [92], filtering [95], and droplet generation [91, 96]. On the other hand, permanent magnet drive had weakness in positioning accuracy and thus the controllability was quite low. Therefore, the conventional MMT application was restricted to only on-off movement. Figure 1.19 shows classification of these MMT drives. The MMT was not required for precision movement in these actuations. Inomata et al. actuated hybrid type of MMT by permanent magnet set on the *XY* linear stages and achieved enucleation process by MMTs [97] (Figure 1. 20). In order to compensate the low controllability of the MMT, they anchored polymer part to control the posture of the MMT by assembling the hole prepared on the MMT leg to the PDMS pillar in the microfluidic chip, but still it took time to operate enucleation process by the developed MMT.

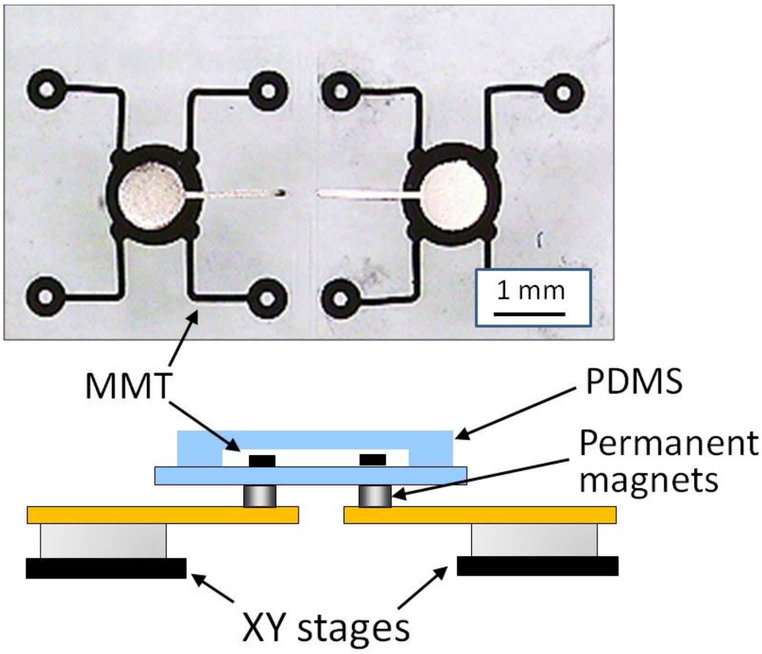

Figure 1.20 MMT drive by permanent magnet set on the *XY* linear stage [97]

1.4 Thesis Overview

1.4.1 Research aim and target

Although there are many novel noncontact actuators discussed above, the output force of the most of the noncontact actuators is less than μN orders. Therefore, the applications of the actuators are limited to jobs not required strong force such as delivery of small size of cell. On the contrary, the output force of permanent magnet is extremely high without any electrical input. It is not smart way to waste this inherent strong material. But the low positioning accuracy also limits its application to simple task.

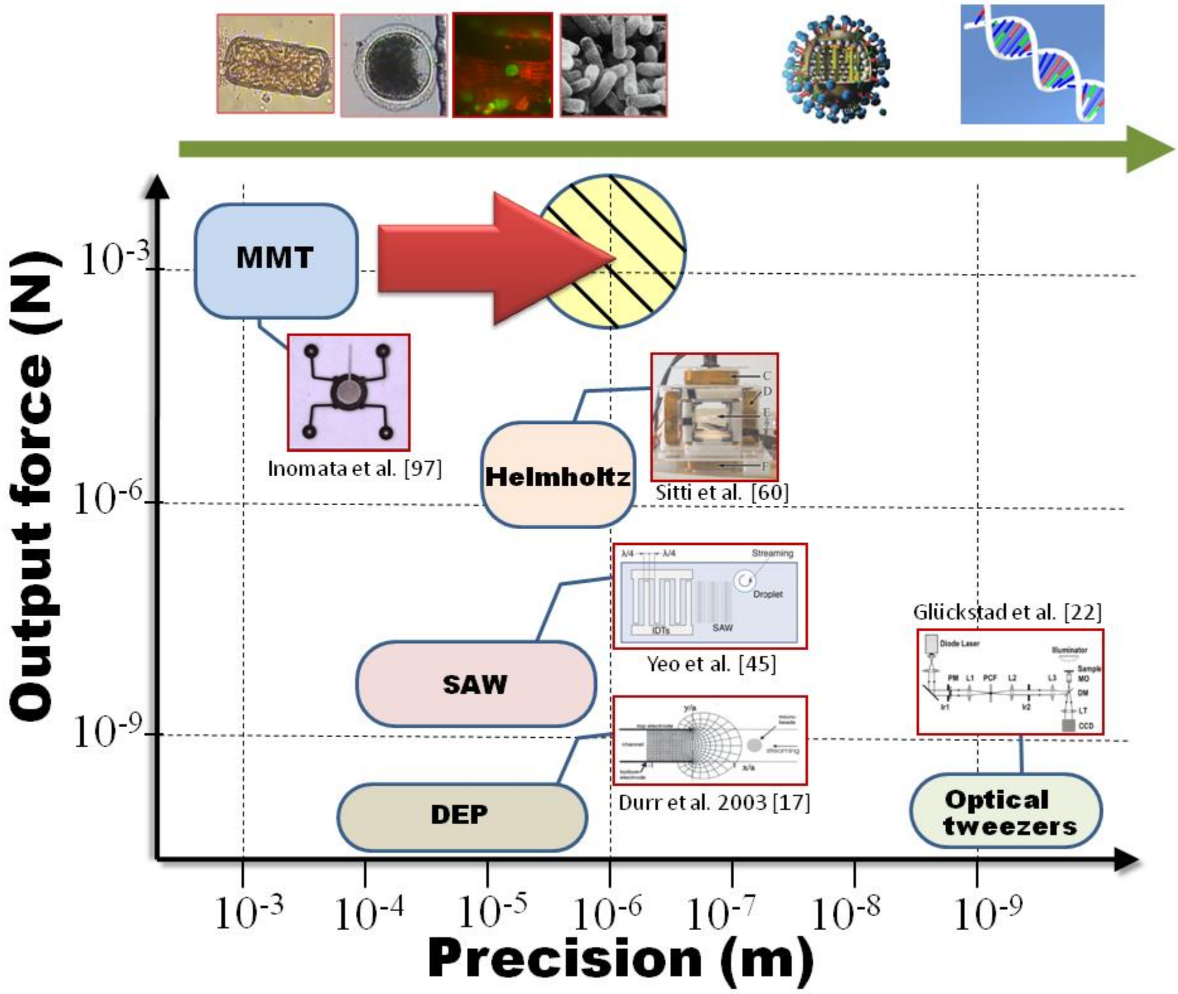

Figure 1.21Classification of noncontact actuator and the research aim.

Therefore, the research aim of this dissertation is to improve the positioning accuracy to micrometer order with keeping strong output force of the MMT (Figure 1.21). Then, the MMT can be applied to wide range of cell manipulations such as enucleation of oocyte, which requires high power to conduct. And the multi-scale of biological cells can be targeted form the size of micrometer order to submillimeter order.

Figure 1.22 shows the conceptual view of the dissertation goal. The MMTs are placed in a microfluidic chip and actuated by permanent magnets set on linear stages. Then, the MMT manipulates the inserted cells under the microscope just like a micromechanical manipulator does, but the size of the manipulator is significantly smaller and the environment is more stable than in the case of micromechanical manipulator owing to the closed space of the microfluidic chip. In addition, the advantage of the microfluidic chip allows manipulating cells continuously by flowing cells in a designed channel to the MMT.

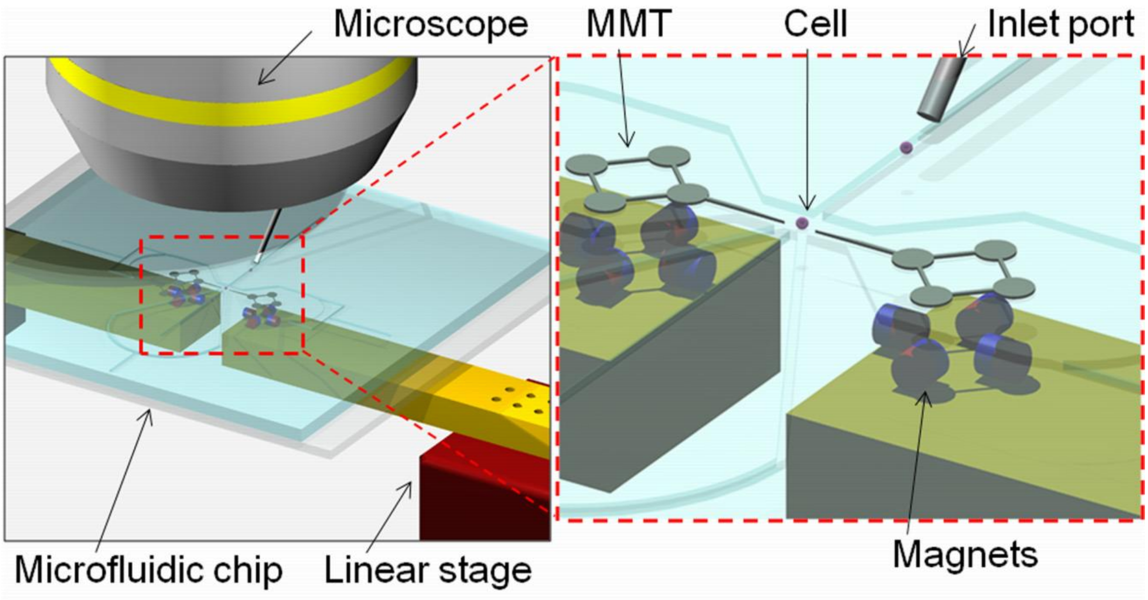

Figure 1.22 Conceptual view of thesis goal

1.4.2 Outline of dissertation

This dissertation consists of seven chapters and proposes new drive methodology for the MMT in order to achieve precise accuracy. The schematic diagram is shown in Figure 1. 23. The novel methods are proposed from three different aspects, which are, 1. drive unit (chapter 3), 2. microfluidic chip conditions (chapter 4), and 3. MMT shape (chapter 5). and combined for biomedical applications (chapter 6). The outline is described as follows (Figure 1.24).

Chapter 2: The reason of the low positioning accuracy in current MMT will be discussed. The static magnetic analysis supports the fact that friction is the key issue to improve positioning accuracy of MMT.

Chapter 3: Two of novel methods for the drive units will be discussed to reduce friction on the MMT. FEM analysis as well as experimental data validates the effectiveness of the drive. It is also extend multi degrees of freedom actuation.

Chapter 4: Friction reduction by oscillating glass substrate of microfluidic chip will be introduced. The evaluation experiments for the effects of friction reduction by vibration in terms of accuracy, output force and speed will be presented.

Chapter 5: Novel MMT shape is designed to minimize friction on the MMT. Optimization of the design parameters and its fabrication will be discussed as well as the evaluation experiments.

Chapter 6: Several cell manipulations in a microfluidic chip, such as enucleation of oocyte, and multiple sorter will be presented.

Chapter 7: Summary of the dissertation and future work will be discussed.

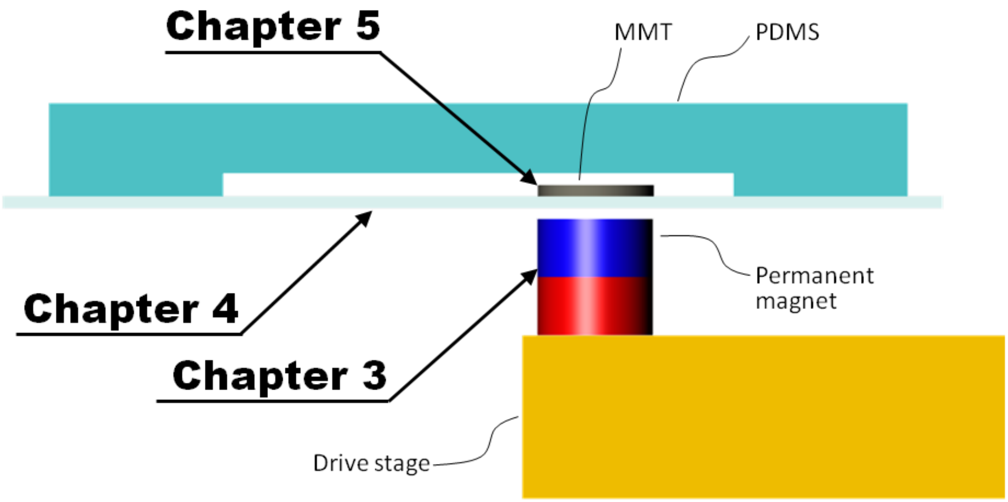

Figure 1.23 Schematic diagram of the outline

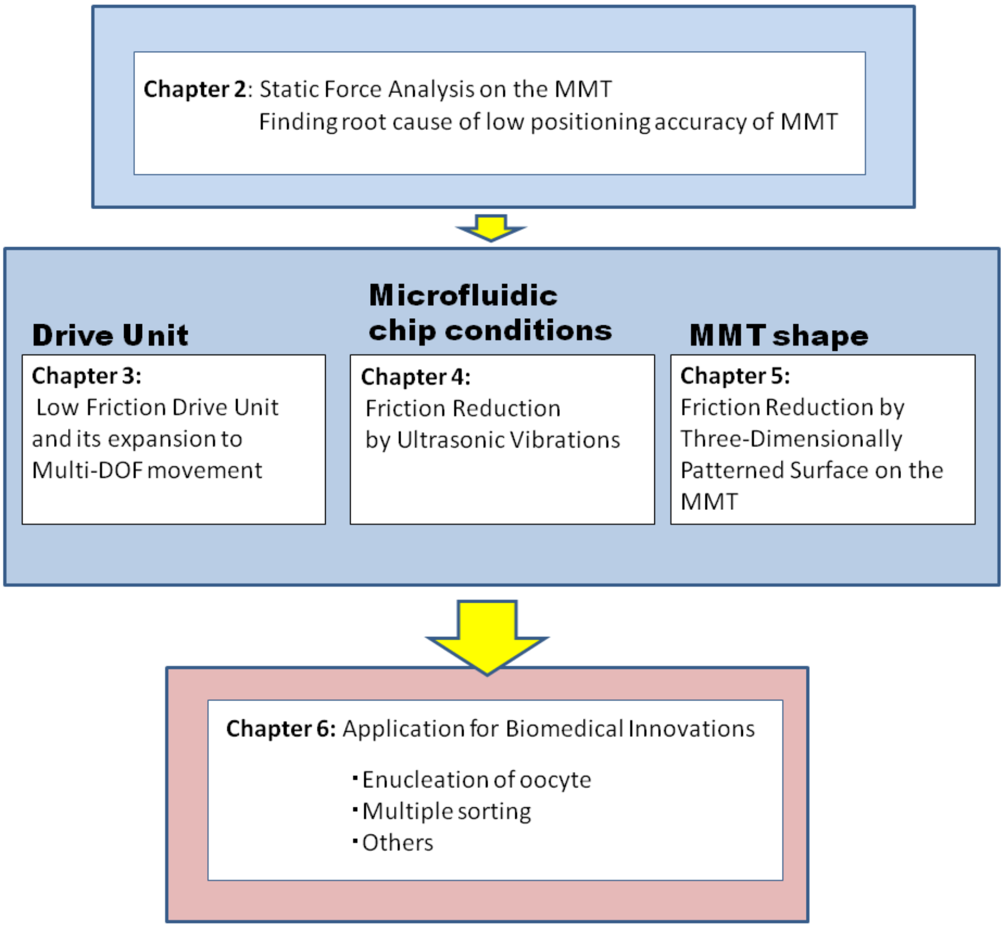

Figure 1.24 Outline of the dissertation

Chapter 2.

Static Force Analysis on the MMT

2.1 Dead Band

It is essential for an MMT to follow the drive unit precisely for the precise positioning of MMT in a microfluidic chip. However, there is an area where the MMT is not driven when the magnet passes under the MMT when the permanent magnet actuates an MMT beneath the microfluidic chip, and we call this area the “dead band”. Figure 2.1 shows a nickel-based MMT (diameter = 1.0 mm, height = 0.05 mm) driven by a neodymium ($Nd_2Fe_{14}B$) permanent magnet (diameter = 1.0 mm, height = 1.0 mm, grade: N40). The MMT was not driven until the distance between the magnet and the MMT reached 543.0 μm, and then the MMT started following the magnet. This large amount of dead band interferes with the precise positioning of the MMT on a microfluidic chip and deteriorates the effective control of the MMT as a robot on a chip because of the slow response speed to the driver unit. Therefore, analyzing the

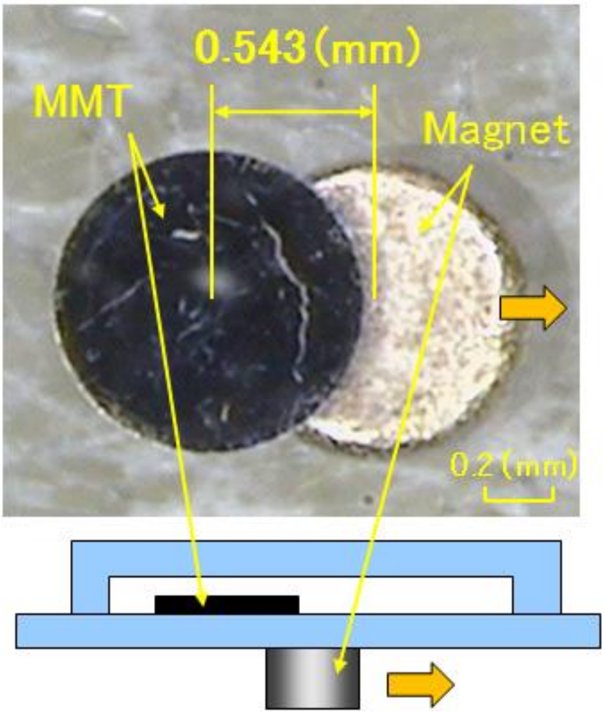

Figure 2.1 Measured dead band area when the MMT is driven by a permanent magnet (magnet: neodymium, ϕ1.0×1.0 mm; MMT: nickel, ϕ1.0×0.05 mm).

dead band is necessary for the precise control of magnetic microactuators.

2.2 Related Forces Working on an MMT

In case of static conditions, the forces employed on an MMT in a liquid atmosphere are mainly following five factors; gravity force, buoyancy force, Van der Waarls force, magnetic force, and static friction force.

- **Gravity force**

Gravity force is one of the major factors to have an impact on the Newtonian dynamics, but the effect of the gravity tends to be vanishingly small in microscale. Assuming the density of the Ni is 8.8 g/cm^3, the gravity force acting on the MMT in the case of Figure 2.1 is

$$F_g = V \times \rho_{Ni} \times g = 3.3(\mu\text{N}) \qquad (2.1)$$

where V is the MMT volume, ρ_{Ni} is the density of Ni and g is constant of gravitation.

- **Buoyancy force**

Since an MMT is acting on liquid atmosphere, the buoyancy force is employed on the MMT. Assuming the density of the water is 1.0 g/cm^3, the buoyancy force acting on the MMT in the case of Figure 2.1 is

$$F_B = V \times \rho_{water} \times g = 0.4(\mu\text{N}) \qquad (2.2)$$

where ρ_{water} is the density of water.

- **Van der Waals force**

Van der Waals force is normally ignored in macro-scale dynamics since the amount is considerably small comparing to the other forces, but the effect of Van der Waals force is getting stronger with decreasing the target object size. Therefore, it is better to confirm the amount of Van der Waals force acting on the MMT. In order to calculate the Van der Waals force, the distance between the two solid objects is the key factor of the amount of Van der Waals force and the distance is highly depend on the surface roughness of the objects. Therefore, the roughness of the MMT was measured by contact type surface measurement (Surfcorder ST200, Kosaka Laboratory Ltd.). Figure 2.2 shows the result of the surface roughness data of the MMT and the maximum average roughness of Ni plate fabricated by electroplating was 0.141 μm.

Assuming the distance between the two solid objects is same as mean surface roughness, then the Van der Waals force acting on the MMT in the case of Figure 2.1 can be calculated as follows [98]

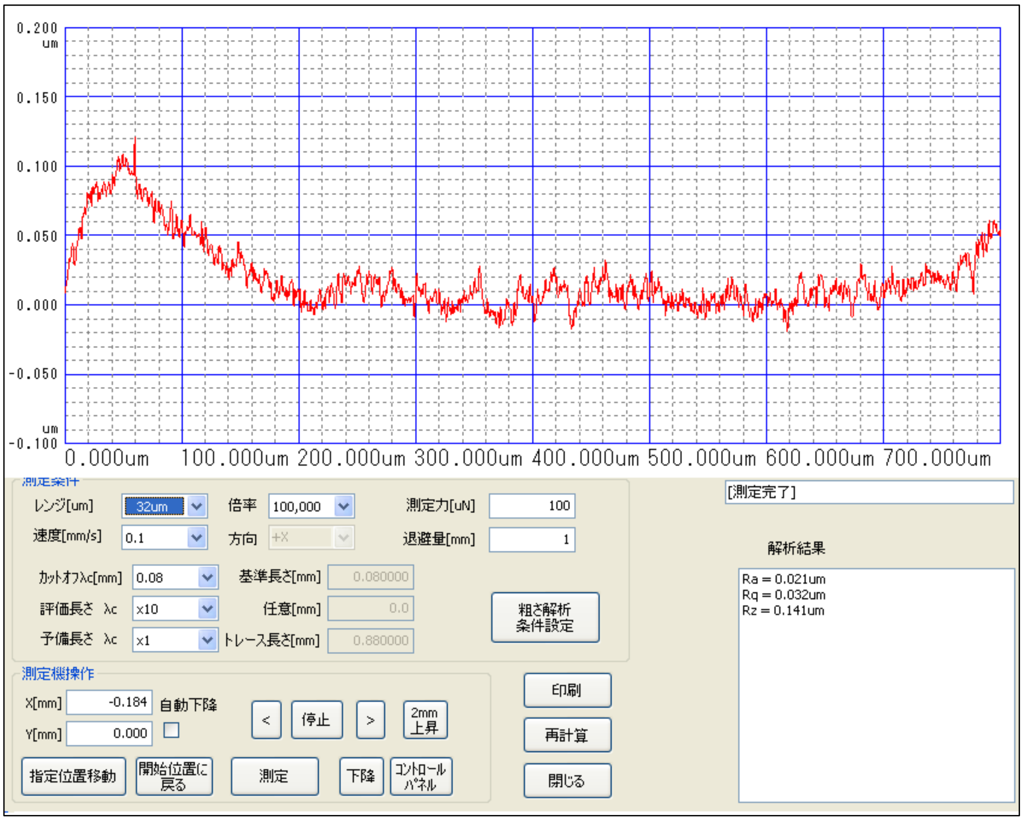

レンジ[um] 32um
倍率 100,000
測定力[uN] 100
速度[mm/s] 0.1
方向 +X
退避量[mm] 1
カットオフλc[mm] 0.08
基準長さ[mm] 0.080000
評価長さ λc x10
任意[mm] 0.0
予備長さ λc x1
トレース長さ[mm] 0.880000
X[mm] -0.184
Y[mm] 0.000
自動下降 ☐
[測定完了]

解析結果

Ra = 0.021um
Rq = 0.032um
Rz = 0.141um

Figure 2.2 Surface roughness data for the MMT fabricated by Ni electroplating.

$$F_V = \frac{A}{6\pi d^3} \times S = 0.6 \ \ (\mu\text{N}) \qquad (2.3)$$

where A is Hamaker constant (40 × 10^{-20} J), *d* is the distance, and S is the surface area acting on the Van der Waals force.

- **Magnetic force**

The magnetic field generated by a permanent magnet is quite strong. Even ϕ 1.0 mm × 1.0 mm neodymium magnet (grade: N40) has approximately 150 mT on the magnet surface and the measured magnetic force indicated it generated mN order magnetic force. The detailed calculation of the magnetic force is shown in the next section.

- **Friction force**

Friction force can be calculated by the product of friction coefficient and vertical force acting on the MMT including normal force and stiction force such as van der Waals force [99]. The friction coefficient of the metal object is normally in the range of 0.1 ~ 0.3, and thus, it can be estimated that the friction on the MMT is mN or sub-mN order. The detailed calculation of the friction is shown in the next section.

2.3 Static Magnetic Field Analysis

2.3.1 Modeling of static force on the MMT

In order to counter the cause of the dead band and predict its amount for a certain MMT and a magnet, we have developed a static force model on the MMT (Figure 2.3). The gravitational force, buoyant force, and the Van der Waals' force are ignored in this model since these are relatively small as compared to the magnetic force applied to the MMT.

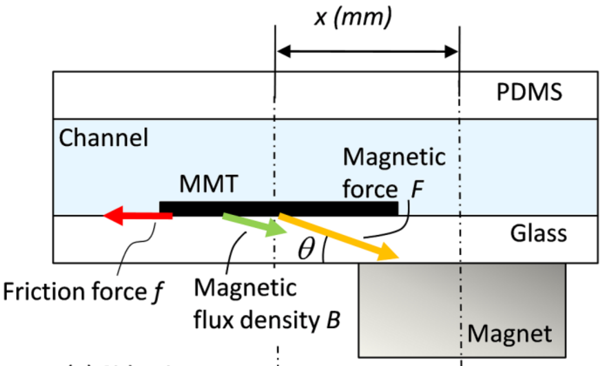

(a) Side view

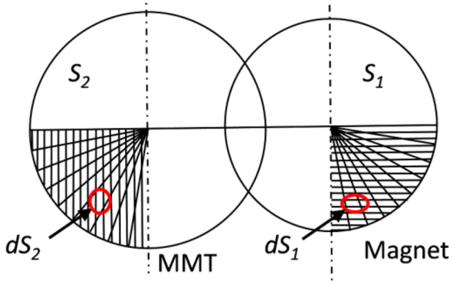

(b) Top view

Figure 2.3 Static force model driven by a permanent magnet in a microfluidic chip.
(a) Side view. (b) Top view

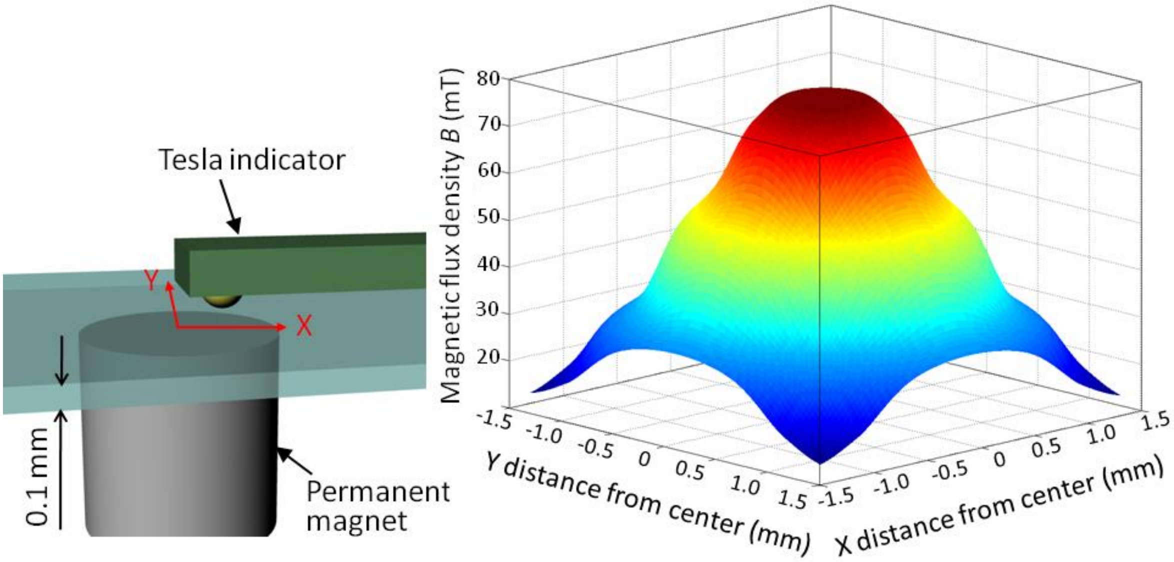

(a) Measurement conditions

(b) Magnetic flux distributions

Figure 2.4 Magnetic flux density distributions around magnet
(magnet: neodymium, ϕ 1.0× 1.0 mm, height of the grass substrate: 0.1 mm)

For the calculation of the magnetic force, the magnet and the MMT are subdivided into very small elemental areas dS_1 and dS_2, respectively. Then, the vector $\boldsymbol{B}$, which is the magnetic flux density in the small elemental area of the MMT (dS_2), can be computed by dividing the sum of the vectors of the flux from each small elemental area dS1 by the magnet area S_1:

$$\vec{B} = \iint d\vec{B} \cdot dS_1 \Big/ S_1 \qquad (2.1)$$

where $d\boldsymbol{B}$ is magnetic flux density radiated from each small elemental area of the magnet dS_1.

However, it is quite difficult to express magnetic flux density distribution around a magnet by single formula since a magnetic flux density $\boldsymbol{B}$ has complicated nonlinear distribution due to its dependence of size, shape, and the magnet material feature. Therefore, the cubic spline interpolation from experimentally measured data is used to predict the magnetic flux density distribution around the magnet. Figure 2.4 shows experimentally measured magnetic flux density distributions. The neodymium magnet is fixed and the tesla indicator (T-571, Denshijiki Industry Co. LTD.) measured at 10 points in *X* and *Y* direction respectively and cubic interpolation was applied.

The pressure **P** on the small elemental area of the MMT (***dS₂***) can be expressed as the same manner with Abbott et al [54]. That is;

$$\vec{P} = \upsilon(M \cdot \nabla)\vec{B} \qquad (2.2)$$

where v is the MMT volume and M is the magnetization.

Finally, the total magnetic force **F** on the MMT can be calculated by the sum of the elemental forces, which is calculated by the product of pressure ***P*** and elemental area dS_2;

$$\vec{F} = \iint \vec{P} \cdot dS_2 \qquad (2.3)$$

The drive force of the MMT is the horizontal component of F vector and the friction force on the MMT can be expressed as the product of the vertical component of ***F*** vector and the static friction coefficient μ. The MMT can move when the drive force is larger than the friction force;

$$\left|\vec{F}\right|\cos\theta - \left|\vec{F}\right|\sin\theta \times \mu > 0 \qquad (2.4)$$

where θ is an angle of the vector ***F*** from the horizontal line.

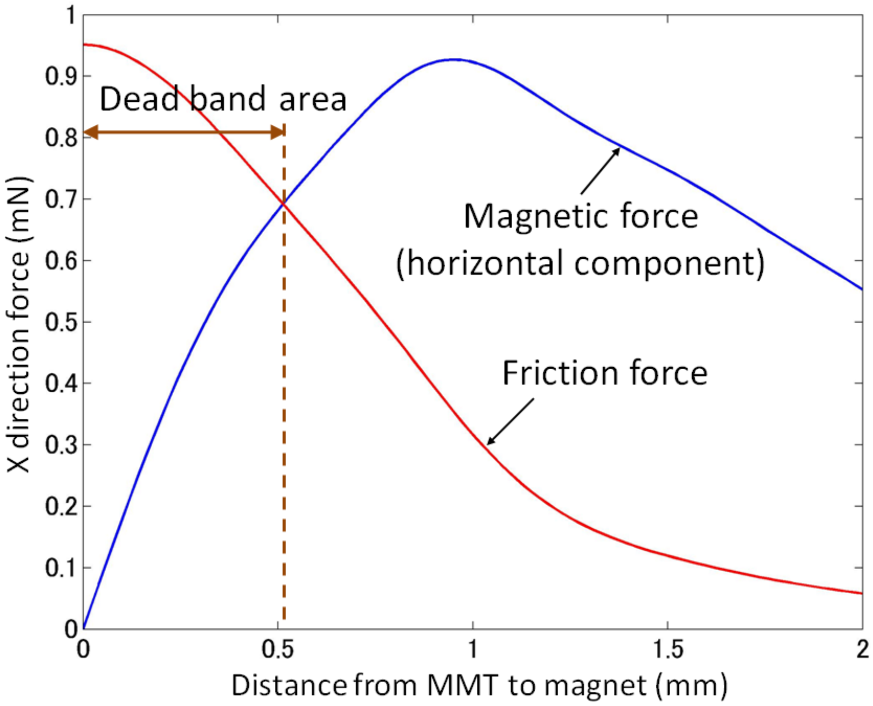

Figure2.5Simulation result of the drive force of the MMT and the friction force (magnet: neodymium, ϕ1.0×1.0 mm; MMT: nickel, ϕ1.0×0.05 mm).

2.3.2 Simulation result

Figure 2.5 shows the simulation result under the conditions that the magnet size was ϕ1.0 × 1.0 mm, and the material was Neodymium, while the MMT size is ϕ1.0 × 0.05 mm, and the material was nickel. The saturation magnetization is material constant, which is 5.12×10^5 A/m for Ni. It can be seen that the magnetic force in the horizontal direction increases along with the distance increase around the magnet, and then starts decreasing with increasing distance, while the friction force is almost constant around the magnet and starts decreasing with increasing distance. In the region, where the magnet is totally covered by the MMT, the friction force is higher than the drive force. Thus, the MMT does not move in spite of the magnet movement. When the distance reaches to 513.0 μm, the driven force exceeds the friction force and the MMT starts following to the magnet. This simulation result is corresponding to the measured dead band amount mentioned above (543.0 μm).

From this result, it can be determined that the dead band is caused by the static friction. This simulation can predict the drive force, the friction force on an MMT and the dead band amount respectively and helps designing the magnetic microactuators to avoid dead band. As it is now clear that the cause of the low positioning accuracy and the low controllability is the static friction, the next stage is how to reduce the friction on the MMT.

2.4 Conclusion Remarks

In this chapter, static force modeling was developed by dividing small elemental area of MMT and permanent magnet respectively. By integrating elemental magnetic force vector, the total magnetic force vector could be calculated. The any other forces in vertical direction are ignored in the model sine were considerably smaller than magnetic force generated by permanent magnet. By taking into account of friction force derived from vertical force on the MMT and friction coefficients, the dead band amount can be estimated. From this result, it can be determined that the dead band is caused by the static friction. This simulation can predict the drive force, the friction force on an MMT and the dead band amount, respectively, and helps designing magnetic microactuators to avoid the dead band. As it is now clear that the cause of the low positioning accuracy and the low controllability is the static friction, the next stage is how to reduce the friction on the MMT.

Next chapter presents new driving methodology for an MMT to reduce friction on the MMT.

Chapter 3.

Friction Reduction by Drive Unit

3.1 Concept and Principle of New Driving Method

3.1.1 Magnetic analysis of conventional drive method

In order to analyze the root cause of the large friction force on an MMT, FEM analysis was conducted. Figure 3.1 shows the magnetic flux density distributions by an FEM analysis of the conventional MMT driven (magnet: ϕ1.0 × 1.0 mm neodymium, MMT: ϕ1.0 × 0.05 mm Ni MMT). As shown in the Figure, the direction of the magnetic flux density around the MMT is vertically aligned and thus the large downward force is applied. This downward force makes the friction on the MMT larger. The gravity force on the MMT is 0.38×10^{-3} mN since the specific gravity of Ni is 7.88, while the downward force by the magnetic force is 1.59 mN according to equation (2.2). Therefore, approximately 2000 times larger downward force is applied on the MMT from the magnetic field than gravity force of MMT. Reducing the

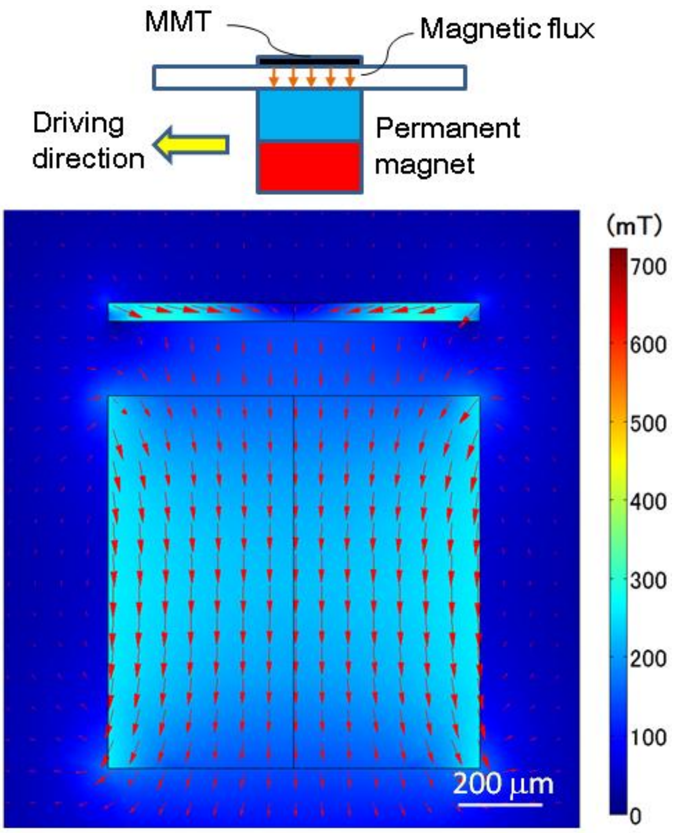

Color: Magnitude of magnetic flux density
Arrow: Direction of magnetic flux density

Figure 3.1 FEM results of magnetic flux density in conventional drive
(magnet: neodymium, ϕ1.0×1.0 mm; MMT: nickel, ϕ1.0×0.05 mm).

downward force from magnetic fields is essential to reduce the friction on the MMT and thus increasing MMT accuracy.

Two effective drive methods to reduce the downward force on an MMT are proposed as following.

3.1.2 Two-tiered magnetic drive (TMD)

In order to reduce the friction, the vertical force on an MMT has to be reduced. Figure 3.2 (a) shows the concept of two-tiered magnetic drive (TMD). The magnetic sheet, which is embedded in a microfluidic chip, counters the magnetic flux of the drive magnet by applying magnetic flux in reverse direction. Since an MMT is subject to both of upward and downward forces, it leans in a microchip and the contact area between the MMT and the grass substrate is significantly reduced. Figure 3.2 (b) shows the FEM result of the TMD for magnetic flux density (magnet: ϕ1.0 × 1.0 mm neodymium, MMT: ϕ1.0 × 0.05 mm Ni MMT). Comparing with Figure 3.1, the vertically aligned magnetic flux decreases significantly around the MMT. Much reduced downward force and smaller contact area makes the friction considerably reduced.

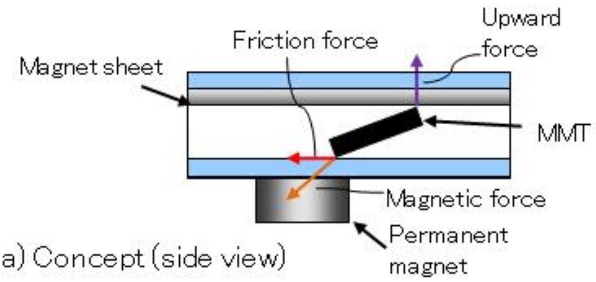

(a) Concept (side view)

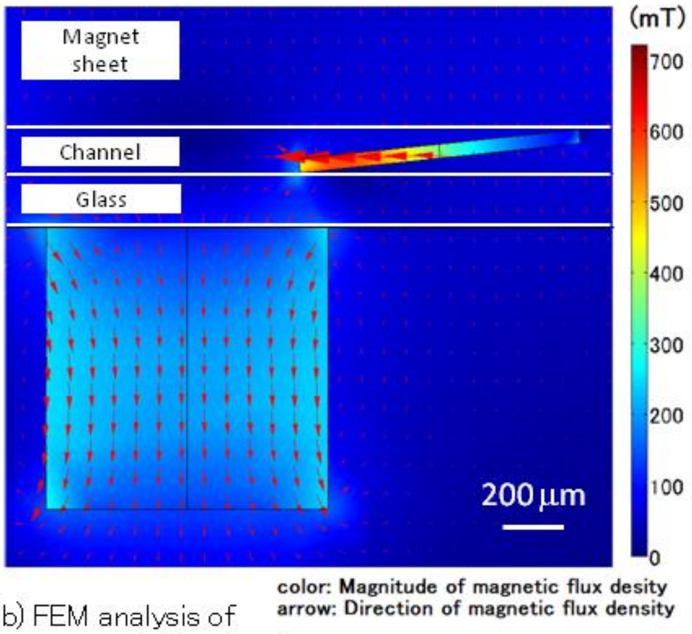

(b) FEM analysis of magnetic flux density

Figure 3.2 FEM results of magnetic flux density in TMD
(a) Concept (side view), (b) FEM analysis of magnetic flux density

(magnet: neodymium, ϕ1.0×1.0 mm; MMT: nickel, ϕ1.0×0.05 mm).

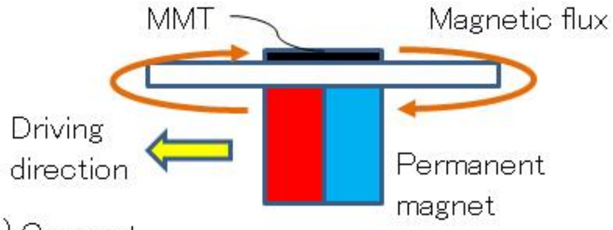

(a) Concept

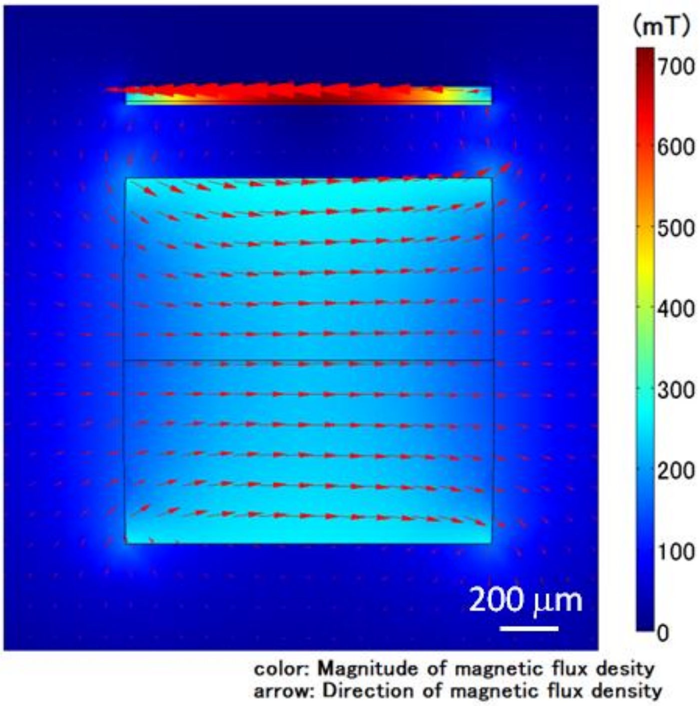

(b) FEM analysis of magnetic flux density

Figure 3.3 FEM results of magnetic flux density in HPD.
(a) Concept (b) FEM analysis of magnetic flux density
(magnet: neodymium, ϕ1.0×1.0 mm; MMT: nickel, ϕ1.0×0.05 mm).

3.1.3 Horizontal polar drive (HPD)

Another way to reduce the vertical force on the MMT is that the MMT is set such that the permanent magnet pole is parallel to the driving direction of a magnet that has the same size as the MMT. Here we describe the driving method of the MMT in such setup as the horizontal polar drive (HPD). Figure 3.3 shows the concept and the FEM result of HPD (magnet: ϕ1.0 ×

1.0 mm neodymium, MMT: ϕ1.0 × 0.05 mm Ni MMT). The magnetic flux flows in a circular pattern through the MMT, and its direction is aligned to the driving direction. As a result, there is considerably less magnetic flux in the vertical direction around the MMT as compared to that shown in Figure 3.1. In addition, the magnetic flux density inside the MMT is twice as high as that shown in Figure 3.1.This implies that magnetic power with a considerably high efficiency is applied to the MMT and the magnetic force on the MMT is much greater in the driving direction than in the vertical direction; therefore, the friction force is reduced by decreasing the vertical force on the MMT.

3.2 Experimental Evaluations of drive methods

3.2.1 MMT fabrications

The Ni based MMT fabrication process is shown in Figure 3.4. At first, the sacrificial layer (LOR 5B, Tokyo Ohka Kogyo Co., Ltd.) is coated on Si wafer. Then Cr - Au is sputtered on the wafer (thickness = 300 nm). Next, the photoresist (KMPR 3035, Nippon Kayaku Co., Ltd.) is spin-coated on the substrate. After the exposure, the KMPR pattern is developed by NMD-3 (Tokyo Ohka Kogyo Co., Ltd.). Finally the Ni was grown by the electroplating (= 50 μm). After removing the photoresist and sacrificial layer by remover PG (Nippon Kayaku Co., Ltd.), the Ni parts can be collected and cleaned by ultrasonic.

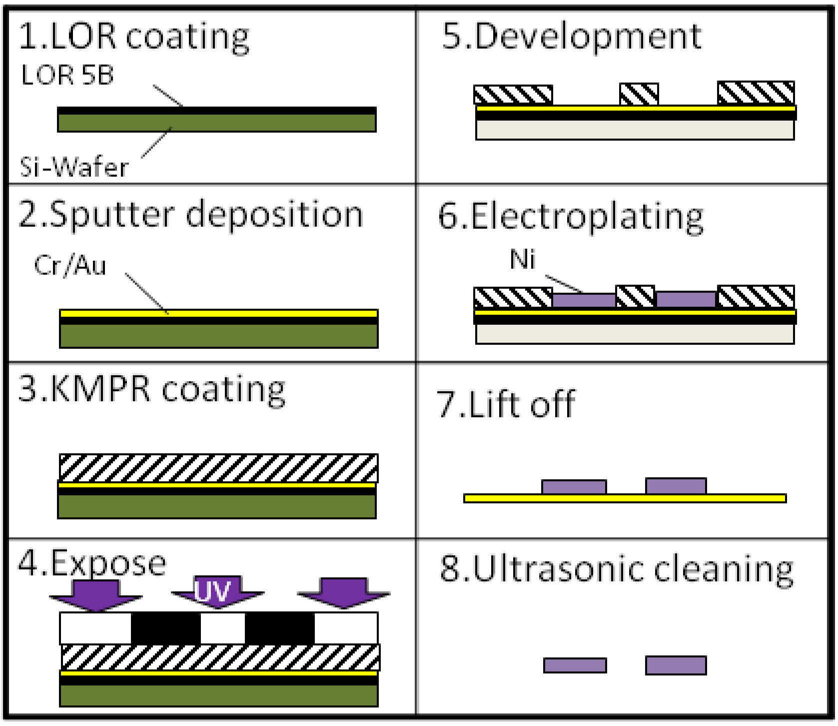

Figure 3.4 Fabrication process of a nickel-based MMT.

3.2.2 Experimental evaluation for following response

The experiment has been conducted to evaluate two driving methods, TMD and HPD as well as the conventional drive method. Figure 3.5 shows the experimental set up including the linear stage for the magnet actuation, the microscope with CCD camera, and PC for controlling the stage and capturing image data from CCD camera. Ni based ϕ 1.0 mm × 0.05 mm circular disc is used as an MMT and a neodymium based ϕ 1.0 mm × 1.0 mm cylinder magnet is used as a drive unit. The magnet is commercially available and its surface magnetic flux density is 166 mT (grade: N40).

Figure 3.6 shows the experimentally obtained following response ability of the MMT against the linear stage with the permanent magnet. The stage moves in 1 degree of freedom (DOF) with 0.5 Hz sine wave and the stroke is ± 1.4 mm. In the case of conventional drive, the

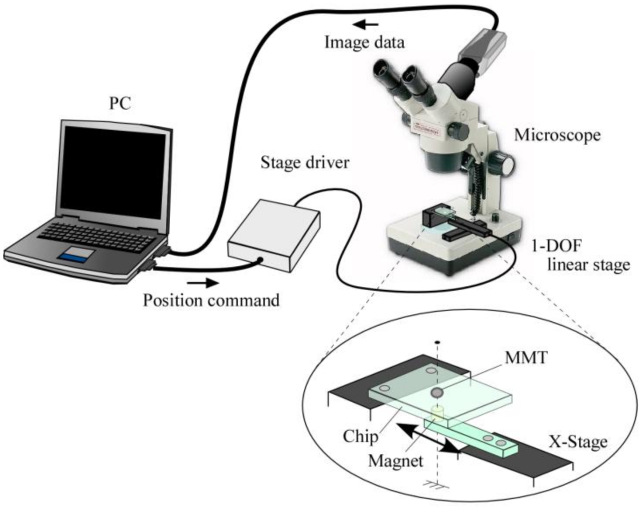

Figure 3.5 Experimental setup.

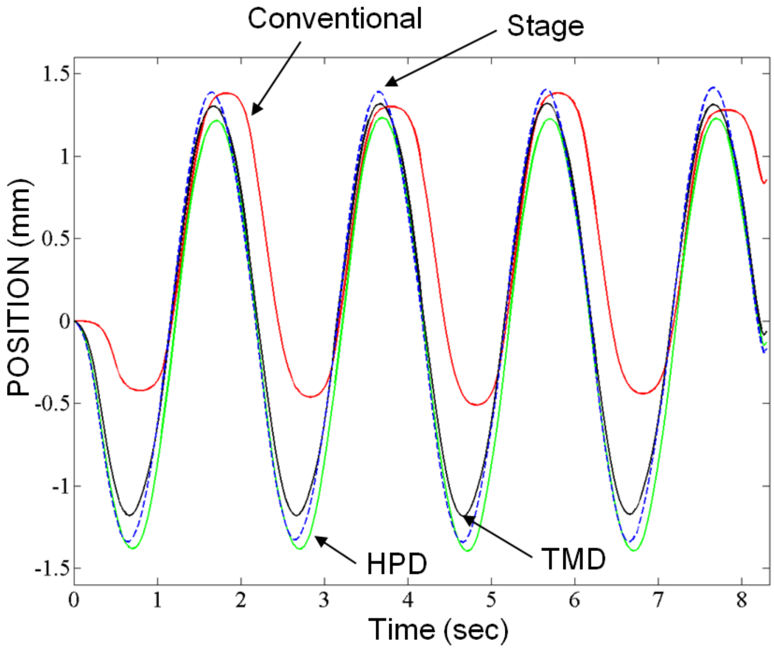

Figure 3.6 Following response of the MMT to the linear stage in three different driving unit (magnet: neodymium, ϕ1.0×1.0 mm; MMT: nickel, ϕ1.0×0.05 mm)

movement of the MMT against the stage is delayed by 0.3 sec; the maximum difference between the MMT and the stage is 1.0 mm. Under this large time lag, the MMT cannot

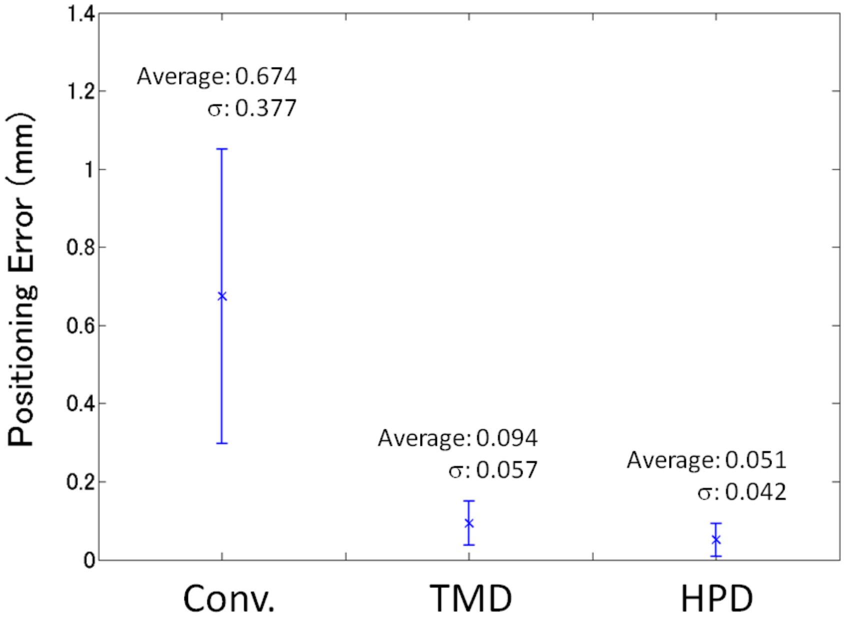

Figure 3.7 Positioning error between the drive magnet on the linear stage and the MMT in each drive method

respond to the cell movement in a microfluidic chip and this makes the development of an automation system difficult. On the other hand, in both of the TMD and HPD, the response of the MMT is more than 10 times faster. Figure 3.7 shows the comparison of the MMT positioning error against the drive magnet. Comparing to the positioning error in the conventional drive, the average error is 5 times smaller in TMD and 10 times smaller in HPD. Precise positioning accuracy and following response to stage are essential for developing automation systems as well as the manipulation of small size of objects.

In the meanwhile, the difference between the stage and the MMT tends to get worse around the returning points, which is the stage speeds smaller. This result implies that the friction on the MMT has velocity dependence. According to the Stribeck curve in fluid lubrication field, in boundary lubrication region or mixed film lubrication region, where the liquid film thickness is smaller than surface roughness of the MMT, the more the velocity increases, the more liquid film thickness increases in boundary lubrication conditions [100, 101]. And as a result, the friction decreases. Therefore, the friction on the MMT exceeds the drive force around the returning point since the velocity is close to zero and the MMT start delaying to the stage.

3.2.3 Experimental evaluation for output force

In order to evaluate the efficiency of the drive method, comparison of the force ratio of driving force (F_{DRIVE}) to the friction force ($F_{FRICTION}$) is effective. From force balance, the output force of the MMT F_{OUT} can be calculated by the following;

$$F_{OUT} = F_{DRIVE} - F_{FRICTION} = F_X - \mu \cdot F_Y \qquad (3.1)$$

where F_X and F_Y are horizontal and vertical components of the magnetic force respectively, and μ is friction coefficient. Also, the output force of the MMT on the different surface can be calculated by the equation (3.2).

$$F'_{OUT} = F_X - \mu' \cdot F_Y \qquad (3.2)$$

From equation (3.1) and (3.2), the drive force of the MMT F_{DRIVE} and friction force $F_{FRICTION}$ can be calculated.

Figure 3.8 shows the output force of the MMT (ϕ 1.0 mm sphere steel) actuated by neodymium magnet (ϕ 1.0×1.0 mm) measured by the load cell (Kyowa, LVS-5GA) for two different surfaces (glass and clean paper). The friction coefficients of the glass and paper are 0.11 and 0.18 respectively. The absolute value of the output force by HPD is much lower than conventional drive, but the reduction of the force is smaller when the friction coefficient increases. From this result, the force ratio of the driving force to the friction force (F_{DRIVE} / $F_{FRICTION}$) is 3.27 in conventional drive while it is 5.57 in HPD which is 1.7 times higher than the conventional drive. Since the drive force of the MMT in HPD is fairly higher than the

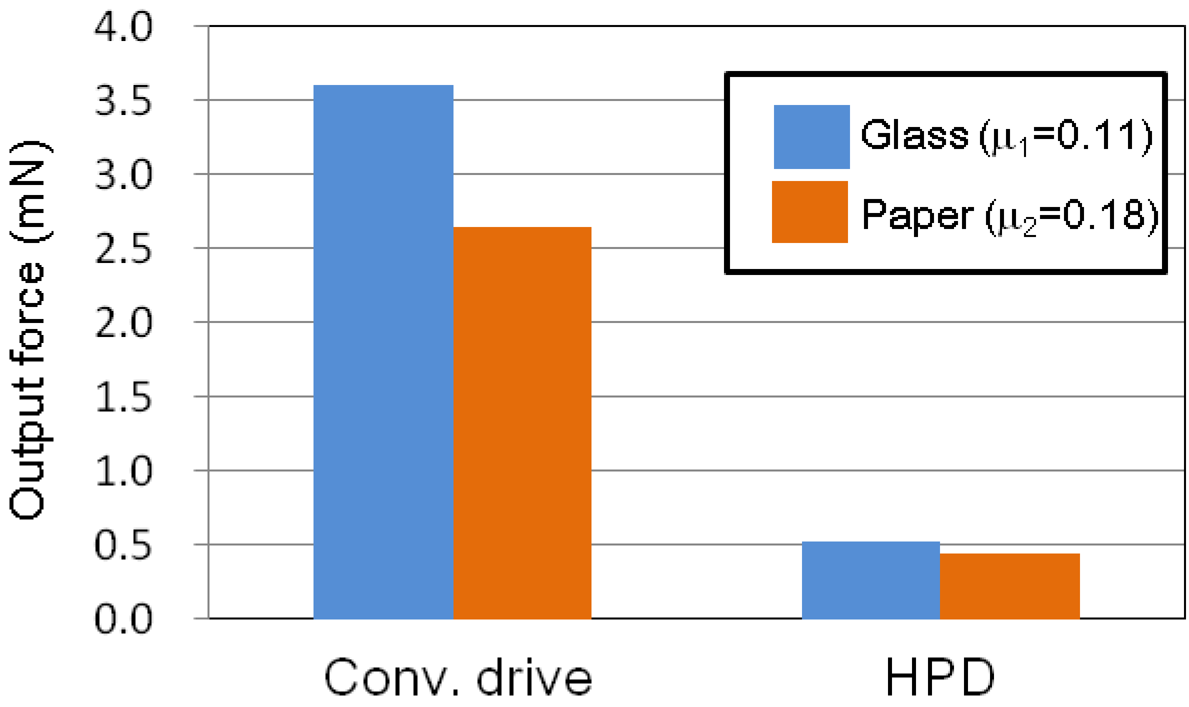

Figure 3.8 Output force of the MMT *(ϕ* 1.0 mm steel sphere) by the conventional drive and the HPD on two different surfaces (glass and clean paper).

friction force, MMT can follow to the drive magnet more precisely than in the case of conventional drive.

3.3 Developing HPD for Multi-DOF MMT

3.3.1 Concept and design of multi-DOF MMT

Although TMD and HPD effectiveness is clear in MMT actuation, both methods are only available of 1 DOF. Few applications for cell manipulations can be conducted in 1 DOF. In order to manipulate biological cells freely in a microfluidic chip, it is important for precise actuation in multi-DOF. We thus extended the HPD to precise multi-DOF control actuation by combining four permanent magnets under HPD conditions.

Figure 3.9 (a) shows the concept of the 2-DOF MMT driven by HPD, and Figure 3.9 (b)

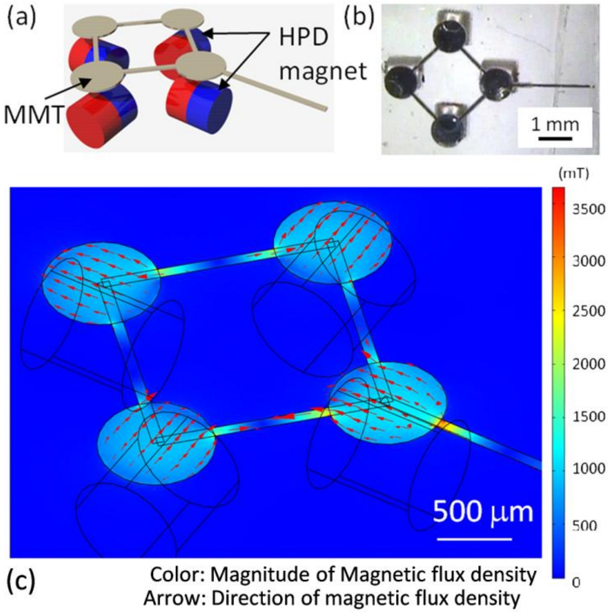

Figure 3.9 Multi-DOF MMT (a) concept, (b) actual design, (c) FEM analysis of magnetic flux

shows the actual design. Two pairs of magnets under the HPD conditions are set with the polar axis normal to each other. The cell manipulation is conducted on the head of the extended part. Figure 3.9 (c) shows the FEM result of the magnetic flux density for the 2-DOF MMT. It can be seen that the drive magnets independently actuate the circular disc part of the MMT as it is shown in Figure 3.3.

It is quite important to align four magnets and keep the certain distance between them in order to obtain full advantage of the assembled HPD. Therefore, the fixture of the permanent magnets has to be precise fabrication, but it is difficult to produce accurate 1 mm^3 size magnet fixture by machining. Therefore, stereolithography was employed to obtain precise 3 dimensional shape. Figure 3.10 shows the fixture of the four permanent magnets in order to align and keep the HPD conditions. The fixture was made by 3D stereolithography using EDEN 250 (SHACOH Co.) and four neodymium magnets were assembled on the fixture manually.

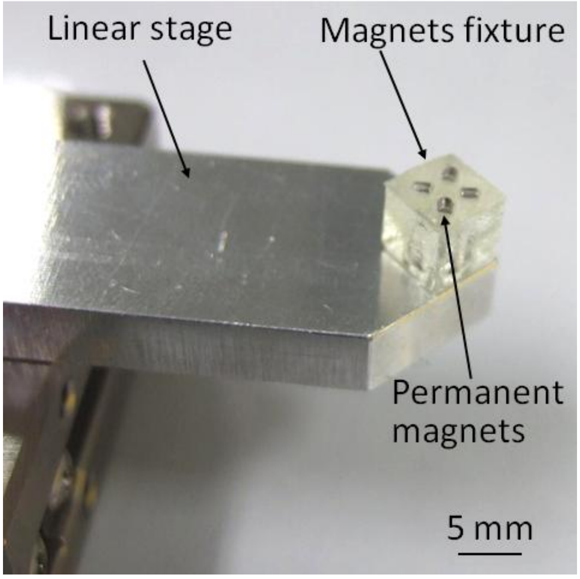

Figure 3.10 Permanent magnets fixture made by stereolithography (EDEN 250)

3.3.2 Experimental evaluation for multi-DOF movement

In evaluation experiments on multi-DOF MMT positioning accuracy, the linear stage was actuated in a circular trajectory under open loop control with constant drive velocity, then corresponding MMT positioning was measured by a CCD camera (radius: 0.5 mm) at a linear stage drive velocity of 1.57 mm/s (3.14 rad/s) on the x-y plane.

Figure 3.11 (a) shows results for a conventional drive (MMT: 1.0 mm diameter circular disc, single neodymium magnet): MMT movement does not follow the target trajectory. Average of the absolute positioning error from the target in this case was 290 μm the standard deviation 90 μm and maximum error 402 μm. Under this huge error, it is impossible to control microsize objects. Figure 3.11 (b) shows multi-DOF HPD results (design in Figure 3.9). Average of the absolute positioning error of the MMT from the target trajectory was 84 μm, standard deviations 28 μm, and maximum error of 50 points 125 μm.

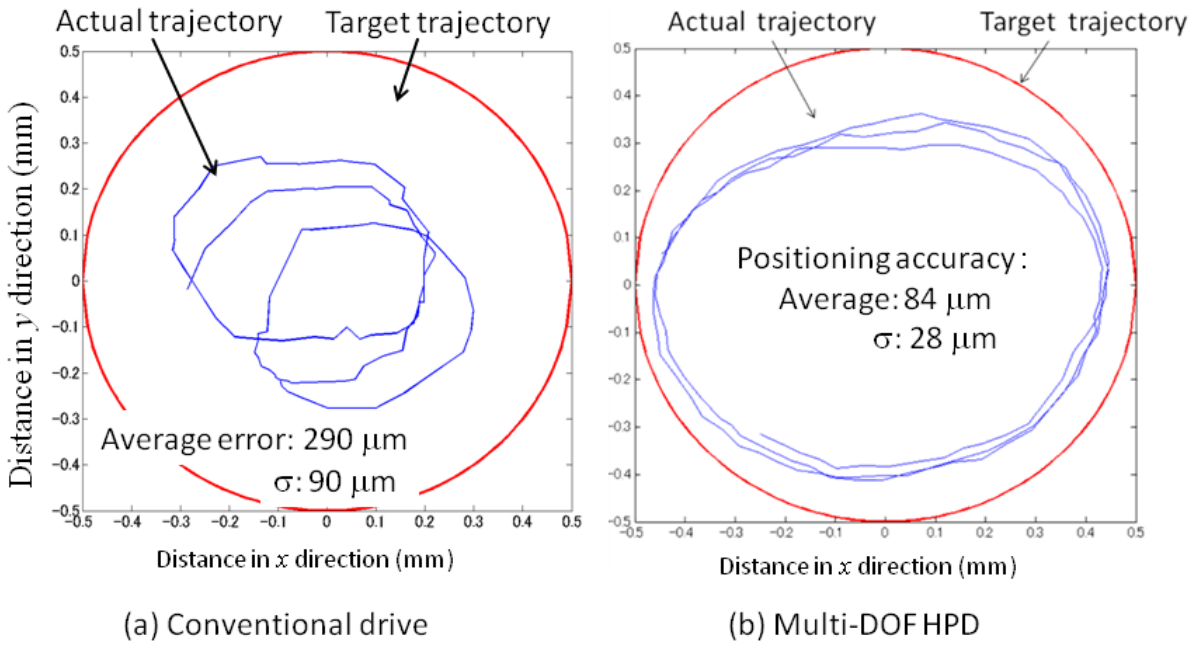

(a) Conventional drive (b) Multi-DOF HPD

Figure 3.11 Evaluation for positioning accuracy of MMT in 2-DOF (a) conventional drive (MMT: 1.0mm circular disc, magnet: single neodymium magnet), (b) assembled HPD (MMT: designed in Figure 3.9, magnet: four assembled HPD).

3.4 Conclusion Remarks

In this chapter, the root cause of the large friction on an MMT in conventional drive was confirmed as large downward force on the MMT. Two distinguished driving methods, Two-Tiered Magnetic Drive (TMD) and Horizontal Polar Drive (HPD), were developed to reduce the vertical component of the magnetic force from a permanent magnet. The effectiveness was validated experimentally as well as analytically.

In order to extend these driving to multi-degree of freedom, four permanent magnets are assembled in HPD conditions and it achieved same accuracy as 1 DOF in 2 DOF. The amount of dead band reduced and thus accuracy increased significantly comparing to the conventional drive. However, the absolute values of these driving are still more than 50 μm, which is far from precise cell manipulations.

Therefore, other approaches to reduce friction on an MMT are required while multi-DOF HPD is employed. Next two chapters present different approaches, which are compatible with HPD, to reduce friction on an MMT.

Chapter 4.

Friction Reduction by Ultrasonic Vibrations

4.1 Driving Principle

When the ultrasonic vibration is applied to the sliding surface of a moving object, the direction of the friction on the object switches from ten thousand to a million times per second and as a result, the effective friction decreases significantly [102-106]. Littmman et al.[104, 105] developed an analytical model to explain the phenomena of the friction reduction and demonstrated that the reduction ratio depends on the velocity ratio of the moving object and the sliding surface. Kumar et al. also developed an analytical model and expressed the friction reduction ratio. As shown in Figure 4.1 (a), body A is assumed to slide with a constant velocity V_s over body B. When the instantaneous velocity of B, $V(t)$, is greater than V_s the friction force F will reverse its direction and acts in the same direction as V_s (Figure 4.1 (b)).

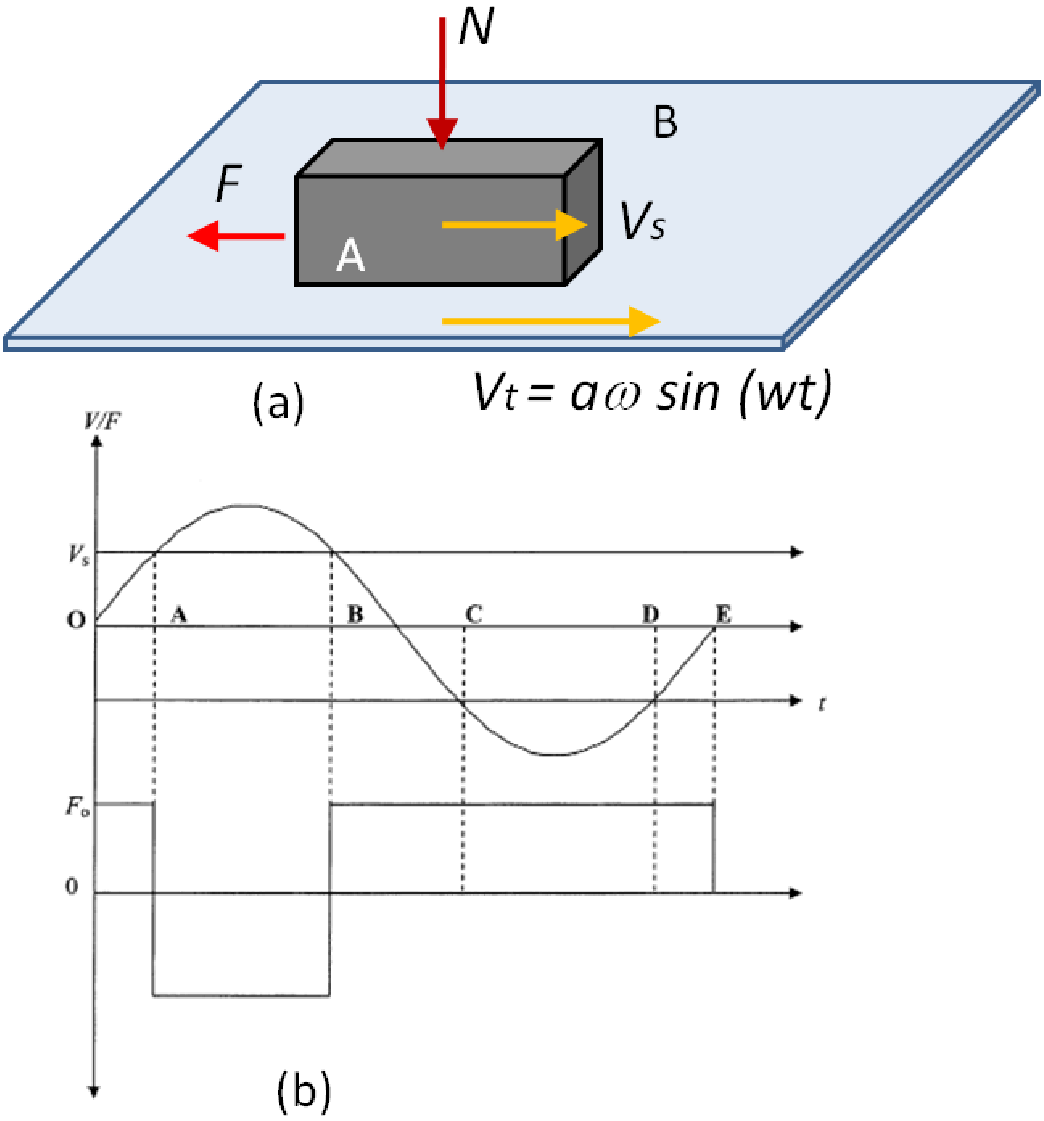

Figure 4.1 Principle of friction reduction by ultrasonic vibrations (a) concept. (b) Variation of vibration velocity with time and corresponding change in direction of frictional force [106].

The friction reduction ratio of resultant average friction F_a over frictional force in the absence of the vibration F_0 is expressed as follows [106];

$$\frac{F_a}{F_0} = \frac{2}{\pi} \sin^{-1} \frac{V_s}{a\omega} \approx \frac{2 \cdot V_s}{\pi \cdot a\omega} \qquad (4.1)$$

where a and ω are the amplitude and the angular frequency of the vibration respectively.

As discussed in previous sections, friction in microscale is the dominant contributor in the deterioration of the positioning accuracy due to the scale effect. Thus, the friction reduction by vibration can be expected to have a considerable impact on the positioning accuracy in microscale. Here, we apply this phenomenon to the microfluidic chip to reduce the effective friction on the MMT considerably. Figure 4.2 shows the driving concept of the MMT with ultrasonic vibration. Radially displaceable piezoelectric ceramic is attached to the glass substrate under the microfluidic chip and oscillates the sliding surface of the MMT. The MMT is actuated by permanent magnets whose axis is set to the horizontal direction and the permanent magnet is placed on the 2-DOF linear stage.

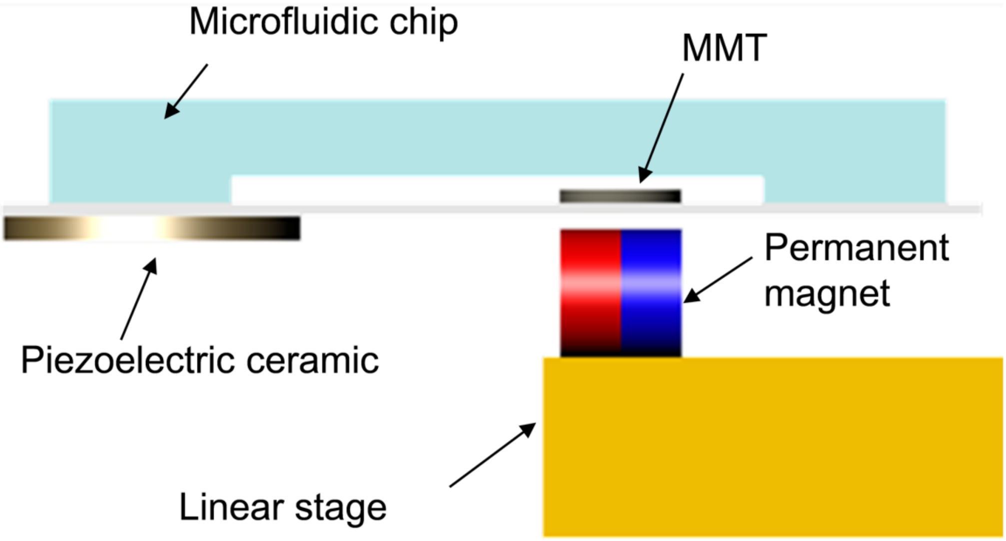

Figure 4.2 Driving concept of the MMT actuated by permanent magnet with ultrasonic vibration. Oscillating the grass substrate by the piezoelectric ceramic reduces the effective friction on the MMT.

4.2 Evaluation Experiments

4.2.1 Experimental setup

In the previous section, we discussed the driving method by horizontally arranged permanent magnets, which is called horizontal polar drive (HPD), and improved the positioning accuracy by reducing the friction on the MMT. Since the friction reduction method by ultrasonic vibration is compatible HPD, the same design as Figure 3.9 was employed for the evaluation experiments.

Commercially available piezoelectric ceramic (W-40, MKT Taisei Co.), of dimensions ϕ42.0 × 3.5 mm was used in the experiments in order to reduce the effective friction on the MMT and improve the positioning accuracy. The resonance frequency of the ceramic was 55 kHz, and the electrostatic capacitance was 4600 pF. Figure 4.3 shows the frequency characteristic of the piezoelectric ceramic under different applied voltages. It can be seen that the vibration amplitude is significantly increased around the resonance frequency and the magnitude is approximately 1.4 μm when 300 $V_{p\text{-}p}$ (peak to peak) AC voltages is applied. Therefore, it is assumed that the vibration amplitude is not large enough to affect the cell manipulation when the ceramic mentioned above is used. Four neodymium (Nd2Fe14B) magnets (diameter: 1.0 mm, grade: N40) were employed as a drive magnet. Figure 4.4 shows the experimental setup. Piezoelectric ceramic was attached to the glass substrate to induce the ultrasonic vibration. The four permanent magnets were placed on the same fixture as Figure 3.10 made by stereolithography. Then, the magnets were actuated by the 2-DOF linear stage and the MMT was operated in a microfluidic chip. The position of the MMT was measured through CCD camera attached to the microscope and the position of the stage (or magnet) was recorded by encoder from the linear stage.

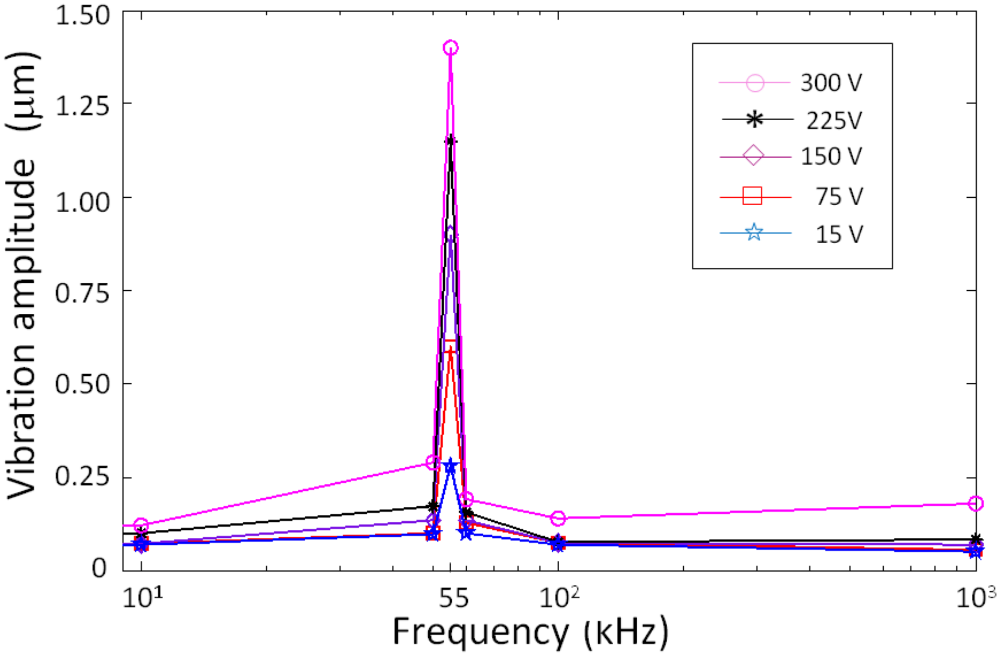

Figure 4.3 Frequency characteristics of the piezoelectric ceramic (W-40, MKT Taisei Co.). The resonance frequency is 55 kHz and the peak vibration amplitude is 1.4 μm when 300 $V_{p\text{-}p}$ is applied

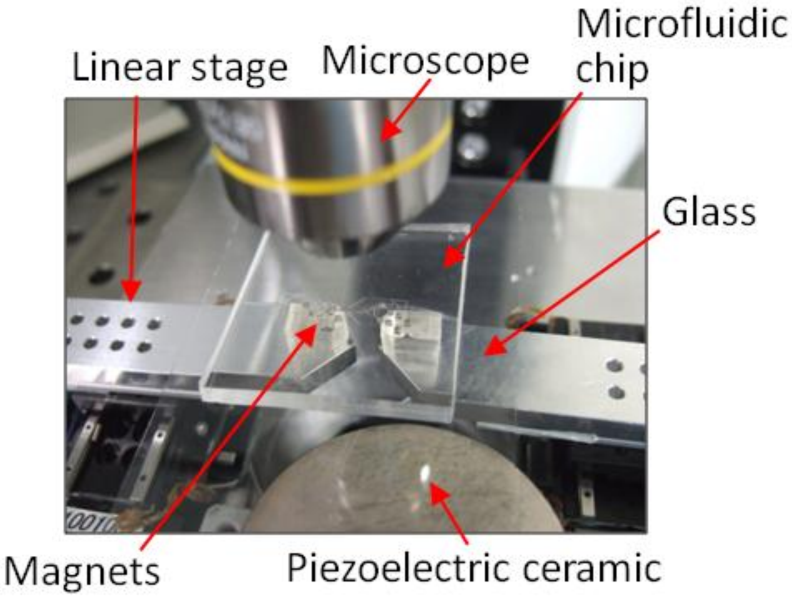

Figure 4.4 Experimental setup. Piezoelectric ceramic is attached to glass substrate and MMT is actuated by four HPD permanent magnets beneath the microfluidic chip

4.2.2 Evaluation of the effect of the ultrasonic vibration for the MMT accuracy

An experiment was conducted in order to evaluate the effect of the ultrasonic vibration and the improvement of the MMT positioning accuracy. The linear stage was actuated in a circular trajectory with the constant drive velocity and the corresponding MMT positions were measured by CCD camera. The four of ϕ 1.0 mm × 1.0 mm columnar neodymium magnets were used as the drive unit. Figure 4.5 shows the MMT positioning accuracy with vibration by piezoelectric ceramic against the target trajectory of the circular (radius: 0.5 mm). The drive velocity of the linear stage was 0.785 mm/sec in x-y direction and the 300 $V_{p\text{-}p}$ was applied to the piezoelectric ceramic with 55 kHz frequency. The measurements were conducted in 100 points. Comparing to the without vibration case (Figure 3.11 (b)), the MMT movement was significantly improved. The drive stage configuration was same as Figure 3.11 but the maximum error between the targets to the actual trajectory was approximately 10 μm, which was more than 10 times greater accuracy than in the case without vibration.

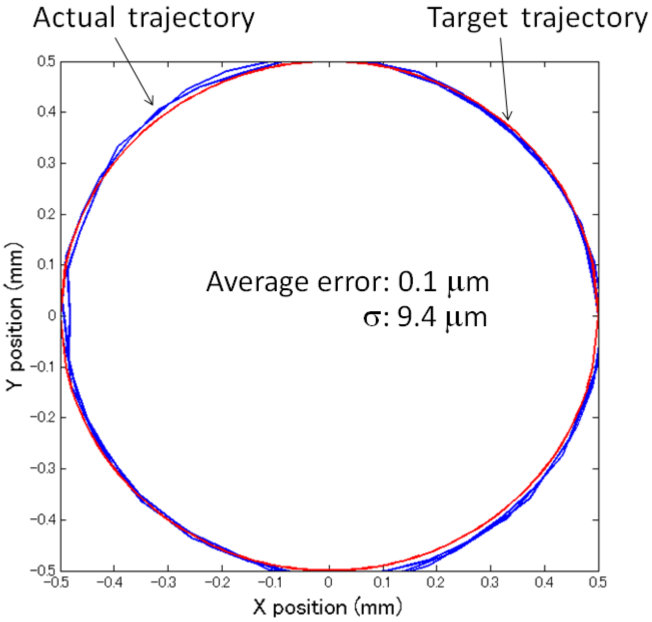

Figure 4.5 Positioning accuracy of the MMT with vibration from piezoelectric ceramic (frequency of the piezoelectric ceramics: 55 kHz drive frequency of the stage: 0.5 Hz)

Note that the total positioning accuracy included not only the MMT positioning error, but also other factors such as the measuring error and the stage positioning error. The measuring error was approximately 4 μm due to 2.5 μm per pixel of the display from CCD camera and the linear stage positioning error was approximately 5 μm. Thus, the positioning error of the MMT itself under the above conditions can be calculated by root-mean-square error as follows;

$$e_{MMT} = \sqrt{e_{total}^2 - e_{measure}^2 - e_{stage}^2} = 7.0 \quad \mu m \qquad (4.2)$$

where e_{total} is total positioning error of the MMT against target, $e_{measure}$ is the measuring error, e_{stage} is the stage positioning error against the input command and the e_{MMT} is the positioning error caused by the MMT drive itself.

According to the equation (4.1), the friction reduction ratio is a function of the vibration amplitude and the velocity of the MMT. Figure 4.5 shows maximum error of the MMT itself (e_{MMT}). The error e_{MMT} was calculated by equation (4.2) after 100 points measuring by CCD camera under various applied voltages (15, 75, 150, 225 and 300 $V_{p\text{-}p}$) to the piezoelectric ceramic and under various drive velocities (0.16, 0.47, 0.79, 1.57, 2.36, 3.14, 3.93, 4.71 and 5.50 mm/sec) of the stage respectively and the data were interpolated by cubic spline curves.

The positioning error increases with increasing stage velocity, and decreases with increasing applied voltage, which represents the vibration amplitude at the sliding surface. In the case without vibration, the result corresponds to the stribeck curve [100, 101] and it is reasonable that the positioning error increase according to the friction. The result in the case with vibration broadly corresponds to equation (4.1); however, the positioning accuracy with lower applied voltages is more precise than when a higher voltage is applied in the region of the low stage velocity. This can be attributed to the fact that the positioning accuracy is nearing the amplitude of the vibrations. In fact, the positioning accuracy of the MMT is 1.1 μm when the applied voltage is 15 V_{p-p} and the stage velocity is 0.16 mm/sec, but it is impossible to achieve this accuracy when applied voltage is 300 V_{p-p} due to ±1.4 μm displacement of the piezoelectric ceramic as shown in Figure 3 (d). Consequently, the error at 0.16 mm/sec stage velocity became less than 1 percent of the case without vibration when 15 V_{p-p} is applied.

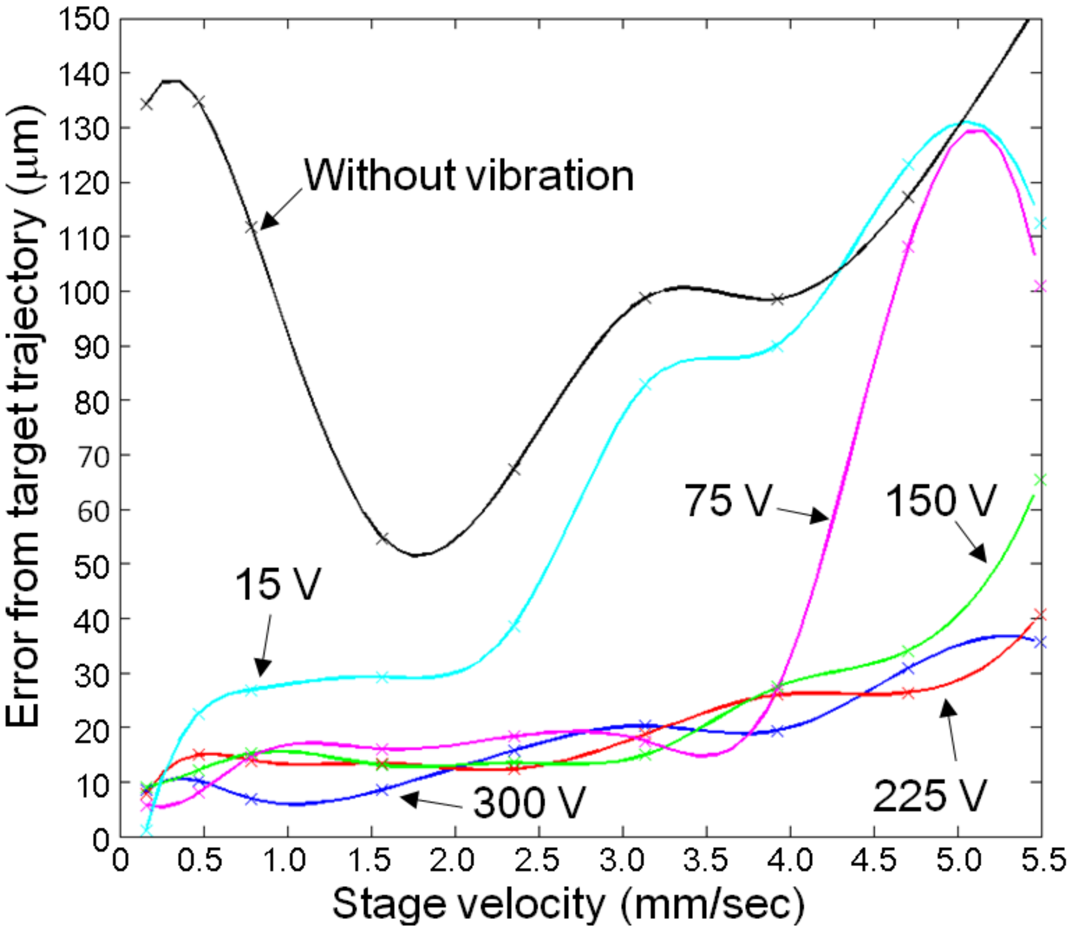

Figure 4.6 Correlation of the positioning error and drive velocity in different applied voltages (applied frequency to the piezoelectric ceramic: 55 kHz)

4.2.3 Evaluation of the effect of the ultrasonic vibration on the MMT actuation speed

In addition to the achievement of the micrometer order positioning accuracy, other benefits of the ultrasonic vibration can be also observed. The response speed was increases as well because of the significantly decreased friction on the MMT. Figure 4.7 shows the frequency response characteristic of MMT when the stage moves 1.0 mm stroke of 1 DOF. 150 $V_{p\text{-}p}$ was applied to the piezoelectric ceramics. When the stage frequency exceeds 3 Hz, the following capability of the MMT to the stage gradually deteriorated. Figure 4.8 shows the high speed MMT movement in 3-DOF (x-y-θ) with ultrasonic vibration. Consequently, the high speed actuation in 3-DOF leads to the high throughput operation in a microfluidic chip.

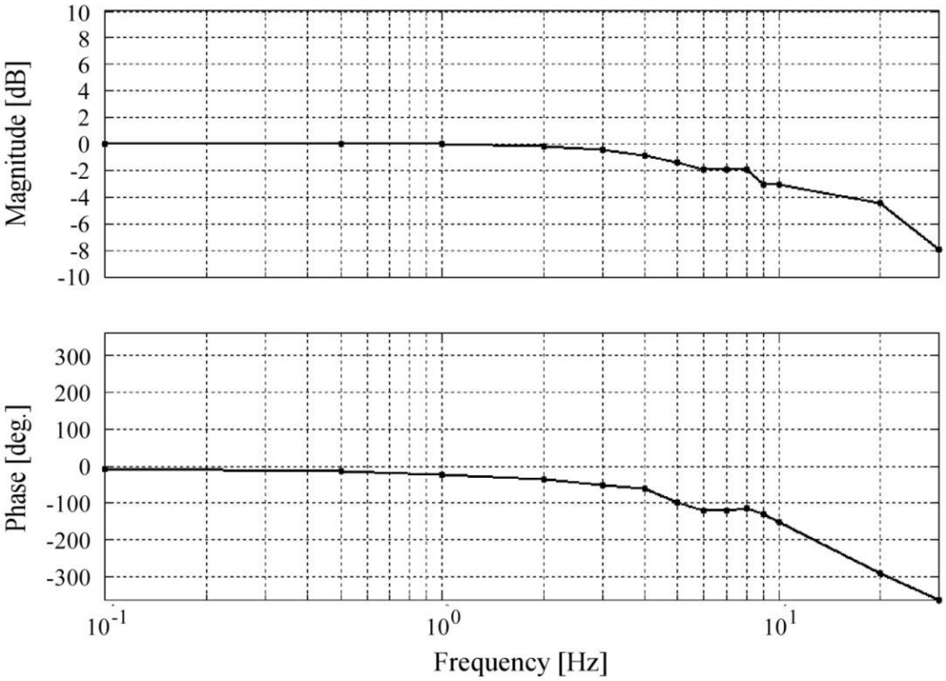

Figure 4.7 Frequency response characteristic of MMT when stage moved 1 DOF with 1.0 mm stroke.

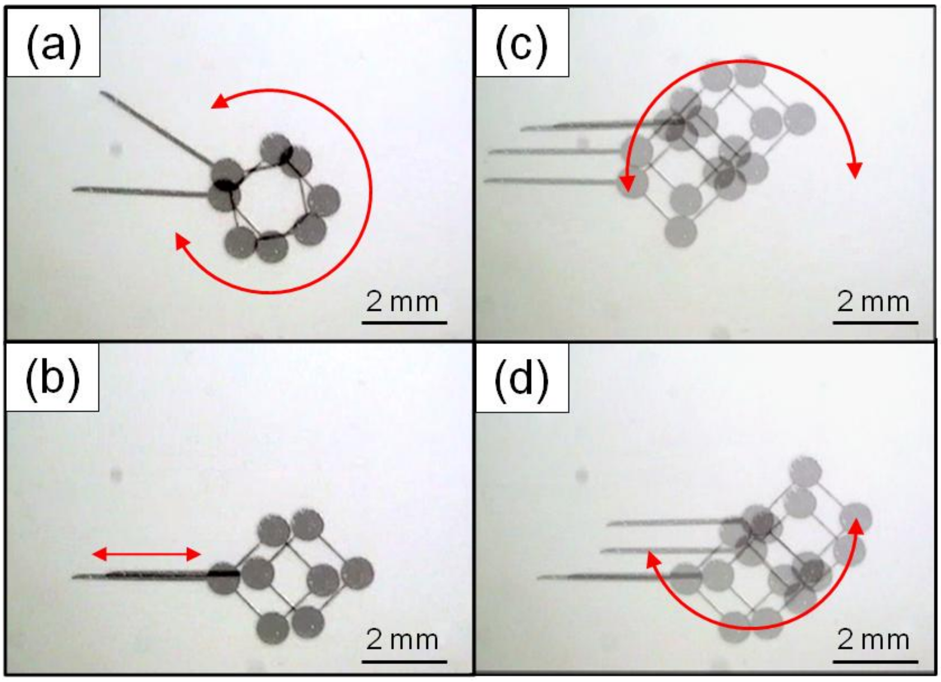

Figure 4.8 High speed 3-DOF movement of MMT (rotation speed: 500 rpm, 5 Hz in x-y)

4.2.4 Evaluation of the effect of the ultrasonic vibration for the output force

The output force of the MMT is also experimentally evaluated by the loadcell (LVS-5GA, Kyowa Electronic Instruments Co. Ltd). Figure 4.9 shows the output forces of the MMT with and without ultrasonic vibration respectively. The drive unit and MMT configuration was same as Figure 3.11. The output force of the MMT with ultrasonic vibration (150Vp-p, 55 kHz) increased twice as much instead of the friction reduction. Comparing to the other microactuators, the output force of the MMT is considerably higher and it can reach in the order of mN force. Increasing the capacity of the maximum force enables the MMT to apply to the force requirement tasks, such as a cell cutting operation and mechanical stimulation to the microorganism.

High power output and precise positioning accuracy allows the MMT to be employed in a

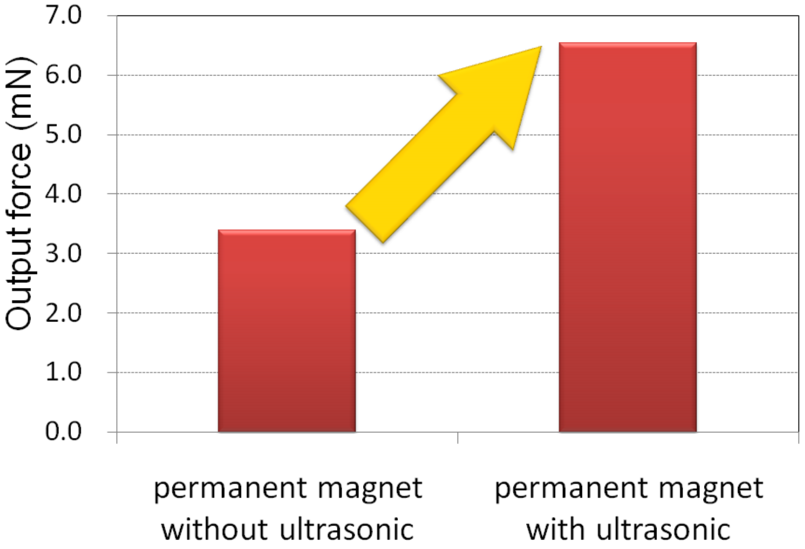

Figure 4.9 Experimentally measured output forces with and without vibration.

wide range of applications like commercialized micromechanical manipulators. The differences are that the size of the manipulator is tiny for the MMT and it can be actuated in a microfluidic chip. A closed environment supplies the less disturbance atmosphere to prevent cell contamination and miniaturization of the manipulator leads to the high throughput of the operations [87].

Based on the above measurement result and Kumars' equation (4.1), the actual friction on the MMT can be calculated as follows;

$$F_0 / F_a \approx \frac{\pi}{2} \frac{a\omega}{V_s} \qquad (4.1)$$

$$F_{OUT} = F_{Drive} - F_0 \qquad (4.3)$$

$$F'_{OUT} = F_{Drive} - F_a \qquad (4.4)$$

Here, the unknown variables are the drive force from the permanent magnet (F_{Drive}), the friction amount without vibration (F_0), and friction amout with vibration (F_a). We can calculate the unknown variables from the equation (4.1), (4.2), (4.3). Figure 4.10 shows the calculated friction amount F_0 and F_a. Owing to the friction reduction by ultrasonic vibration,

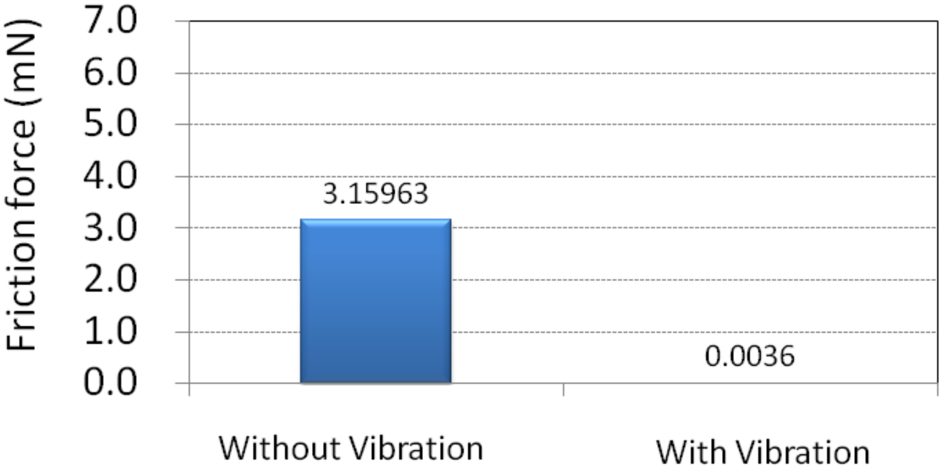

Figure 4.10 Calculated friction forces with and without vibration.

the friction decreased by thousandth part of the original friction amount from 3.2 mN to 3.6 μN.

4.2.5 Vibration toxicity test for biological cells

The friction reduction counts for nothing if the applied vibration makes negative effects on cells. Thus, the vibration toxicity test was conducted by examining cell propagation. Six wells of Chondrocytes (5000 cells / well) were prepared and cultured in incubator for 24 hours in advance. The vibration with 55 kHz frequency and 1.2 μm amplitude was applied to three of them after 6, 12, 24, 48, 72 hours for 10 minutes respectively and nothing applied to the others. The WST-8 assay (Cell Counting Kit-8, Dojindo Co.), which is commonly used for cell toxicity test, was added to the wells and the absorption of light with 450 nm wavelength was measured by plate reader in order to count the number of live cells [107, 108]. Figure 4.11 shows the comparison of the cell propagation with and without vibration. According to this result, there is no difference in cell growth rate between the groups with and without vibration. It implies that the vibration does not give negative effect on the cell groth. This result indicates that the vibration is applicable to cell manipulation since the actual duration of the vibration is only few seconds per cell.

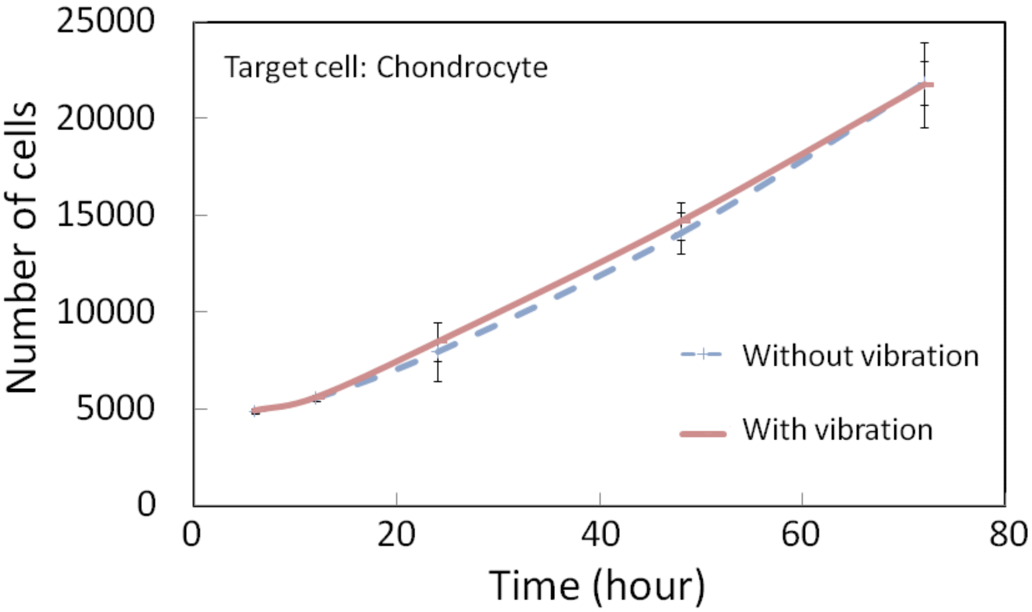

Figure 4.11 Vibration toxicity test result for cells (target cell: chondrocyte).

4.3 Conclusion Remarks

In this chapter, we described an innovative drive method for MMTs actuated by permanent magnets with ultrasonic vibration applied to the microfluidic chip. The positioning accuracy improved by up to 100 times than in the case of without vibration. The minimum positioning accuracy for the MMT itself was 1.1 μm. In addition to the precision, response speed was also improved and high speed actuation in 3-DOF (x-y-θ) was achieved. The vibration also increased the output force of the MMT as well as friction reduction and we validated the MMT could output several millinewtons. A wide range of applications for cell manipulations can be achieved in a microfluidic chip owing to the high power output (mN order), high precision (μm order).

However, there are several weaknesses of this drive method. 1. The friction reduction ratio depends on the relative velocity between the MMT and oscillated glass substrates. Therefore, the MMT positioning error increases when the MMT velocity increases and it reaches more than 100 μm in high speed region. This attribute of the vibration restricts precise cell manipulation by MMT with high speed.

In addition, large amplitude of vibration gives MMT more stable accuracy in high speed region, but it makes cells vibrate as well. Therefore, it becomes difficult to operate precise cell manipulation. Thus, it is better to keep low amplitude of vibration and combine another friction reduction method to achieve precise cell manipulation with high speed.

Chapter 5.

Friction Reduction by Three-Dimensionally Patterned Surface on the MMT

5.1 Principle and Designing of Riblet Surface on the MMT

5.1.1 Introduction

Previous two chapters discussed to reduce the friction on the MMT by developing the drive unit, and relative movement of the substrate. As a result, the MMT achieved to obtain minimum 1.1 μm precise accuracy and several mN high power output force. However, as known as equation (4.1), the friction reduction ratio depends on the MMT velocity and it decreases when the velocity of the MMT increases. In fact, the error between the MMT and the stage considerably increased when the stage velocity reaches more than 3.1 mm/sec (3 Hz) as shown in Figure 4.6 and 4.7. Therefore, another friction reduction method is required in order to achieve high speed, high precision, high power actuation.

Furthermore, the MMT in previous chapters was made by nickel, which is not bio-compatible material in general. In addition, the fabrication of MMT was based on nickel electroplating, which is difficult to achieve precise fabrication accuracy and complex three dimensional shape. On the other hand, it is well known that Si is bio-compatible material and flexible fabrication can be achieved.

Here, we propose new type of MMT composed of hybrid structure of Ni and Si. Taking advantage of flexibility of Si fabrication, three dimensionally patterned surface is produced on the MMT in order to reduce fluid friction on the MMT. Figure 5.1 shows the concept of Si-Ni hybrid structure MMT. Nickel remains same at the actuation part in order to obtain strong magnetic force from the permanent magnet, but Si is surrounding nickel to have bio-compatibility when the MMT manipulates biological cells. In addition, regularly arrayed V groove, which is called “riblet”, is patterned on the MMT and it reduces fluid friction force on the MMT. As a result, MMT can achieve high power output from the permanent magnet, precise accuracy at ultrahigh speed region as well. It leads to high throughput cell manipulations in a microfluidic chip.

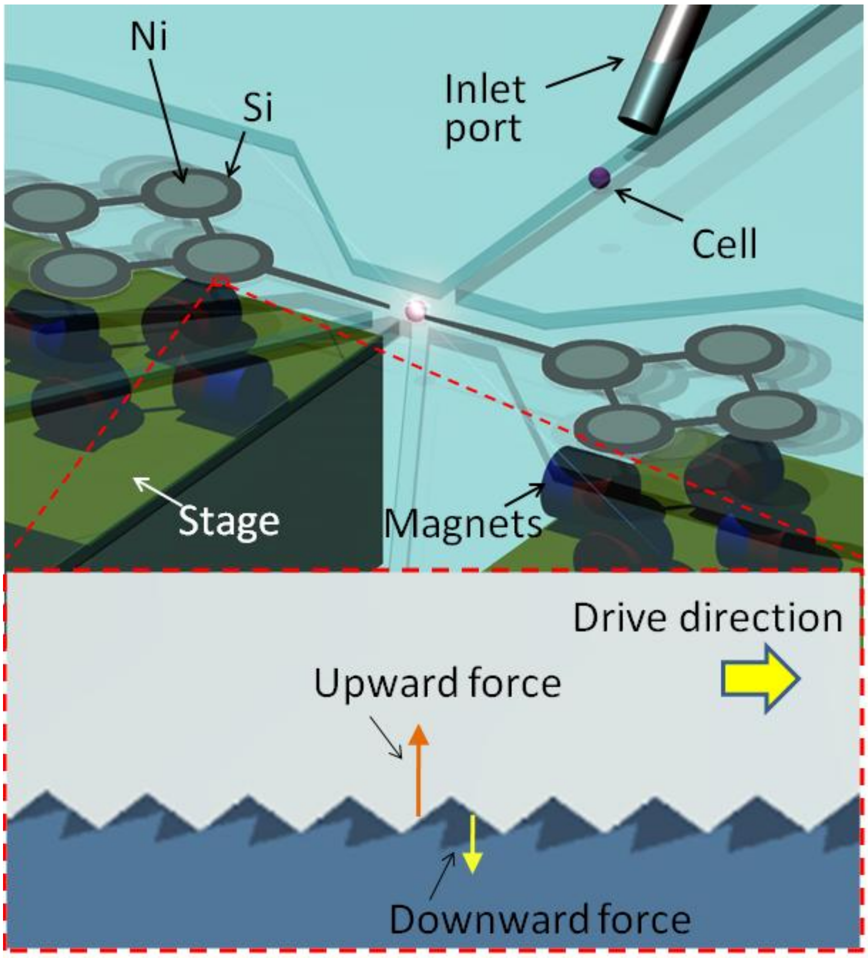

Figure 5.1 Concept of the riblet surface on the MMT

5.1.2 Principle of the fluid friction reduction by riblet surface

The riblet shape, which is regularly arrayed V groove and also known as shark skin, is practically used for airplane and ship to reduce fluid friction force [109-111]. The basic principle to reduce fluid friction force by riblet is that squeezing liquid by the V groove generates upward fluid force on the riblet surface and it makes the lubricant film thickness increase. As a result, the shear stress from the wall reduces and the fluid friction force decreases. Here, the fluid pressure analysis is conducted to understand the principle of the riblet surface and lead to optimizing the riblet shape in order to minimize the fluid friction on the MMT.

Figure 5.2 shows the definition of the variables for the riblet. In order to simplify the calculation, the front surface to velocity direction is classified as Region I, and back surface is classified as Region II.

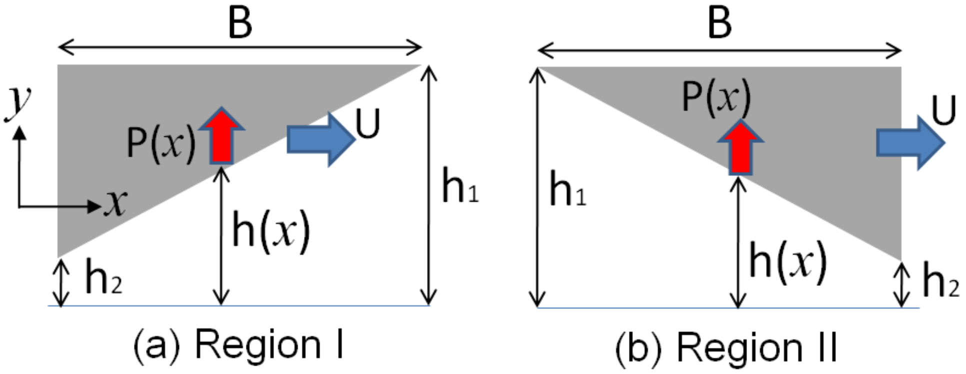

Figure 5.2 Definition of the variables for the riblet

The height *h(x)* at arbitrary position *x* is expressed as flows;

$$h(x) = h_1 - (h_1 - h_2)\frac{x}{B} = h_1\{a - (a-1)\cdot \bar{x}\} \qquad (5.1)$$

$$\because a = h_1/h_2, \qquad \bar{x} = x/B$$

By derivation of equation (5.1), we obtain

$$dx = -\frac{B}{h_2(a-1)}dh \qquad (5.2)$$

Here, we assume that the fluid pressure at boundaries of the Region I and Region II is 0, that is P(0) = P (B) = 0. Then, the following is derived from Reynolds equation.

$$\frac{d}{dx}\left(\frac{h^3}{\eta}\frac{dP}{dx}\right) = 6U\frac{dh}{dx} \qquad (5.3)$$

where η is viscosity resistance.

For $I_2(x) = \int_0^x \frac{dx}{h^2}$, $I_3 = \int_0^x \frac{dx}{h^3}$, $h_m = \frac{I_2(B)}{I_3(B)}$,

$$I_2(x) = \frac{B}{h_2(a-1)}\left(\frac{1}{h} - \frac{1}{h_1}\right), \quad I_3(x) = \frac{B}{2h_2(a-1)}\left(\frac{1}{h^2} - \frac{1}{h_1^2}\right)$$

And $h_m = \frac{I_2(B)}{I_3(B)} = \frac{2h_1h_2}{h_1 + h_2}$

$$\begin{aligned} P(x) &= 6\eta U\{I_2(x) - h_m I_3(x)\} \\ &= 6\eta U\left[\frac{B}{h_2(a-1)}\left(\frac{1}{h} - \frac{1}{h_1}\right) - \frac{2h_1h_2}{h_1+h_2}\left\{\frac{B}{2h_2(a-1)}\left(\frac{1}{h^2} - \frac{1}{h_1^2}\right)\right\}\right] \end{aligned} \tag{5.4}$$

To simplify the equations, we set $\bar{h} = \frac{h}{h_2} = a - (a-1)\cdot\bar{x}$

$$P = \frac{6\eta UB}{h_2^2}\frac{1}{a-1}\left\{\frac{1}{\bar{h}} - \frac{1}{a} - \frac{a}{1+a}\left(\frac{1}{\bar{h}^2} - \frac{1}{a^2}\right)\right\} \tag{5.5}$$

For Region II, by same manner as Region I, we can get

$$P = \frac{6\eta UB}{h_1^2}\frac{1}{a-1}\left\{\frac{a}{1+a}\left(\frac{1}{\bar{h}^2} - \frac{1}{a^2}\right) - \frac{1}{\bar{h}} + \frac{1}{a}\right\} \tag{5.6}$$

Figure 5.3 shows the fluid pressure distribution calculated by equation (5.5) and (5.6), when B = 250 μm, h_1 = 10 μm, h_2 = 5 μm, U = 5 mm/sec, η = 0.882 × 10^3 Pa·s (water).

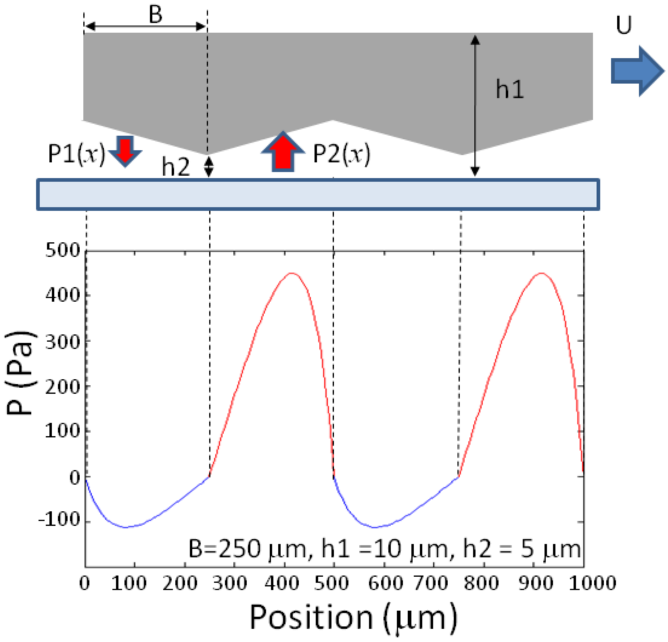

Figure 5.3 Pressure distribution on the riblet surface (B = 250 μm, h_1 = 10 μm, h_2 = 5 μm, U = 5 mm/sec)

As shown in Figure 5.3, upward force is generated on Region I, and downward force is generated on Region II. When integrating the all fluid pressure over the surface area, the total pressure force is always upward. This upward force makes the lubricant film thickness increase and fluid force decrease.

Now that the total fluid force on the MMT generated by the riblet surface can be calculated, finding the optimum riblet shape is next step in order to achieve precise actuation of the MMT in high speed region.

5.2 Optimization of Riblet Shape on the MMT

According to the Stribeck curve, the more the lubricant film thickness increases, the more fluid friction reduces. Thus, designing riblet shape (height h_1 and width B in Figure 5.2) to maximize the lubricant film thickness (h_2) leads to minimizing the friction on the MMT.

During the MMT movement in a microfluidic chip, there are three forces arise in vertical direction; gravity force ($F_{gravity}$), magnetic force in vertical direction (F_{magnet}), and fluid pressure force on the riblet (F_{fluid}). These three forces are balanced during MMT movement if the velocity of the MMT does not change and thus the lubricant film thickness is kept same. That is,

$$F_{gravity} + F_{magnet} + F_{fluid} = 0 \qquad (5.7)$$

Here, $F_{gravity}$ and F_{magnet} are easily measured and F_{fluid} can be calculated by equation (5.5) or (5.6). Therefore, we can find optimum combination of h_1 and B to maximize h_2 under the condition of equation (5.7).

To sum up, this optimization problem can be expressed as follows;

Maximize: h_2 (lubricant film thickness)

With respect to: h_1, B (riblet shape)

Subject to: $F_{gravity} + F_{magnet} + F_{fluid} = 0$ (force balance in vertical direction)

Figure 5.4 shows calculation result of h_2 under the constraints of equation (5.7). The gravity force ($F_{gravity}$) of the MMT designed by Figure 3.9 was 5 μN and the vertical component of magnetic force F_{magnet} was 23 μN, which was experimentally measured. Based on this calculation result, the film thickness h_2 is not depend on riblet width B and it is maximized to 3.4 μm when h_1 = 8.8 μm.

In the next section, the fabrication method to produce the optimum riblet design is discussed.

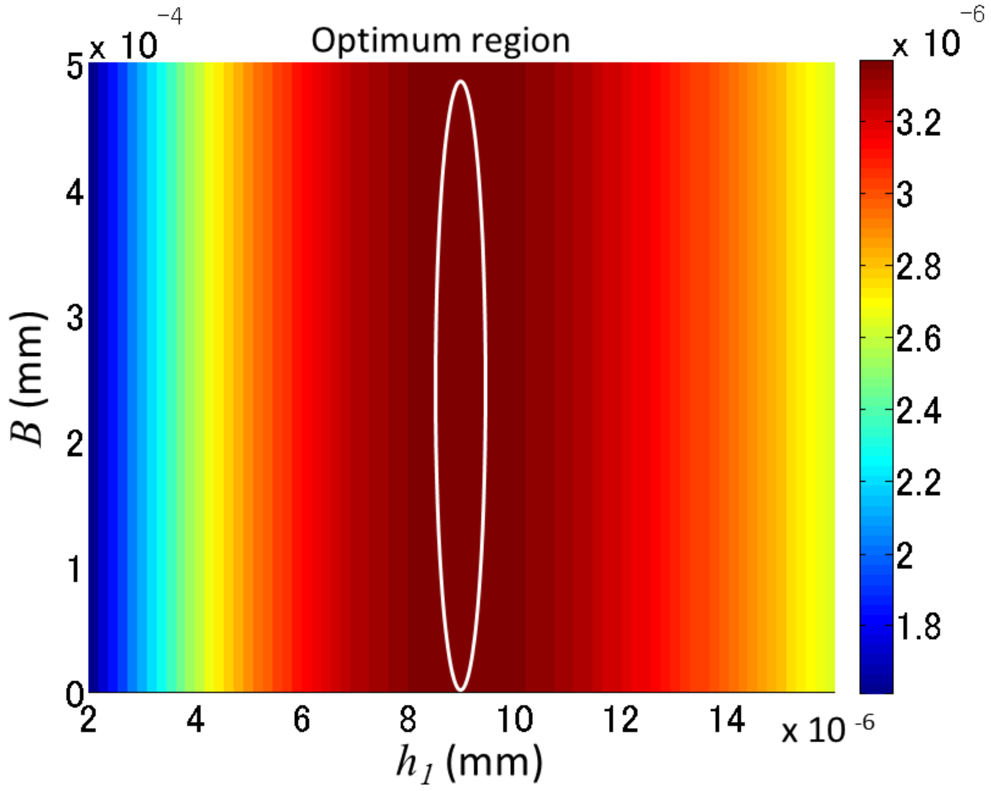

Figure 5.4 Result of optimum riblet design to maximize the lubricant film thickness h_2. (U = 15 mm/sec)

5.3 Fabrication of Si-Ni Composite Structure of MMT with Riblet

In order to produce the optimum riblet shape, it requires the precise three-dimensional fabrication. However, unlike previous chapters, it is quite difficult to produce micron meter size riblet on the MMT by electroplating. Therefore, the composite structure of Si and Ni is employed.

Figure 5.5 shows the fabrication process of Ni and Si composite fabrication. First, SiO_2 was sputtered on the 200 μm thickness Si wafer with (100) crystal orientation (thickness = 300 nm after 30 min, 240 W). Then, OAP (Tokyo Ohka Kogyo Co. LTD.) was spin-coated on SiO_2 to bond OFPR and SiO2 properly (2000 rpm, 30 sec). After the 3 min baking at 90 degrees, OFPR-800 200cp was spin-coated on the OAP by 2000 rpm, 30 sec (thickness = 4 μm). After the 30 min baking at 90 degrees, the OFPR was exposed by maskless laser lithography system (Heidelberg Inst.) (laser intensity = 50 W, 60 % without filtering) and stripes were patterned. Acid treatment was then conducted by 10:1 BHF buffered hydrogen fluoride (Stella Chemifa Co.) to etch SiO_2 (5 min, room temperature). After removing the OFPR by acetone, Si was etched by 50 % KOH at 75 degree for 26 min. Then, undercut phenomenon occurs and optimum riblet shape was fabricated on Si wafer (process 5 in figure 5.5). Figure 5.6 (a) shows the SEM image of Si after wet etching. The optimum riblet shape designed by the previous section was fabricated precisely.

Then, Cr/Au was sputtered on the riblet surface (thickness = 300 nm) and Ni was formed on the riblet surface by electroplating as a support sheet. After the SU-8 was coated on the opposite surface (thickness = 15 μm), it was exposed to pattern MMT shape. Then, DRIE was conducted to penetrate Si to form MMT (750 cycles). Figure 5.6 (b) shows Si wafer after DRIE. The interference fringe patter is shown because of the riblet surface.

After the Cr film is removed by Cr etchant, Ni was formed by electroplating. Finally, Si-Ni composite structure of MMT was fabricated after Cr / Au and Ni support sheet were removed by Cr and Au etchant. Figure 5.7 shows SEM image of fabricated MMT with optimized riblet. The riblet shape was patterned on Si and Ni surface and Ni was covered by Si. Therefore, the MMT becomes bio-compatible tools.

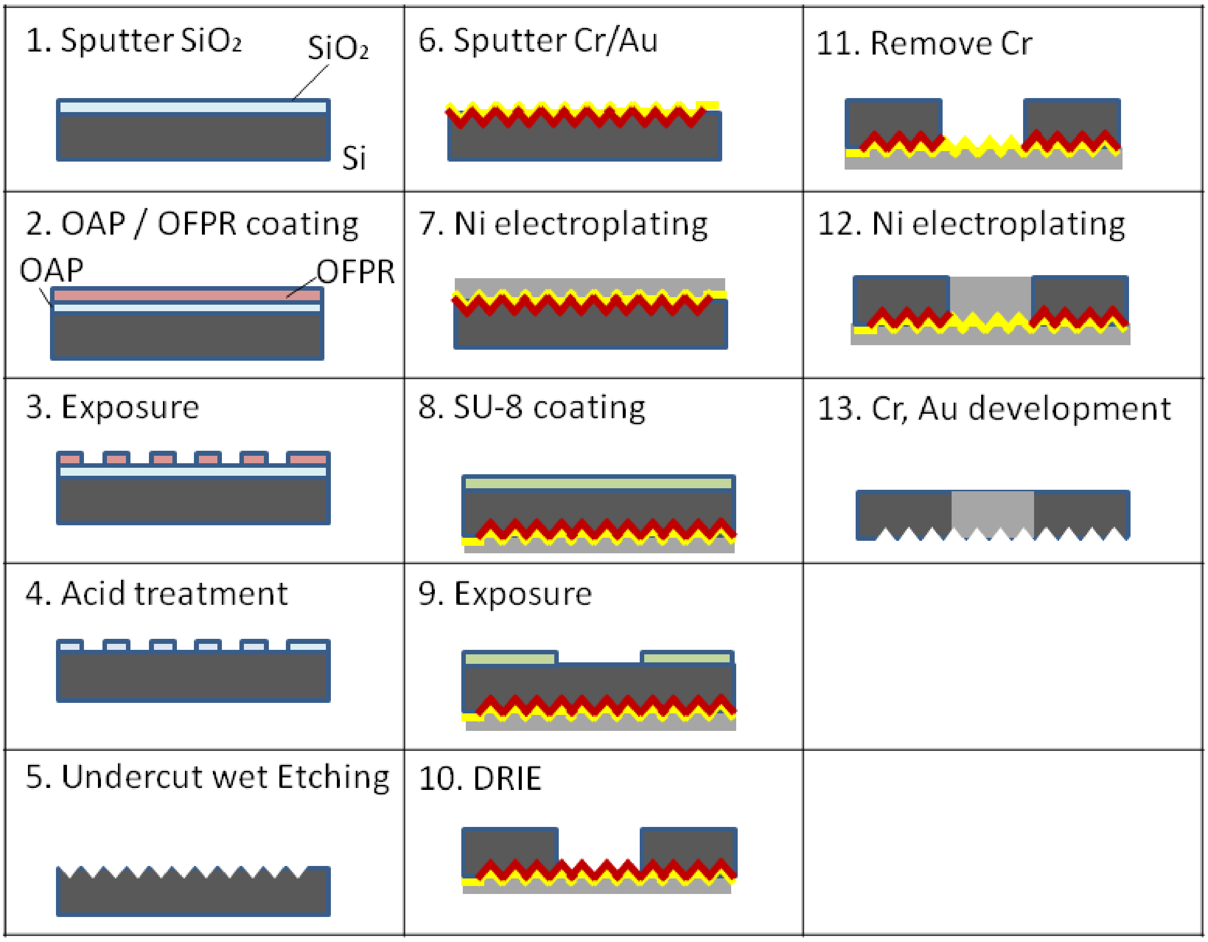

Figure 5.5 Fabrication process flow of Si-Ni composite MMT with riblet surface

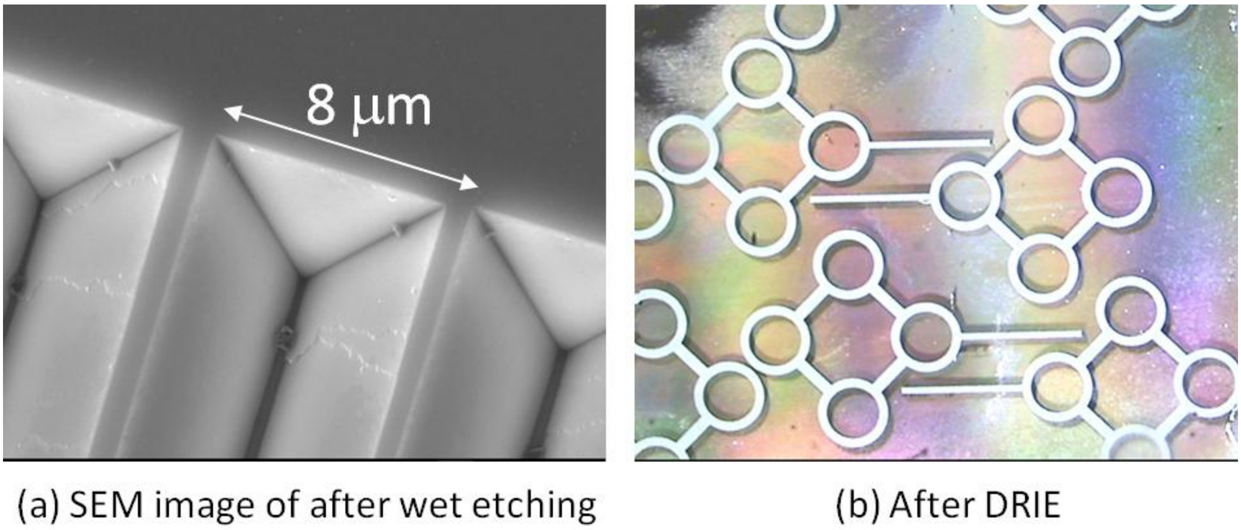

(a) SEM image of after wet etching (b) After DRIE

Figure 5.6 Fabrication of Si-Ni composite MMT with riblet surface

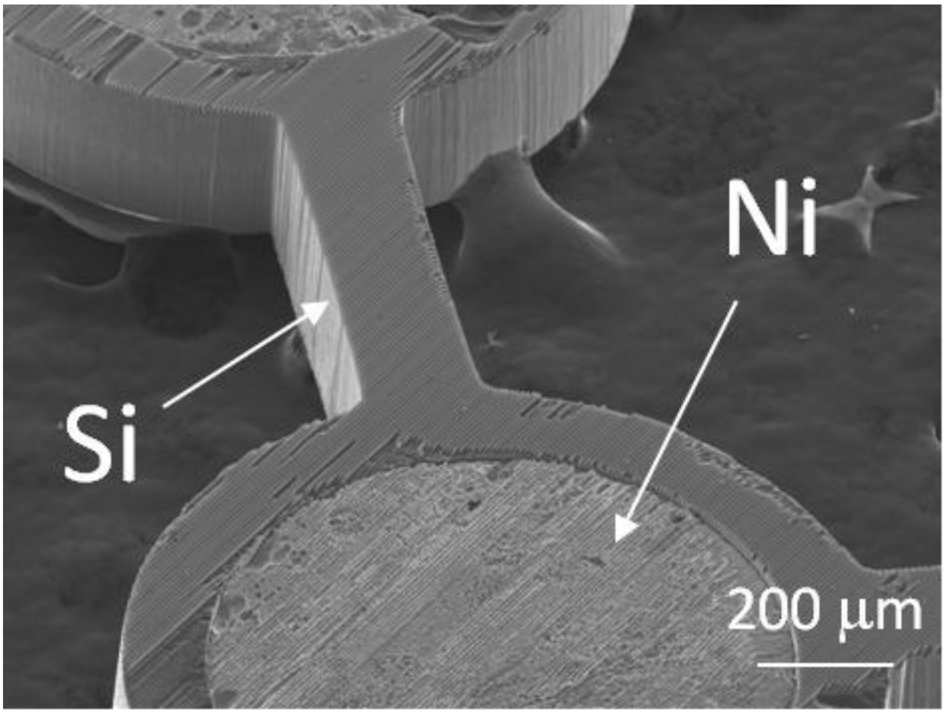

Figure 5.7 SEM image of Si-Ni composite MMT

5.4 Evaluation Experiments of Si-Ni composite MMT with Riblet

An experiment was conducted in order to evaluate the effect of the riblet surface and the improvement of the MMT positioning accuracy. The linear stage was actuated in a circular trajectory (diameter 1.0 mm) with the constant drive velocity. The corresponding MMT positions were measured by CCD camera through the microscope and stage position was recorded through encoder. The four of ϕ 1.0 mm × 1.0 mm columnar neodymium magnets were used as the drive unit in HPD conditions. 150 $V_{p\text{-}p}$ were applied to piezoelectric ceramics to induce the ultrasonic vibrations. Measurement was conducted for 100 points of Ni based MMT and Si-Ni composite MMT respectively in different stage velocities (0.31, 1.57, 3.14, 6.28, 9.42, 12.56 mm/sec).

Figure 5.8 shows the result of the evaluation experiments for the positioning accuracy of the MMT against the target trajectory. In low velocity region, the amount of error of MMT position from stage trajectory was almost same between the MMT with and without riblet while Si-Ni composite MMT with riblet surface obtain certain advantages against Ni MMT without riblet at high velocity region. Si-Ni composite MMT with riblet keeps precise poisoning accuracy in high speed region (more than 5 mm/sec) as well. This is because the more velocity increases, the more fluid friction reduces owing to the riblet shape as known as equation (5.5).

The effectiveness of the riblet is proved now, however, the riblet has orientation. Therefore, the frequency characteristic is measured for Si MMT in two different directions as well as Ni MMT. Figure 5.9 shows the experimental result. The drive stage moves in 1 degree of freedom with different frequency from 0.1 to 30 Hz sine wave and the stroke is ± 1.4 mm.

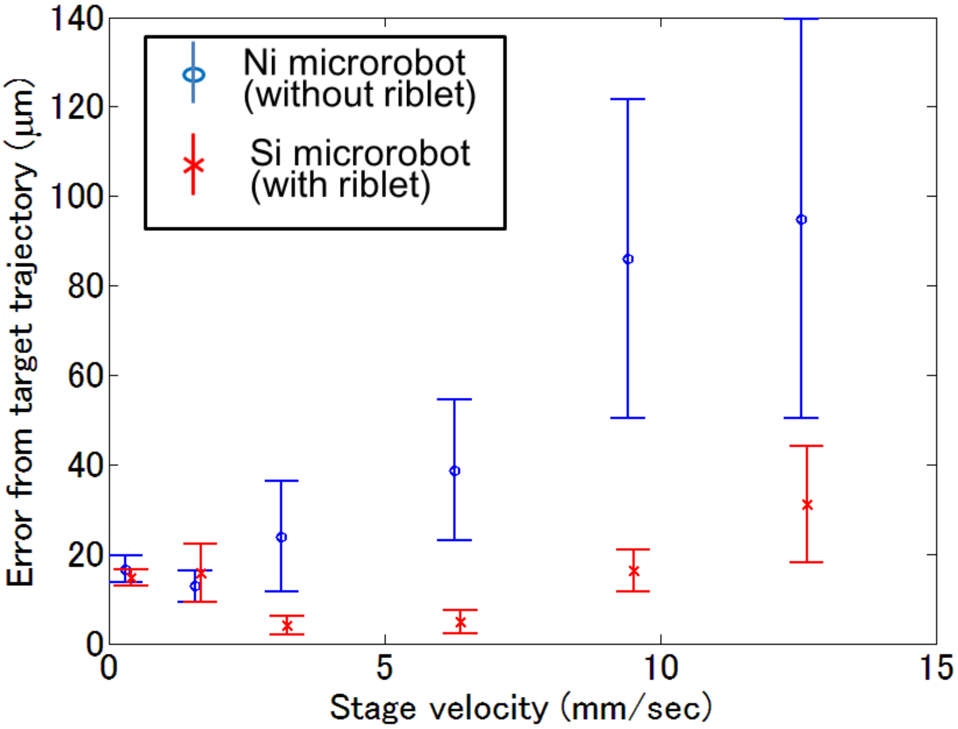

Figure 5.8 Evaluation of positioning accuracy for MMT with riblet surface.

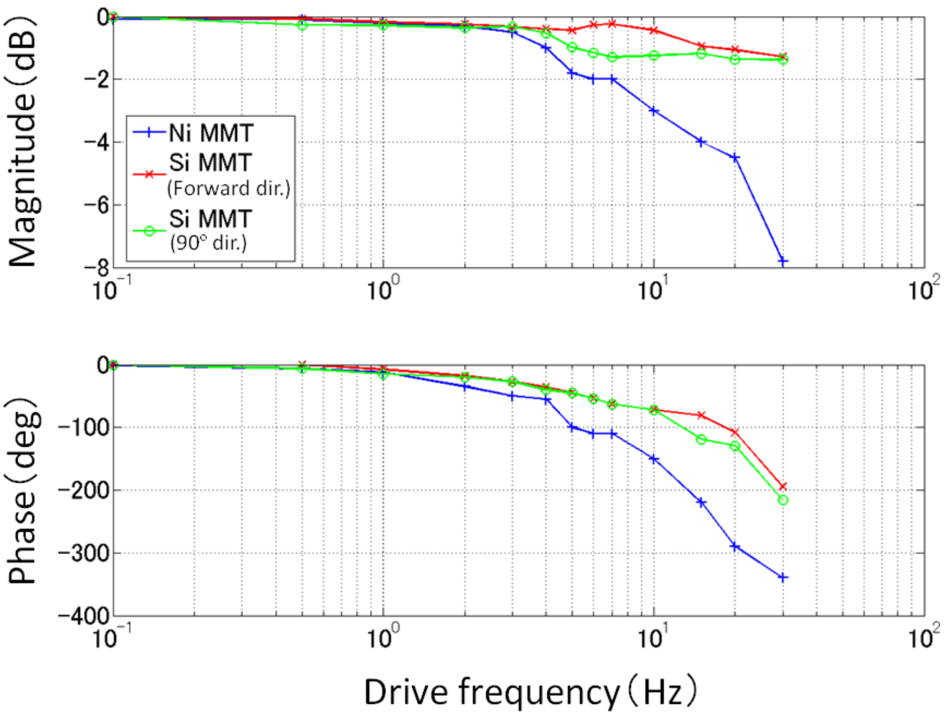

Figure 5.9 Frequency response characteristic of MMT with and without riblet.

The result shows that the MMT with riblet can follow the stage up to 30 Hz, which is the speed limit of the stage used while the MMT without riblet has delay after 5 Hz. Also, when the Si MMT with riblet moved in forward direction to the riblet, the response obtained better results than the case when it moved in 90 degree direction. But for both cases, the following response improved from the MMT without riblet. This is because the riblet is also useful to decrease friction owing to the smaller contact area to the substrate.

5.5 Conclusion Remarks

In this section, comprehensive analysis for the effect of riblet surface on MMT was conducted and it led to optimization of riblet shape to minimize the fluid friction on the MMT. Since the upward friction force increases with increasing MMT velocity, riblet has more advantages in high speed region.

For the fabrication of MMT with riblet, Si-Ni composite fabrication process was employed to obtain precise three dimensional shape on the MMT as well as taking advantage of bio-compatibility of Si material. Anisotropic wet etching of Si wafer was conducted to obtain riblet shape and DRIE and electroplating gave Si-Ni composite structure of the MMT.

The evaluation experiment was conducted and it was confirmed that the advantage of the riblet was getting large in high speed region. The positioning error of MMT with riblet from stage trajectory kept low even though the velocity increased. This advantage of riblet compensates the weakness of friction reduction by ultrasonic vibration discussed as previous chapter.

By combining these approaches discussed in Chapter 3, 4, and 5, the MMT can actuate high power (mN order), precise accuracy (μm order) and high speed (more than 10 mm/sec).

Chapter 6.

Application to Biomedical Innovations

6.1 Introduction

Cell manipulations in the confined space of a microfluidic chip are highly important in the field of biotechnology because of the low contamination capability, repeatability, and high throughput ability. Robots on a chip have great advantages for the treatment of biological cell instead of human handling due to their non-skill dependent, high throughput and high repeatability.

Now that the MMT can achieve precise positioning up to 1.1 μm, high speed actuation up to 15 mm/sec, and high power output force in the order of several millinewtons, a wide range of applications for cell manipulations can be achieved in a microfluidic chip. Here, several applications for cell manipulations by MMT in a microfluidic chip will be presented.

6.2 Enucleation of Oocyte

6.2.1 Background

Cloning has been actively investigated for use in food production, organ transplantation, and the development of genetically similar laboratory animals. The enucleation of oocyte is one of the cloning processes, which is time consuming and requires operation skill. In current operation, manually operated micromanipulators with glass capillaries are used to remove a nucleus under a microscope. However, the conventional manual manipulation tends to have problems of contamination, low success rate and low repeatability, and thus complicated cell manipulation could be carried out only by skilled people. Automation of the cloning technique is required for high-throughput production of processed cells with high quality and homogeneity [112]. The approach to enucleate oocytes in a microfluidic chip by hybrid MMTs and by 1-DOF MMTs with HPD were conducted previously [97] [113], but it was quite difficult to develop the automation system since the positioning error between the stage and the MMT was too large to control. Besides, it was difficult to handle continuously moving cell due to the slow response of the MMT against the drive stage. Ichikawa et al. proposed to cut oocyte for enucleation by controlled syringe pump to generate shear stress on an oocyte [114]. But the response speed of the syringe pump is not fast due to the difficulty to control flow in microchannel and cutting an oocyte takes 45 seconds.

Here we present enucleation of oocyte process operated by MMT in a microfluidic chip. Figure 6.1 shows the concept of enucleation of oocyte by dual-arm MMT. The size of oocyte is approximately 150 μm while MMT accuracy is several μm. Therefore, it is not difficult task to control oocyte posture, and remove nucleus from it. The target throughput time is 10 s, which is far superior to conventional operations and the cutting accuracy is less than 25% of

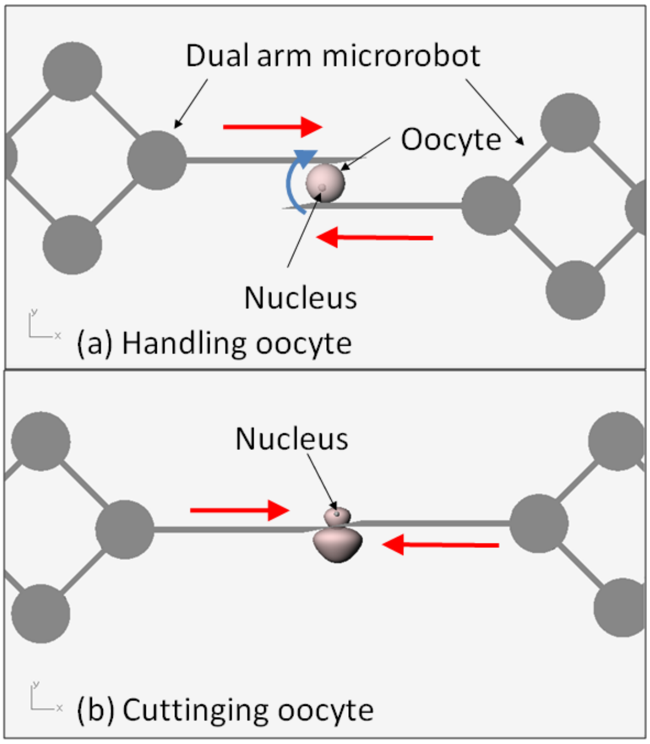

Figure 6.1 Concept of enucleation of oocyte by dual-arm MMT.

the original oocyte size.

6.2.2 Experimental setup

In advance of oocyte enucleation process, the swine oocyte has to be prepared with hylauronidase (0.1% of TCM 199) for 10 min in order to remove cumulus cells surrounding the oocytes and pronase (0.5% of PBS) for 10 min to remove zona pellucida. Then, Hoechst 34580 is applied for staining the nucleus of the oocyte.

Figure 6.2 shows the design of the microfluidic chip for the enucleation of oocytes. The oocytes are inserted at the inlet port and flow in a channel of 100 μm height and 200 μm width. The height of the channel to the nucleus collection port is set lowered (50 μm) so that the area containing nucleus cannot escape from the MMT to z direction. The dual-arm MMT then rotates the oocyte and area containing the nucleus is withdrawn into the channel. The dual-arm MMT cuts the oocyte with the tip of the blade and the nucleus part flows to the

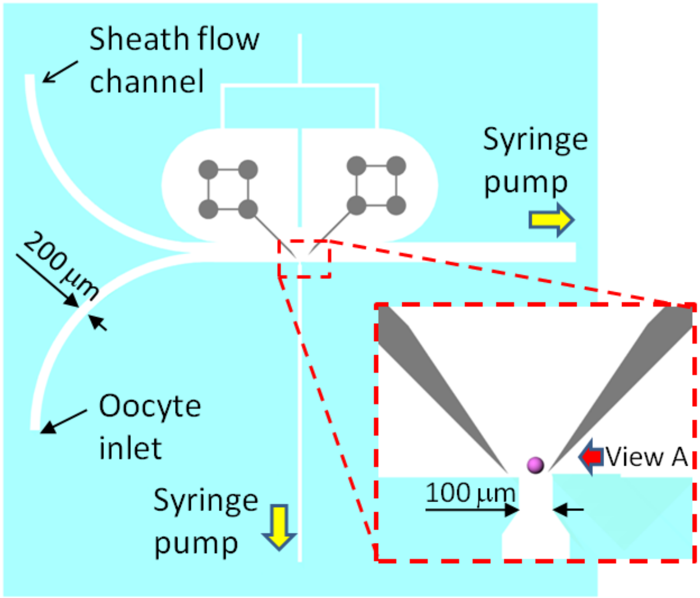

(a) Top view

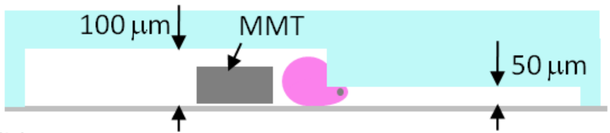

(b) View A

Figure 6.2 Design of the microfluidic chip for the enucleation of oocyte.

nucleus collection port. The remainder of the oocyte flows to oocyte collection port to be used in subsequent processes.

The sheath flow channel is set for the oocyte to flow along the PDMS wall and reaches to the manipulation area properly. Figure 6.3 shows the FEM for fluid analysis. The sheath flow restricts for the fluid from oocyte inlet port to flow to the area where MMT is placed, and thus oocyte can keep flowing along the wall. Also, the center PDMS wall between the dual arm MMTs prohibit fluid flow from occurring in MMT actuation area.

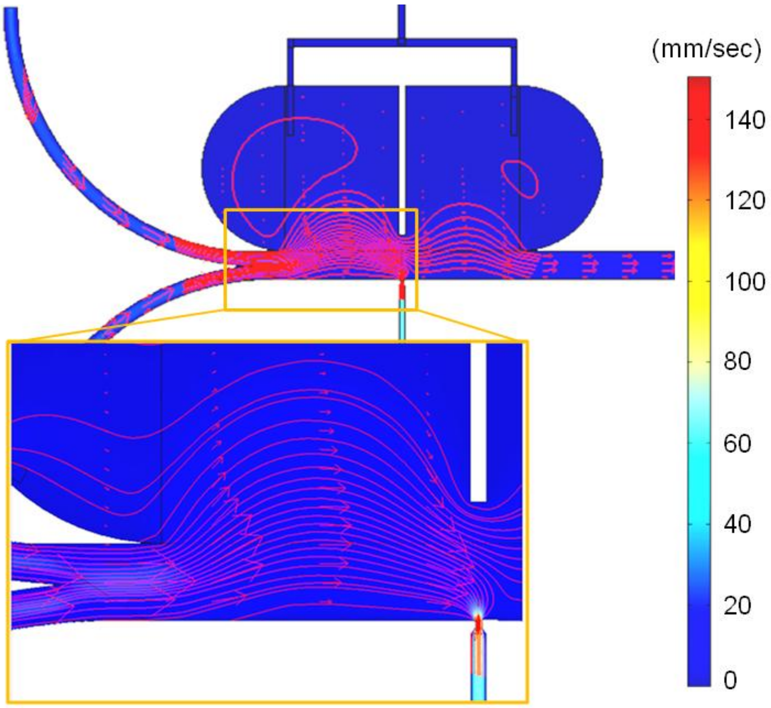

Figure 6.3 FEM analysis for fluid flow.

6.2.3 Experimental result

Figure 6.4 shows the experimental result of swine oocyte enucleation process. The oocyte inserted from the inlet flowed to the narrow channel and became lodged since the oocyte was not small enough to enter the channel of 30 μm width and height (Figure 6.4 (a)). After the nucleus position was confirmed, the oocyte was rolled by the MMT (Figure 6.4 (b)) and pushed back to the narrow channel so that the nucleus containing area was trapped in the channel (Figure 6.4 (c)). Then the tip of the MMT pressed oocyte (Figure 6.4 (d)) and cut the oocyte (Figure 6.4 (e)). It can be seen that the nucleus was successfully removed and the oocyte retained its circular shape even after the cutting (Figure 6.4 (f)). The processing time, which is the duration from the time when oocyte reached the narrow channel to the time when oocyte was cut, was less than 10 s and the amount of oocyte removed was about 20% of the original size.

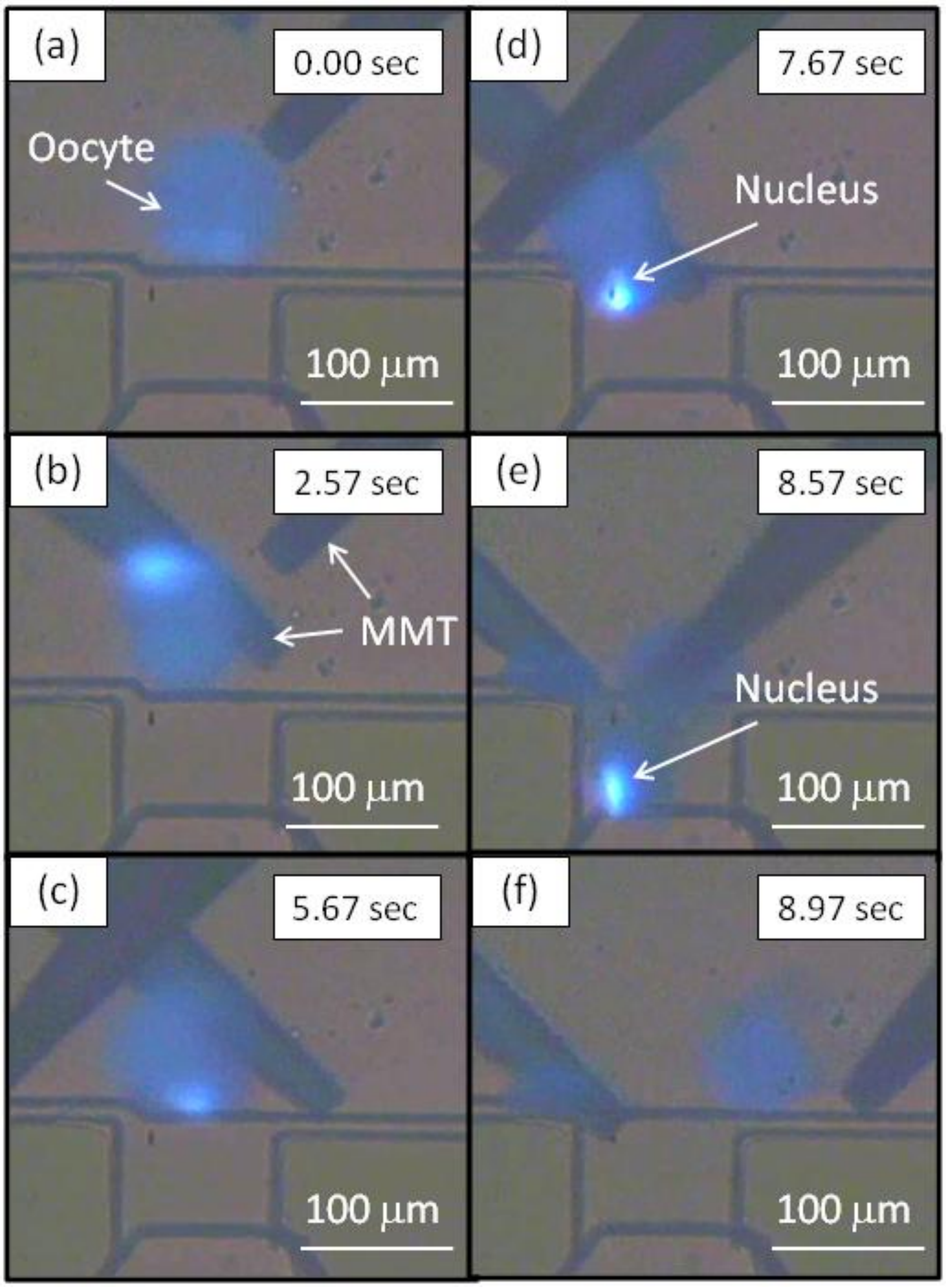

Figure 6.4 Experimental result of oocyte enucleation process by dual arm MMTs

6.3 Sorting Particle into Multiple Channels

6.3.1 Background

Sorting specific cells out of mixtures is required in cell observation and analysis cells. Flow cytometers, also called cell sorters and used to assay individual cells and separate or collect cells from suspensions [115] present problems of cost, size, and adaptability. Research is thus on in cell sorting on microfluidic chips to reduce cost, work space, contamination, and sample volume [116].

Related approaches have included dielectrophoretic sorting [117-119], optical trapping [28], magnetic isolation, adhesion cell sorting [120], and microvalve switching in microfluidic channels -- all of which require specially designed devices suiting the sorted object, e.g., size, sorting speed, and carrier liquid. A recently developed mechanical cell sorter using a polymer-based magnetically driven microtool (MMT) [93] has proven to be robust and reliable because it is unaffected by what it sorts and it can sort relatively large items thanks to high magnetic force but, as yet, has only on-off control and sorts items into just two channels only.

In this section, we propose the new type of particle sorter on a microfluidic chip into multiple channels by dual-arm MMT, as shown in Figure 6.5.The two sorting MMTs are activated by permanent magnets on XY stages from beneath the chip and block all but the desired channel. Particles flow into the open channel by fluid force. Separating particles into multiple parallel channels enables the drive to be small and speeds up throughput for sorting different particles.

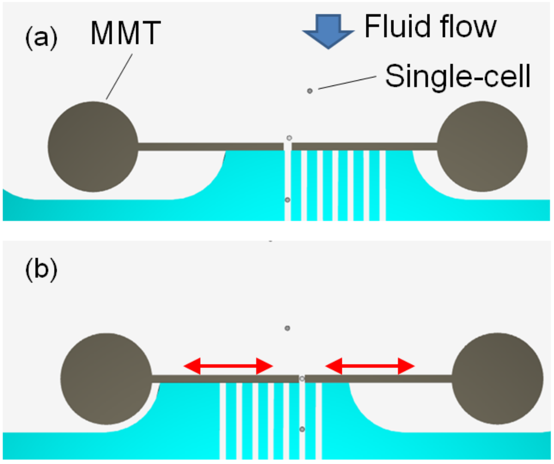

Figure 6.5 Concept of multiple sorting by MMT.

6.3.2 Designing microfluidic chip

Because the particle flow is determined by channel shape, FEM analysis was conducted for two types of typical channel designs for stable particle flow and sorting, as shown in Figure 6.6. Figure 6.6 (a) shows design in which particles flow from a wide channel into narrow branches, causing a vortex at the corner when MMTs arrive at the center and particles are trapped and not sorted into the desired channel. On the other hand, Figure 6.6 (b) shows design in which particles flow into a single line determined by MMT sorting. Note that the MMT in the upstream must have enough clearance in the channel for particles to be undisturbed by the flow and the MMT downstream must have less clearance to prevent overrun. In this case, the fluid flows linearly and thus the particle can sort to the channels smoothly. Therefore, (b) type of design is employed for multiple channels sorting chip.

Figure 6.7 shows the design of microfluidic chip for multiples sorting of ϕ 100 μm microbeads by MMT. In sorting on the microfluidic chip, the channel is 380 μm wide and the MMT upstream is160 μm wide to guide particles into the clearance between the channel and MMT. The MMT downstream is 320 μm wide to ensure that particles do not overrun. An assist flow from the MMT flexible upstream was added to prevent counter flow.

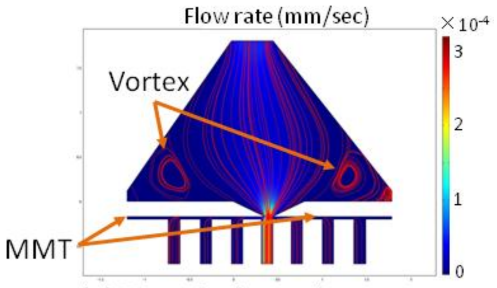

(a) Triangle channel type

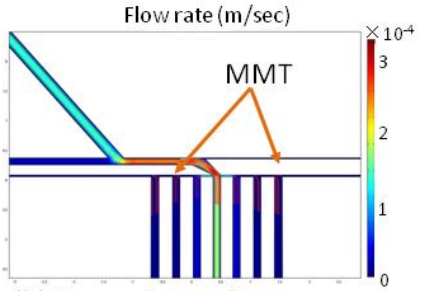

(b) Linear channel type

Figure 6.6 FEM analysis for fluid flow in two different type of channel.

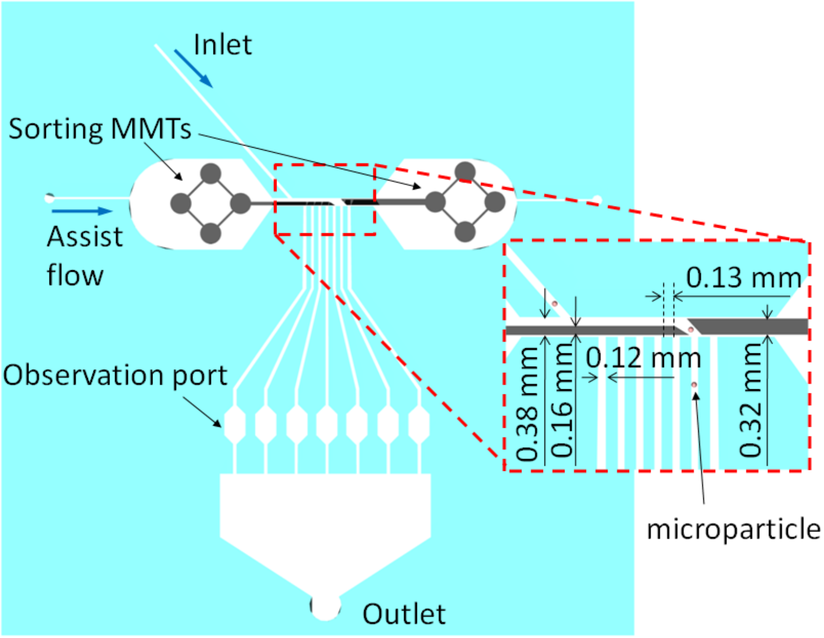

Figure 6.7 Design of microfluidic chip for multiple channels sorter by MMT.

6.3.3 Experimental result

Figure 6.8 shows sorting experiment results for 100 μm microbeads inserted from the inlet port. The microbeads flew through the MMT guide upstream and turned by the MMT downstream (Figure 6.8 (a)) in desired channel directions (Figure 6.8 (b)). When the MMT shifts to other channels, microbeads were sorted into multiple channels without remaining in the middle of the channel (Figure 6.8 (c)-(f)).

Theoretically speaking, the maximum throughput of this sorting is 59 particles/sec based on the fact that the MMT can actuate up to 15 mm/sec with less than 40 μm error according to previous chapter, and the channel pitch is 250 μm.

This sorting chip does not require any chemical, electrical, and optical property for particles and thus it can apply any kind of cells or particles without any damage.

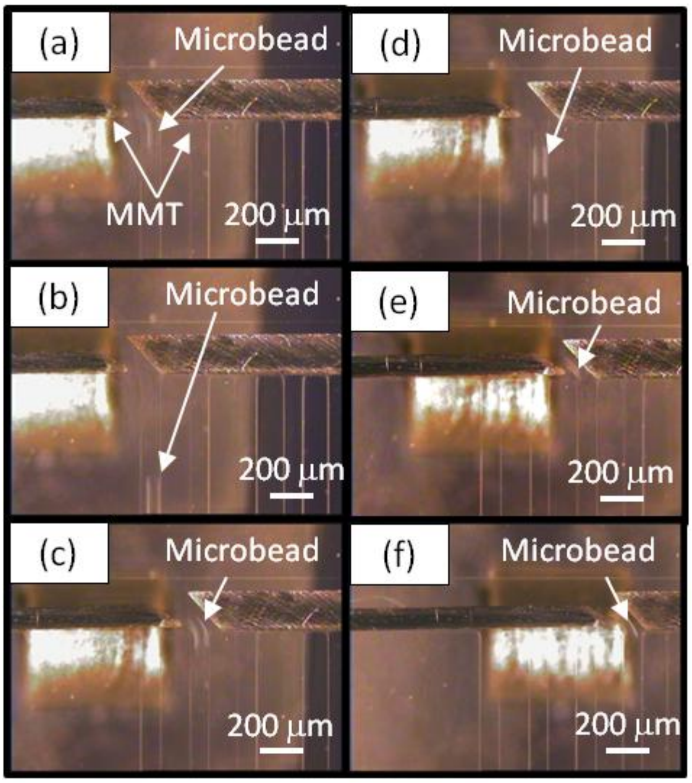

Figure 6.8 Result of multiple channel sorting for ϕ100 μm microbeads.

6.4 Other Applications Using MMT for Cell Manipulations

6.4.1 Cell spheroid assembly for regenerative medicine

Producing tridimensional organization in vitro is promising technology for regenerative medicine. It is expected to repair and replace damaged, injured or lost human organs. Conventionally the porous scaffold is employed as a framework to produce 3D tissue [121, 122], but scaffold may cause the problems after implant of human body. Therefore, many research related to producing 3D tissue structure without scaffolds is emerging. Yamato et al succeeded in culturing and accumulating cell sheet using temperature-responsive culture dishes [123, 124]. Matsunaga et al. produce 3D artificial structure by molding cells attached to collagen gel beads [125]. But it is difficult to assemble cells in arbitrary array in these approaches while the positional relationship is important for cells to grow or differentiate.

MMT can be suitable tool to produce 3D cell structure. MMT can handle spheroid, which is cell aggregation, easily since it has enough power. Assembling spheroid by MMT enables to create flexible cell array in high speed. Figure 6.9 shows the MDCK spheroid, which is staind in red, blue and green, assembly by dual arm MMTs. The throughput of the assembly can be increase thanks to high power output of MMT since it can treat more than 1000 cells at a time. Also it is easy to transport spheroid to the set position to achieve flexible array with different type of spheroids.

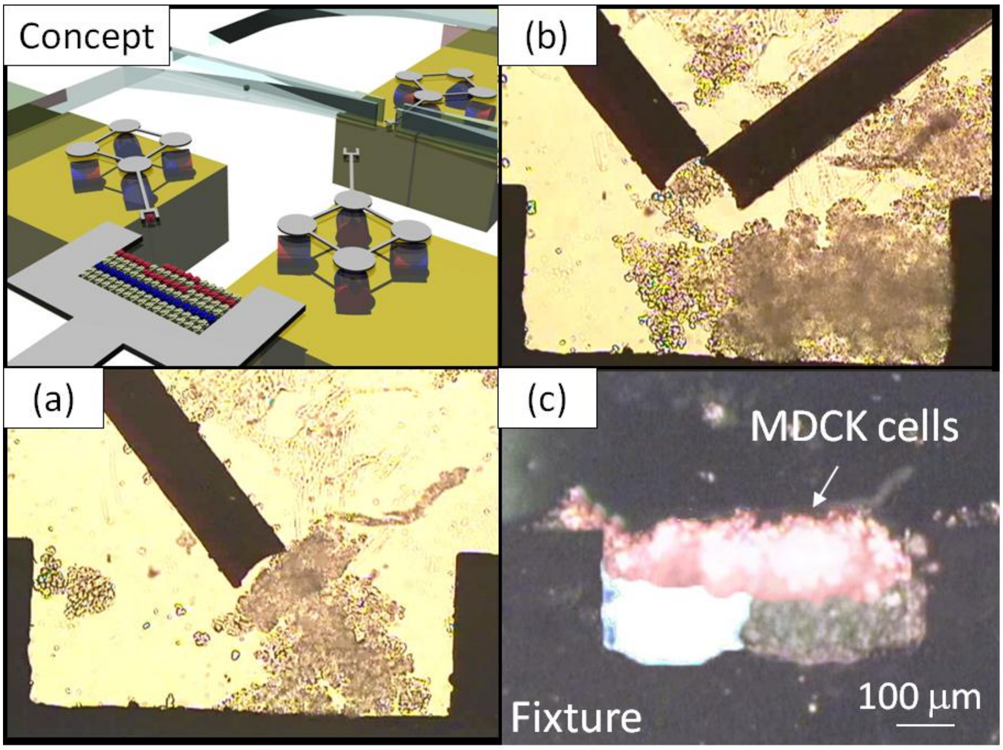

Figure 6.9 Spheroid assembly by dual-arm MMT.

6.4.2 Particle loader for continuous manipulation in a microfluidic chip

In order to achieve continuous particle or cell manipulations in a microfluidic chip, it is important that cell flows one by one. Unintended aggregation or jam of cell in a channel makes most operations difficult. Therefore, a cell loading system is required to supply appropriate amount of cells to manipulate with steady pace. In order to supply cells separately, it is reasonable to apply the physical force to control cell flow, and developed MMT is suitable tool here as well owing to high power output and high speed actuation.

Figure 6.10 shows the concept as well as experimental results of cell or particle loader by MMT. The MMT strokes up and down and when the MMT is at down part, the cell is loaded to hooked part of MMT and when the MMT moves up, cell is ejected to the channel where continuously flowing to the next operation. In experiments, ϕ100 μm microbeads were

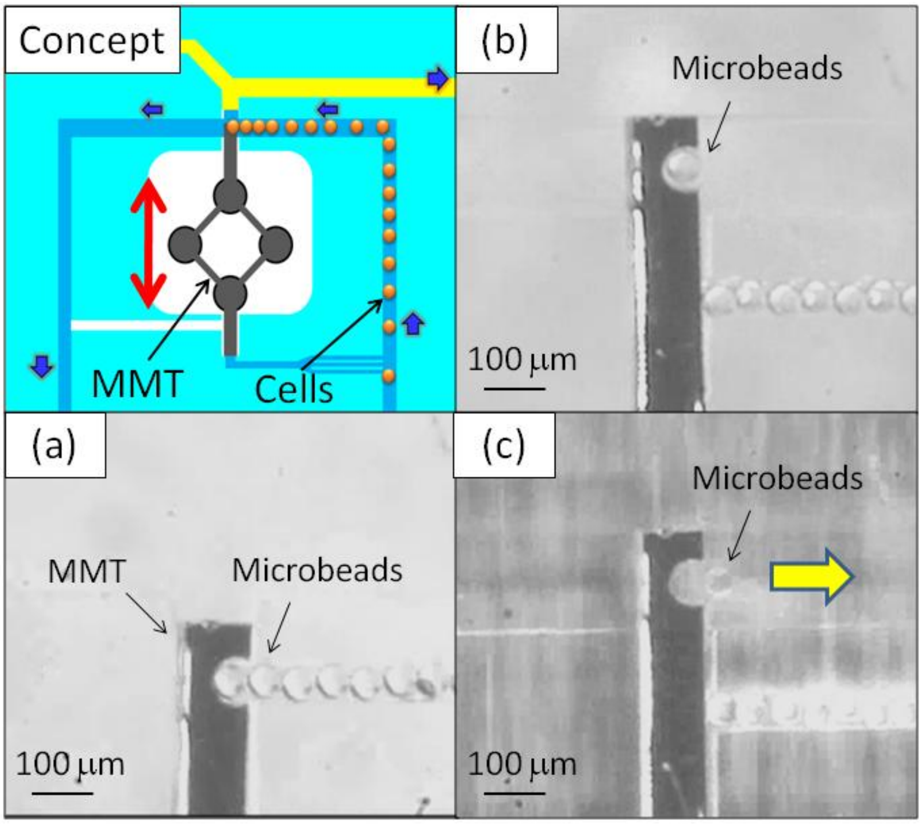

Figure 6.10 Particle loader by hooked shape MMT.

successfully delivered to next operation and the pitch of delivered beads can be controlled by changing frequency of the MMT stroke.

This loading system supply appropriate amount of cells to manipulate with steady pace and it makes continuous cell manipulation easier in a microfluidic chip.

6.5 Conclusion Remarks

In this chapter, several applications of MMT developed in previous chapters to cell manipulations in a microfluidic chip were presented. Because of mN order strong force, μm order positioning accuracy, and tens of mm/sec high speed actuation in 3-DOF, MMT can now apply to multi-scale of biological cell (5 μm – 500 μm). In addition, wide range of applications can be conducted such as cell cutting, sorting, assembling and loading, which are difficult to achieve by any other noncontact actuators due to lack of output force or accuracy.

Unlike conventional operation by mechanical manipulators, on-chip cell manipulation can be conducted as a flow process and cells can be supplied to the manipulation area from one second to the next. Therefore, the throughput of the process can be increased significantly once the system is setup. Then, this precisely controlled MMT is promising tool to develop high speed and high throughput automation process.

Chapter 7.

Conclusion

7.1 Summary

In this thesis, we have presented novel actuation methodology for magnetically driven microtool (MMT) and its application to cell manipulations in a microfluidic chip.

In chapter 2, first we defined the root cause of low positioning accuracy for an MMT as existence of dead band, where MMT does not move in spite of magnet movement. In order to analyze the dead band, the analytical modeling was developed for the static force on the MMT. The permanent magnet and the MMT were divided into small elemental area respectively and calculate the total magnetic force vector on the MMT. Then the drive force and friction force could be calculated from the total magnetic force vector. The fact that experimental value of dead band amount was corresponding to the simulation result, conduced that the friction on the MMT was dominant factor of the large amount of dead band.

In chapter 3, two distinguish drive methods, two-tiered magnetic drive (TMD) and horizontal polar drive (HPD), were developed to reduce vertical component of magnetic force on the MMT in order to reduce friction. Evaluation experiments were conducted to confirm the effectiveness of these drives by measuring error between MMT and drive magnet position when magnet stroked in 1 DOF. Results showed both driving improved MMT positioning accuracy by 5 – 10 times than conventional drive. However, both new drive methods do not receive any advantages in more than 1 DOF. Therefore, novel driving method was developed to improve positioning accuracy of MMT in 2-DOF by assembling four permanent magnets in HPD conditions respectively. The evaluation experiments indicated that it improved accuracy by 4-5 times but the absolute value of the positioning accuracy of MMT was still more than 50 μm, which was not enough to manipulate biological cells precisely

In chapter 4, another friction reduction method on the MMT was developed. A piezoelectric ceramics was attached to the glass substrate of microfluidic chip to induce ultrasonic vibration. Vibration gives friction direction change by tens of thousands times per seconds and it reduces effective friction on the MMT significantly. Applying this phenomenon with assembled HPD, minimum 1.1 μm positioning accuracy of MMT was achieved. The novelty of the friction reduction by vibration appeared on the response speed and output force as well. The MMT was actuated with up to 5 Hz in 3-DOF and the output force was increased about twice as much as the case without vibrations and reached 6.5 mN. The toxicity exam was also conducted to evaluate the effect of vibration on biological cells, but the growth rate was almost same as without vibration, which means the vibration does not give negative effect on cells. The MMT achieved minimum 1.1 μm positioning accuracy, several millinewton output force, and high speed actuation up to 5 Hz, however, both of precise accuracy and high speed actuation could not achieved since the friction reduction ratio decreases with increasing velocity of MMT.

In chapter 5, riblet surface, which is regularly arrayed V groove, was fabricated on the MMT by making MMT composite structure of Si and Ni in order to reduce fluid friction on the MMT and thus achieve precise positioning accuracy of MMT in high speed region as well. Analytical modeling was conducted and it led to calculate optimum riblet shape to minimize the fluid friction on the MMT. In order to fabricate micrometer order V groove, anisotropic wet etching and DRIE for Si was employed and then Ni electroplating gave composite structure of MMT. The evaluation experiments showed the positioning accuracy of MMT with riblet kept stable in high speed region (more than 5 mm/sec) as well while MMT without riblet deteriorate easily. By combining the three different friction reduction methodology for an MMT, high power, precise accuracy and high speed actuation was achieved at the same time.

In chapter 6 shows application of developed MMT for cell manipulations in a microfluidic chip. Owing to the high power and precise accuracy, MMT can apply wide range of applications for multi-scale of biological cells (5 – 500 μm). Enucleation of oocyte, sorting particle into multiple channel, assembling cell spheroids to produce spheroid sheet, and particle loading to achieve stable particle delivery for cell manipulation, were conducted. It was difficult to achieve those applications by any other noncontact actuators due to lack of power or accuracy.

The developed MMT can now use for many of cell manipulations, which currently commercialized mechanical manipulators conducts but the size of the manipulator is significantly smaller and the environment is more stable than a micromechanical manipulator owing to the closed space of the microfluidic chip.

7.2 Future Work

The future work of this research mainly contains two parts.

1. Environment control of microfluidic chip

In this thesis, we improved MMT performance by developing the drive unit and optimum MMT shape to reduce friction on the MMT. But surface condition on the microfluidic chip plays an important role of MMT actuation as well. The hydrophilic surface supplies thicker lubricant film in water environment and thus it makes the friction reduced as well. In addition, environment control is also important to achieve high throughput cell manipulation by MMT. It is frequently happens that cells are stick to the PDMS wall and prevent from continuous manipulation. Many of Lab-on-a-Chip researchers work on surface modification to control cell adhesions. Figure 7.1 shows surface modification to hydrophilic surface on the PDMS wall to selectively change the adhesion force on cell [126]. Combining these technologies give us distinguish performance of MMT and enable high throughput cell manipulations in a microfluidic chip.

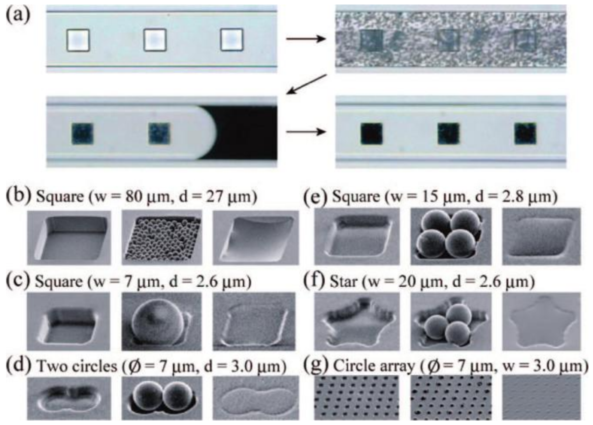

Figure 7.1 Surface modification by chemical modulation [126].

2. Automated cell manipulation by MMT

All of cell manipulations presented in this thesis were operated manually through joysticks. But now that the MMT accuracy improved, fully automated cell manipulation will be next step by integrating vision sensor, trajectory stage control, and feedback control of drive stage. Modeling of the cell manipulation is quite important to develop automation system. Cell is not a rigid body but a soft material where large deformation can be caused and thus, handling cell is not easy task as it seems to be.

By combining chemical and robotics technologies, cell manipulation by microrobot can be like production line of the manufacturing. Figure 7.2 shows the conceptual view of on chip cell production line. The microchannels with controlled surface become belt conveyer and transport cells one by one. And it reaches certain area, the sensor detects it and microrobot play determined task to conduct required cell manipulations. Then, cell manipulation can be completely non-skill dependent job.

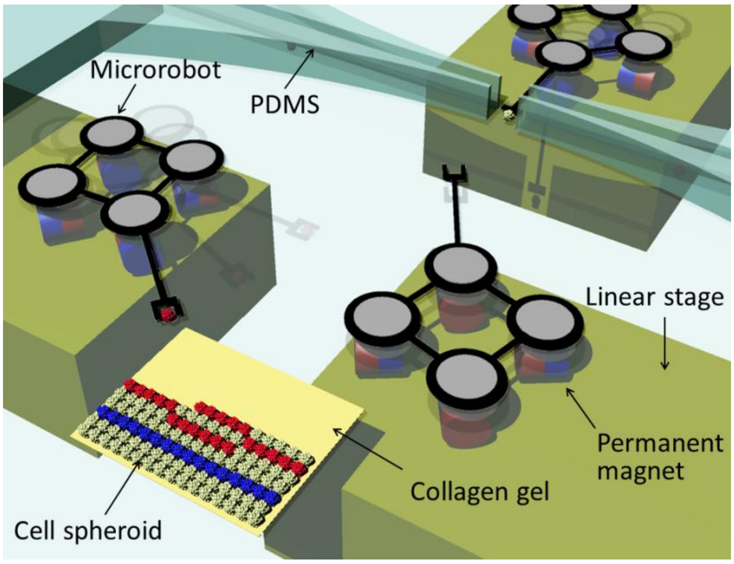

Figure 7.2 Concept of on-chip cell production line.

Bibliography

1. Wakayama T, Perry ACF, Zuccotti M, Johnson KR, Yanagimachi R: **Full-term development of mice from enucleated oocytes injected with cumulus cell nuclei**. *Nature* 1998, **394**:369-374.

2. Yanagida K, Katayose H, Yazawa H, Kimura Y, Konnai K, Sato A: **The usefulness of a piezo-micromnipulator in intracytoplasmic sperm injection in humans**. *Human Reproduction* 1998, **14**(2):448-453.

3. Murayama Y, Constantinou CE, Omata S: **Micro-mechanical sensing platform for the characterization of the elastic properties of the ovum via uniaxial measurement**. *Journal of Biomechanics* 2004, **37**(1):67-72.

4. Ramadan AA, Inoue K, Arai T, Taakubo T: **New Architecture of a Hybrid Two-Fingered Micro-Nano Manipulator Hand: Optimization and Design**. *Advanced Robotics* 2008, **22**(2):26.

5. Shen Y, Nakajima M, Kojima S, Hommma M, Ode Y, Fukuda T: **Characterization of Oscillating Nano Knife for Single Cell Cutting by Nanorobotic Manipulation System inside ESEM**. *Proceedings of the IEEE International Conference on Robotics and Automation* 2011:6.

6. Ahmad MR, Nakajima M, Kojima S, Homma M, Fukuda T: **Nanoindentation Methods to Measure Viscoelastic Properties of Single Cells Using Sharp, Flat, and Buckling Tips Inside ESEM**. *IEEE Transactions on nanobioscience* 2010, **9**(1):12.

7. Minerick AR, Zhou R, Takhistov P, Chang H-C: **Manipulation and characterization of red blood cells with alternating current fields in microdevices**. *Electrophoresis* 2003, **24**(21):3703-3717.

8. Cheng IF, Chang H-C, Hou D, Chang H-C: **An integrated dielectrophoretic chip for continuous bioparticle filtering, focusing, sorting, trapping, and detecting**. *Biomicrofluidics* 2007, **1**(2):021503.

9. Srivastava SK, Daggolu PR, Burgess SC, Minerick AR: **Dielectrophoretic characterization**

of erythrocytes: Positive ABO blood types. *Electrophoresis* 2008, **29**(24):5033-5046.

10. Becker FF, Wang XB, Huang Y, Pethig R, Vykoukal J, Gascoyne PRC: **Separation of human breast cancer cells from blood by differential dielectric affinity**. *Proceedings of the National Academy of Sciences of the United States of America* 1995, **92**:5.

11. Asbury CL, Engh G: **Trapping of DNA in Nonuniform Oscillating Electric Fields**. *Biophysical Journal* 1998, **74**:7.

12. Fiedler S, Shirley SG, Schnelle T, Fuhr G: **Dielectrophoretic Sorting of Particles and Cells in Microsystem**. *Analytical Chemistry* 1998, **70**(9):7.

13. Morgan H, Hughes P, Green NG: **Separation of Submicron Bioparticles by Dielectrophoresis**. *Biophysical Journal* 1999, **77**:10.

14. Yang J, Huang Y, X.B. W, Becker FF, Gascoyne PRC: **Cell Separation on Microfabricated Electrodes Using Dielectrophoretic / Gravitational Field-Flow Fractionation**. *Analytical Chemistry* 1999, **71**(5):8.

15. Gascoyne PRC, Vykoukal J: **Particle separation by dielectrophoresis**. *Electrophoresis* 2002, **23**:11.

16. Tsutsui H, Yu E, Marquina S, Valamehr B, Wong I, Wu H, Ho C-M: **Efficient Dielectrophoretic Patterning of Embryonic Stem Cells in Energy Landscapes Defined by Hydrogel Geometries**. *Annals of Biomedical Engineering* 2010, **38**(12):3777-3788.

17. Durr M, Kentsh J, Muller T, Schnelle T, Stelzle M: **Microdeveces for manipulation and accumulation of micro-and nanoparticles by dielectrophoresis**. *Electrophoresis* 2003, **24**:10.

18. Ashkin A, Dziedzic JM, Bjorkholm JE, Chu S: **Observation of a single-beam gradient force optical trap for dielectric particles**. *Optical Letters* 1986, **11**(5):3.

19. Ashkin A, Dziedzic JM: **Optical Trapping and Manipulation of Viruses adn Bacteria**. *Science* 1987, **235**:4.

20. Chu S, Bjorkholm J, Ashkin A, Cable A: **Experimental Observation of Optically Trapped Atoms**. *Physical Review Letters* 1986, **57**(3):314-317.

21. Mogensen PC, Gluckstad J: **Dynamic array generation and pattern formation for optical tweezers**. *Optics Communications* 2000, **175**:7.

22. Eriksen RL, Mogensen PC, Gluckstad J: **Multiple-beam optical tweezers generated by the generalized phase-contrast method**. *Optics Letters* 2002, **27**(4):3.

23. Arai F, Yoshikawa K, Sakami T, Fukuda T: **Synchronized laser micromanipulation of multiple targets along each trajectory by single laser**. *Applied Physics Letters* 2004, **85**(19):4301.

24. Bouchiat C, Wang MD, Allemand JF, Strick T, Block SM, Croquette V: **Estimating the Persistence Length of a Worm-Like Chain Molecule from**

Force-Extension Measurements. *Biophysical Journal* 1999, **76**:15.

25. Bustamante C, Macosko JC, Wuite GJL: **GRABBING THE CAT BY THE TAIL: MANIPULATING MOLECULES ONE BY ONE**. *Nature Reviews* 2001, **1**:7.

26. Ishijima A, Yanagida T: **Single molecule nanobioscience**. *TREND in Biochemical Sciences* 2001, **26**(7):7.

27. Kimura Y, Bianco PR: **Single molecule studies of DNA binding proteins using optical tweezers**. *The Analyst* 2006, **131**(8):868.

28. Arai F, Ichikawa A, Ogawa M, Fukuda T, Horio K, Itoigawa K: **High-speed separation system of randomly suspended single living cells by laser trap and dielectrophoresis**. *Electrophoresis* 2001, **22**:6.

29. Arai F, Ng C, Maruyama H, Ichikawa A, El-Shimy H, Fukuda T: **On chip single-cell separation and immobilization using optical tweezers and thermosensitive hydrogel**. *Lab on a Chip* 2005, **5**(12):1399.

30. Eriksson E, Sott K, Lundqvist F, Sveningsson M, Scrimgeour J, Hanstorp D, Goksor M, Graneli A: **A microfluidic device for reversible environmental changes around single cells using optical tweezers for cell selection and positioning**. *Lab on a Chip* 2010, **10**:9.

31. Werner M, Merenda F, Piguet J, Salathé R-P, Vogel H: **Microfluidic array cytometer based**

on refractive optical tweezers for parallel trapping, imaging and sorting of individual cells. *Lab on a Chip* 2011, **11**(14):2432.

32. Maruyama H, Kotani K, Masuda T, Honda A, Takahata T, Arai F: **Nanomanipulation of single influenzavirus using dielectrophoretic concentration and optical tweezers for single virus infection to a specific cell on a microfluidic chip**. *Microfluid Nanofluid* 2011, **10**:9.

33. Shi J, Mao X, Ahmed D, Colletti A, Huang TJ: **Focusing microparticles in a microfluidic channel with standing surface acoustic waves (SSAW)**. *Lab on a Chip* 2008, **8**(2):221.

34. Shi J, Huang H, Stratton Z, Huang Y, Huang TJ: **Continuous particle separation in a microfluidic channel via standing surface acoustic waves (SSAW)**. *Lab on a Chip* 2009, **9**(23):3354.

35. Franke T, Abate AR, Weitz DA, Wixforth A: **Surface acoustic wave directed droplet flow in microfluidics for PDMS devices**. *Lab on a Chip* 2009, **9**:3.

36. Shi J, Ahmed D, Mao X, Lin S-CS, Lawit A, Huang TJ: **Acoustic tweezers: patterning cells and microparticles using standing surface acoustic waves (SSAW)**. *Lab on a Chip* 2009, **9**(20):2890.

37. Wood CD, Cunningham JE, O'Rorke R, Wa̍lti C, Linfield EH, Davies AG, Evans SD: **Formation and manipulation of two-dimensional arrays of micron-scale particles in microfluidic systems by surface acoustic waves**. *Applied Physics Letters* 2009, **94**(5):054101.

38. Wood CD, Evans SD, Cunningham JE, O'Rorke R, Wa̍lti C, Davies AG: **Alignment of particles in microfluidic systems using standing surface acoustic waves**. *Applied Physics Letters* 2008, **92**(4):044104.

39. Franke T, Braunmüller S, Schmid L, Wixforth A, Weitz DA: **Surface acoustic wave actuated cell sorting (SAWACS)**. *Lab on a Chip* 2010, **10**(6):789.

40. Barnkob R, Augustsson P, Laurell T, Bruus H: **Measuring the local pressure amplitude in microchannel acoustophoresis**. *Lab on a Chip* 2010, **10**(5):563.

41. Bourquin Y, Reboud J, Wilson R, Cooper JM: **Tuneable surface acoustic waves for fluid and**

particle manipulations on disposable chips. *Lab on a Chip* 2010, **10**(15):1898.

42. Du XY, Fu YQ, Luo JK, Flewitt AJ, Milne WI: **Microfluidic pumps employing surface acoustic waves generated in ZnO thin films**. *Journal of Applied Physics* 2009, **105**(2):024508.

43. Luo JK, Fu YQ, Li Y, Du XY, Flewitt AJ, Walton AJ, Milne WI: **Moving-part-free microfluidic systems for lab-on-a-chip**. *Journal of Micromechanics and Microengineering* 2009, **19**:15.

44. Masini L, Cecchini M, Girardo S, Cingolani R, Pisignano D, Beltram F: **Surface-acoustic-wave counterflow micropumps for on-chip liquid motion control in two-dimensional microchannel arrays**. *Lab on a Chip* 2010, **10**(15):1997.

45. Yeo LY, Friend JR: **Ultrafast microfluidics using surface acoustic waves**. *Biomicrofluidics* 2009, **3**(1):012002.

46. Cecchini M, Girardo S, Pisignano D, Cingolani R, Beltram F: **Acoustic-counterflow microfluidics by surface acoustic waves**. *Applied Physics Letters* 2008, **92**(10):104103.

47. Rogers PR, Friend JR, Yeo LY: **Exploitation of surface acoustic waves to drive size-dependent microparticle concentration within a droplet**. *Lab on a Chip* 2010, **10**(21):2979.

48. Cugat O, Delamare J, Reyne G: **Magnetic Micro-Actuators and Systems (MAGMAS)**. *IEEE Transactions on Magnetics* 2003, **39**(5):3607-3612.

49. Barbic M, Mock JJ, Gray AP, Schultz S: **Electromagnetic micromotor for microfluidics applications**. *Applied Physics Letters* 2001, **79**(9):1399-1401.

50. Mensing GA, Pearce TM, Graham MD, Beebe DJ: **An externally driven magnetic microstirrer**. *Philosophical Transactions of the Royal Society A: Mathematical, Physical and Engineering Sciences* 2004, **362**(1818):1059-1068.

51. Rida A, Gijs MAM: **Manipulation of Self-Assembled Structures of Magnetic Beads for Microfluidic Mixing and Assaying**. *Analytical Chemistry* 2004, **76**:8.

52. Atencia J, Beebe DJ: **Magnetically-driven biomimetic micro pumping using vortices**. *Lab on a Chip* 2010, **4**:598-602.

53. Gauthier M, Piat E: **An electromagnetic micromanipulation system for single-cell manipulation**. *Journal of Micromechatronics* 2004, **2**(2):87-119.

54. Abbott JJ, O.Ergeneman, Kummer MP, Hirt AM, Nelson BJ: **Modeling Magnetic Torque and Force for Controlled Manipulation of Soft-Magnetic Bodies**. *IEEE Transactions on Robotics* 2007, **23**(6):1247-1252.

55. Abbott JJ, Peyer KE, Lagomarsino MC, Zhang L, Dong L, Kaliakatsos IK, Nelson BJ: **How Should Microrobots Swim?** *The International Journal of Robotics Research* 2009, **28**(11-12):1434-1447.

56. Zhang L, Peyer KE, Nelson BJ: **Artificial bacterial flagella for micromanipulation**. *Lab on a Chip* 2010, **10**(17):2203-2216.

57. Yesin KB: **Modeling and Control of Untethered Biomicrorobots in a Fluidic Environment Using Electromagnetic Fields**. *The International Journal of Robotics Research* 2006, **25**(5-6):527-536.

58. Arcese L, Fruchard M, Beyeler F, Ferreira A, Nelson BJ: **Adaptive backstepping and MEMS force sensor for an MRI-guided microrobot in the vasculature**. *Proceedings of the IEEE International Conference on Robotics and Automation* 2011:6.

59. Pawashe C, Diller E, Floyd S, Sitti M: **Assembly and Disassembly of Magnetic Mobile-Robots towardsa Deterministic 2-D Reconfigurable Micro-Systems**. *Proceedings of the IEEE International Conference on Robotics and Automation* 2011:6.

60. Pawashe C, Floyd S, Sitti M: **Modeling and Experimental Characterization of an Untethered Magnetic Micro-Robot**. *The International Journal of Robotics Research* 2009, **28**(8):1077-1094.

61. Sakar MS, Steager EB, Cowley A, Kumar V, Pappas GJ: **Wireless Manipulation of Single Cells using Magnetic Microtransporters**. *Proceedings of the IEEE International Conference on Robotics and Automation* 2011:6.

62. Sakar MS, Steager EB, Kim DH, Kim MJ, Pappas GJ, Kumar V: **Single cell manipulation using ferromagnetic composite microtransporters**. *Applied Physics Letters* 2010, **96**(4):043705.

63. Dittrich PS, Tachikawa K, Manz A: **Micro Total Analysis Systems. Latest Advancements and Trends**. *Analytical Chemistry* 2006, **78**:22.

64. Whitesides GM: **The origins and the future of microfluidics**. *Nature* 2006, **442**(7101):368-373.

65. Weibel DB, Kruithof M, Potenta S, Sia SK, Lee A, Whitesides GM: **Torque-Actuated Valves for Microfluidics**. *Annals of Chemistry* 2005, **77**:8.

66. Nieuwstadt HA, Seda R, Li DS, Fowlkes JB, Bull JL: **Microfluidic particle sorting utilizing inertial lift force**. *Biomedical Microdevices* 2010, **13**(1):97-105.

67. Gossett DR, Weaver WM, Mach AJ, Hur SC, Tse HTK, Lee W, Amini H, Di Carlo D: **Label-free cell separation and sorting in microfluidic systems**. *Analytical and Bioanalytical Chemistry* 2010, **397**(8):3249-3267.

68. Ookawara S: **Feasibility study on concentration of slurry and classification of contained particles by microchannel**. *Chemical Engineering Journal* 2004, **101**(1-3):171-178.

69. Wu Z, Willing B, Bjerketorp J, Jansson JK, Hjort K: **Soft inertial microfluidics for high throughput separation of bacteria from human blood cells**. *Lab on a Chip* 2009, **9**(9):1193.

70. Pamme N: **Continuous flow separations in microfluidic devices**. *Lab on a Chip* 2007, **7**(12):1644.

71. Huang LR: **Continuous Particle Separation Through Deterministic Lateral Displacement**. *Science* 2004, **304**(5673):987-990.

72. Bhagat AAS, Hou HW, Li LD, Lim CT, Han J: **Pinched flow coupled shear-modulated inertial microfluidics for high-throughput rare blood cell separation**. *Lab on a Chip* 2011, **11**(11):1870.

73. Vijayendran RA, Motesegood KM, Beebe DJ, Leckband DE: **Evaluation of a**

Three-Dimensional Micromixer in a Surface-Based Biosensor. *Langmuir* 2003, **19**:5.

74. Stroock AD, Dertinger SKW, Ajdari A, Mezic I, Stone HA, Whitesides GM: **Chaotic Mixer for Microchannels**. *Science* 2002, **295**:5.

75. Kricka LJ, Wilding P: **Microchip PCR**. *Analytical and Bioanalytical Chemistry* 2003, **377**(5):820-825.

76. Mae K: **Development of a new micromixer based on split/recombination for mass production and its application to soap free emulsifier**. *Chemical Engineering Journal* 2004, **101**(1-3):31-38.

77. Lee NY, Yamada M, Seki M: **Development of a passive micromixer based on repeated fluid twisting and flattening, and its application to DNA purification**. *Analytical and Bioanalytical Chemistry* 2005, **383**(5):776-782.

78. Lao K-L, Wang J-H, Lee G-B: **A microfluidic platform for formation of double-emulsion droplets**. *Microfluidics and Nanofluidics* 2009, **7**(5):709-719.

79. Mine Y, Shimizu M, Nakashima T: **Preparation and stabilization of simple and multiple emulsions using a microporous glass memblrane**. *Colloids adn Surfaces B* 1996, **6**:8.

80. Moritani T, Yamada M, Seki M: **Generation of uniform-size droplets by multistep hydrodynamic droplet division in microfluidic circuits**. *Microfluidics and Nanofluidics* 2011.

81. Nisisako T, Torii T, Higuchi T: **Droplet formation in a microchannel networkPresented at the International Symposium on Microchemistry and Microsystems (ISMM 2001), Kawasaki, Japan, September 16?18, 2001**. *Lab on a Chip* 2002, **2**(1):24.

82. Takeuchi S, Garstecki P, Weibel DB, Whiteside GM: **An Axisymmetric Flow-Focusing Microfluidic Device**. *Advanced Materials* 2005, **17**(8):6.

83. Teh S-Y, Lin R, Hung L-H, Lee AP: **Droplet microfluidics**. *Lab on a Chip* 2008, **8**(2):198.

84. Yamada M, Doi S, Maenaka H, Yasuda M, Seki M: **Hydrodynamic control of droplet division in bifurcating microchannel and its application to particle synthesis**. *Journal of*

Colloid and Interface Science 2008, **321**(2):401-407.

85. Jang K, Xu Y, Tanaka Y, Sato K, Mawatari K, Konno T, Ishihara K, Kitamori T: **Single-cell attachment and culture method using a photochemical reaction in a closed microfluidic system**. *Biomicrofluidics* 2010, **4**(3):032208.

86. Yamashita T, Tanaka Y, Idota N, Sato K, Mawatari K, Kitamori T: **Cultivation and recovery of vascular endothelial cells in microchannels of a separable micro-chemical chip**. *Biomaterials* 2011, **32**(10):2459-2465.

87. Trimmer WSN: **Microrobots and micromechanical systems**. *Sensors and Actuators* 1988, **19**(3):267-287.

88. Desai JP, Pillarisetti A, Brooks AD: **Engineering Approaches to Biomanipulation**. *Annual Review of Biomedical Engineering* 2007, **9**(1):35-53.

89. Castillo J, Dimaki M, Svendsen WE: **Manipulation of biological samples using micro and nano techniques**. *Integrative Biology* 2009, **1**(1):30-42.

90. Abbott JJ, Nagy Z, Beyeler F, Nelson BJ: **Robotics in the Small**. *IEEE Robotics & Automation Magazine* 2007:92-103.

91. Yamanishi Y, Feng L, Arai F: **On-demand Production of Emulsion Droplets Over a Wide Range of Sizes** *Advanced Robotics* 2010, **24**(14):2005-2018.

92. Yamanishi Y, Sakuma S, Kihara Y, Arai F: **Fabrication and Application of 3D Magnetically Driven Microtools**. *Journal oF Microelectromechanical Systems* 2010, **19**(2):8.

93. Yamanishi Y, Sakuma S, Onda K, Arai F: **Biocompatible polymeric magnetically driven microtool for particle sorting**. *Journal of Micro-Nano Mechatronics* 2008, **4**(1-2):49-57.

94. Yamanishi Y, Sakuma S, Onda K, Arai F: **Biocompatible Polymeric Magnetically Driven Microtool for Particle Sorting**. *Journal of Micro and Nano Mechatronics* 2008, **4**(1):9.

95. Maruyama H, Sakuma S, Yamanishi Y, Arai F: **Size-Dependent Filtration and Trapping of Microparticles in a Microfluidic Chip Using Graduated Gaps and Centrifugal Force** *Journal of Robotics and Mechatronics* 2010, **22**(3):6.

96. Yamanishi Y, Kihara Y, Sakuma S, Arai F: **On-chip Droplet Dispensing by Magnetically Driven Microtool**. *Journal of Robotics and Mechatronics* 2009, **21**(2):7.

97. Inomata N, Mizunuma T, Yamanishi Y, Arai F: **Omnidirectional Actuation of Magnetically Driven Microtool for Cutting of Oocyte in a Chip**. *Journal of Microelectromechanical Systems* 2010, **20**(2):383-388.

98. Israelachvili JN, Tabor D: **The measurement of van der Waals dispersion forces in the range 1.5 to 130 nm**. *Proceedings of the Royal Society of London Series A, Mathematical and PhysicalSciences* 1972, **331**(1584):21.

99. Ando Y, Ino J: **Friction and pull-off force on silicon surface modified by FIB**. *Sensors and Actuators* 1996, **A57**:7.

100. Gelinck ERM, Schipper DJ: **Calculation of stribeck curves for line contacts**. *Tribology International* 2000, **33**:175-181.

101. Lu X, Khonsari MM, Gelinck ERM: **The Stribeck Curve: Experimental Results and Theoretical Prediction**. *Journal of Tribology* 2006, **128**(4):789-794.

102. Dinelli F, Biswas SK, Briggs GAD, Kolosov OV: **Ultrasound induced lubricity in microscopic contact**. *Applied Physics Letters* 1997, **71**(9):3.

103. Bohringer KF, Goldberg K, Cohn M, Howe R, Pisano A: **Parallel microassembly with electrostatic force fields**. In: *International Conference on Robotics and Automation: 1998; Leuven, Belgium*; 1998: 8.

104. Littmann W, Storck H, Wallaschek J: **Sliding friction in the presence of ultrasonic oscillations: superpositioni of longitudinal oscillation**. *Archive of Applied Mechanics* 2001, **71**:549-554.

105. Storck H, Littmann W, Wallaschek J, Mracek M: **The effect of friction reduction in presence of ultrasonic vibrations and its relevance to travelling wave ultrasonic motor**. *Ultrasonics* 2002, **40**:379-383.

106. Kumar V: **Reduction of the sliding friction of metals by the application of longitudinal or transverse ultrasonic vibration**. *Tribology International* 2004, **37**(10):833-840.

107. Nakagawa T, Takahashi M, Ozaki T, Watanabe Ki, Todo S, Mizuguchi H, Hayakawa T, Nakagawara A: **Autoinhibitory Regulation of p73 by Np73 To Modulate Cell Survival and Death through a p73-Specific Target Element within the Np73 Promoter**. *Molecular and Cellular Biology* 2002, **22**(8):2575-2585.

108. Kuhn DM, Balkis M, Chandra J, Mukherjee PK, Ghannoum MA: **Uses and Limitations of the XTT Assay in Studies of Candida Growth and Metabolism**. *Journal of Clinical Microbiology* 2003, **41**(1):506-508.

109. Choi H, Moin P, Kim J: **Direct numerical simulation of turbulent flow over riblets**. *Journal of Fluid Mechanics* 1993, **255**:39.

110. Bechert DW, Bruse M, Hage W, Hoeven JGT, Hoppe G: **Experiments on drag-reducing surfaces adn their optimization with an adjustable geometry**. *Journal of Fluid Mechanics* 1997, **338**:29.

111. Dean B, Bhushan B: **Shark-skin surfaces for fluid-drag reduction in turbulent flow: a review**. *Philosophical Transactions of the Royal Society A: Mathematical, Physical and Engineering Sciences* 2010, **368**(1929):4775-4806.

112. Yamanishi Y, Sakuma S, Iyanagi T, Arai F, Arai T, Hasegawa A, Tanikawa T, Ichikawa A, Satoh O, Nakayama A *et al*: **Design and Fabrication of ALl-in-One Unified Microfluidic Chip for Automation of Embryonic Cell Manipulation**. *Journal of Robotics and Mechatronics* 2011, **22**(3):7.

113. Hagiwara M, Kawahara T, Yamanishi Y, Arai F: **Precise Control of Magnetically Driven Microtools for Enucleation of Oocytes in a Microfluidic Chip**. *Advanced Robotics* 2011, **25**(8):991-1005.

114. Ichikawa A, Tanikawa T, Akagi S, Ohba K: **Automatic Cell Cutting by High-Precision Microfluidic Control**. *Journal of Robotics and Mechatronics* 2010, **23**(1):6.

115. Bonner WA, Hulett HR, Sweet RG, Herzenberg LA: **Fluorescence Activated Cell Sorting**. *The Review of Scientific Instruments* 1972, **43**(3):6.

116. Barry R, Ivanov D: **Microfluidics in biotechnology**. *Journal of Nanobiotechnology* 2004, **2**:5.

117. Schnelle T, Muller T, Gradl G, Shirley SG, Fuhr G: **Paired microelectrode system: dielectrophoretic particle sorting and force calibration**. *Journal of Electrostatics* 1999, **47**:12.

118. Yang J, Huang Y, Wang X, Wang XB, Becker FF, Gascoyne PRC: **Dielectric Properties of Human Leukocyte Subpopulations Determined by Electrorotation as a Cell Separation Criterion**. *Biophysical Journal* 1999, **76**:8.

119. Tai C-H, Hsiung S-K, Chen C-Y, Tsai M-L, Lee G-B: **Automatic microfluidic platform for cell separation and nucleus collection**. *Biomedical Microdevices* 2007, **9**(4):533-543.

120. Nishimura T, Miwa J, Suzuki Y, Kasagi N: **Label-free continuous cell sorter with specifically adhesive oblique micro-grooves**. *Journal of Micromechanics and Microengineering* 2009, **19**(12):125002.

121. Hutmacher DW: **Scaffold design and fabrication technologies for engineering tissues - state of the art and future perspectives**. *Journal of Biomaterial Science* 2001, **12**(1):18.

122. Vacanti JP, Morse MA, Saltzman WM, Dornb AJ: **Selective Cell Transplantation Using Bioabsorbable Artificial Polymers as Matrices**. *Journal of Pediatric Surgery* 1988, **23**(1):7.

123. Yamato M, Okano T: **Cell sheet engineering**. *Materials Today* 2004, **7**(5):42-47.

124. Yang J, Yamato M, Sekine H, Sekiya S, Tsuda Y, Ohashi K, Shimizu T, Okano T: **Tissue Engineering Using Laminar Cellular Assemblies**. *Advanced Materials* 2009, **21**(32-33):3404-3409.

125. Matsunaga YT, Morimoto Y, Takeuchi S: **Molding Cell Beads for Rapid Construction of Macroscopic 3D Tissue Architecture**. *Advanced Materials* 2011, **23**(12):H90-H94.

126. Yamamoto M, Yamada M, Nonaka N, Fukushima S, Yasuda M, Seki M: **Patterning Reactive Microdomains nside PDMS Microchannels by Trapping and Melting Functionsl Polymer Particles**. *Journal of American Chemistry Society* 2008, **130**:2.

Acknowledgement

It is my great pressure to acknowledge all people who concern this work.

First I would like to express gratitude to Professor Fumihito Arai, Department of Micro-Nano Systems Engineering, Nagoya University, Japan for his constant support, guidance, encouragement, patience, and giving me a chance to be a rechearer.

I would like to extend my sincere to Professor Toshio Fukuda in Department of Micro-Nano Systems Engineering, Professor Noritugu Umehara in Department of Mechanical Science and Engineering, Professor Masahiro Ohka in Department of Complex Systems Science, Professor Yoko Yamanishi in Department of Micro-Nano Systems Engineering, for kindly agreeing with being my doctoral committee member.

I would also like personally thank to Dr. Yoko Yamanishi, Dr. Tomohiro Kawahara, Dr. Hisataka Maruyama, Dr. Taisuke Masuda and Dr. Akihiko Ichikawa, Mr. Shinya Sakuma, Mr. Kazuhiko Onda for their constant support not only for the research aspect but also personal as well. I would like to extend my thanks to all the lab member to share the precious time in my doctoral course.

Finally, I would like to express my deepest gratitude to my wife and daughter for their encouragement and support.

Masaya Hagiwara